Charge noise and spin noise
in a semiconductor quantum device

Inauguraldissertation

zur

Erlangung der Würde eines Doktors der Philosophie

vorgelegt der

Philosophisch-Naturwissenschaftlichen Fakultät

der Universität Basel

von

Andreas V. Kuhlmann

aus Ansbach-Strüth, Deutschland

Basel, 2014

Charge noise and spin noise
in a semiconductor quantum device

Inauguraldissertation

zur

Erlangung der Würde eines Doktors der Philosophie

vorgelegt der

Philosophisch-Naturwissenschaftlichen Fakultät

der Universität Basel

von

Andreas V. Kuhlmann

aus Ansbach-Strüth, Deutschland

Basel, 2014

creative commons

Namensnennung-Keine kommerzielle Nutzung-Keine Bearbeitung 2.5 Schweiz

---

Sie dürfen:

das Werk vervielfältigen, verbreiten und öffentlich zugänglich machen

Zu den folgenden Bedingungen:

Namensnennung. Sie müssen den Namen des Autors/Rechteinhabers in der von ihm festgelegten Weise nennen (wodurch aber nicht der Eindruck entstehen darf, Sie oder die Nutzung des Werkes durch Sie würden entlohnt).

Keine kommerzielle Nutzung. Dieses Werk darf nicht für kommerzielle Zwecke verwendet werden.

Keine Bearbeitung. Dieses Werk darf nicht bearbeitet oder in anderer Weise verändert werden.

- Im Falle einer Verbreitung müssen Sie anderen die Lizenzbedingungen, unter welche dieses Werk fällt, mitteilen. Am Einfachsten ist es, einen Link auf diese Seite einzubinden.

- Jede der vorgenannten Bedingungen kann aufgehoben werden, sofern Sie die Einwilligung des Rechteinhabers dazu erhalten.

- Diese Lizenz lässt die Urheberpersönlichkeitsrechte unberührt.

Quelle: http://creativecommons.org/licenses/by-nc-nd/2.5/ch/   Datum: 3.4.2009

Genehmigt von der Philosophisch-Naturwissenschaftlichen Fakutltät auf Antrag von

Prof. Dr. Richard J. Warburton

Prof. Dr. Paul M. Koenraad

Basel, den 10.12.2014

Prof. Dr. Jörg Schibler

Dekan

Acknowledgements

First and foremost I would like to thank my supervisor Richard J. Warburton for all his help, support and motivation. His enthusiasm for physics was always inspiring and encouraging to me. I owe my successes and achievements to Richard's input. My sincere thanks go to the entire Nano-Photonics group, both past and present. In particular I would like to thank Julien for his input, help and guidance. I truly enjoyed working with you. My thanks go to Jonathan and Lukas for their great help and effort in the experiments. I would like to thank Martino Poggio and his entire group for their support. Moreover I would like to thank the mechanical and the electronic workshop for their impressive work.

Second and most importantly I would like to thank all the people and friends I got to know throughout my studies. Thank you for living, biking, hiking, running and above all enjoying life with me.

I would like to thank my family for their support and love. All of them, my mother, father, sister, uncle and aunt are an important and unmissable part of my life.

Last but not least I would like to thank my girlfriend Isla, the most remarkable outcome of my PhD.

Summary

Self-assembled quantum dots are very attractive as the building blocks for quantum light sources and spin qubits. For instance, a single quantum dot is a robust, fast, narrow-linewidth source of single photons, features not shared by any other emitter. A spin qubit is implemented by a single electron or hole confined to a quantum dot. Fundamental quantum mechanics have been explored in experiments with single quantum dots and spectacular success has been achieved. Future developments however demand an enhanced quantum coherence. For instance, indistinguishable single photons and coherent spins are required to implement a quantum repeater. For quantum-dot-based single photon sources, the linewidths are in the best case typically a factor of two larger than the transform limit in which the linewidth is determined only by the radiative decay time. Photons generated far apart in the time domain are therefore not indistinguishable. Spin coherence is presently limited to microsecond timescales. Improving the quantum coherence involves dealing with the noise inherent to the device. Charge noise results in a fluctuating electric field, spin noise in a fluctuating magnetic field at the location of the qubit, and both can lead to dephasing and decoherence of optical and spin states. Here, the noise and strategies to circumvent its deleterious effects are explored in order to optimize the performance of solid-state quantum systems.

This thesis is divided into five parts. The first chapter describes in detail the main experimental tool to explore noise in the solid-state: resonance fluorescence from single quantum dots. A polarization-based dark-field microscope is realized allowing background-free resonance fluorescence detection while operating in a set-and-forget mode.

Chapter 2 investigates charge fluctuations in a semiconductor. The origin of the main source of charge noise in the commonly used optical field-effect devices is pinned down: charge fluctuations at a GaAs/AlAs interface nearby the quantum dots. These defects are moved further away from the quantum dots in an improved sample design resulting in close-to-transform limited optical linewidths.

Even with the improved heterostructures, the transform limit is not reached. Noise spectra of both charge noise and spin noise provide powerful insights into the noise

inherent to the semiconductor, discussed in chapter 3. A time trace of the resonance fluorescence from a single quantum dot is translated into a noise spectrum. A crucial difference in their optical signatures allows the nature of the noise, charge or spin, to be identified. The charge noise is centred at low frequencies, the spin noise is centred at high frequencies. This technique is able to reveal the entire spectrum of the spin noise. The combined noise falls rapidly with frequency becoming insignificant above $50\,\mathrm{kHz}$ for the quantum dot optical transition as signalled by transform-limited linewidths.

The low frequency noise, charge noise, results in considerable noise in the emission frequency of the single photons. This problem is solved in chapter 4 with a dynamic feedback technique that locks the quantum emission frequency to a reference. The charge noise and its deleterious effects are highly reduced. A frequency-stabilized source of single photons in the solid-state is realized.

The low frequency linewidths are in the best case typically a factor of two larger than the transform limit. It is shown in chapter 5 that spin noise in the host material is the dominant exciton dephasing mechanism. This applies to both the neutral and charged excitons. For the neutral exciton, the spin noise increases with increasing excitation power. Conversely for the charged exciton, spin noise decreases with increasing excitation power. This effect is exploited to demonstrate transform-limited linewidths for the charged exciton even when the measurement is performed very slowly.

Contents

B   Supplementary information to chapter 3

C   Supplementary information to chapter 5

Chapter 1

Resonance fluorescence from single semiconductor quantum dots

Optically active quantum dots, for instance self-assembled InGaAs quantum dots, are potentially excellent single photon sources. The fidelity of the single photons is much improved using resonant rather than non-resonant excitation. With resonant excitation, the challenge is to distinguish between resonance fluorescence and scattered laser light. We have met this challenge by creating a polarization-based dark-field microscope to measure the resonance fluorescence from a single quantum dot at low temperature. We achieve a suppression of the scattered laser exceeding a factor of 10^7 and background-free detection of resonance fluorescence. The same optical set-up operates over the entire quantum dot emission range $(920 - 980 \, \text{nm})$ and also in high magnetic fields. The major development is the outstanding long-term stability: once the dark-field point has been established, the microscope operates for days without alignment. The mechanical and optical designs of the microscope are presented, as well as exemplary resonance fluorescence spectroscopy results on individual quantum dots to underline the microscope's excellent performance.

1.1 Introduction

Semiconductor quantum dots, in particular self-assembled InGaAs quantum dots, are very attractive as the building blocks for quantum light sources[1] and spin qubits[2]. Self-assembled InGaAs quantum dots (operating at wavelengths around 950 nm at low temperature) exploit technologically advanced GaAs heterostructures and have become the workhorse system in the field. It is hugely advantageous to explore the physics using resonant rather than non-resonant laser excitation. On the one hand, non-resonant excitation introduces sources of noise resulting in exciton and spin dephasing[3]. On the other hand, resonant (but not non-resonant) excitation allows a spin to be initialized[4,5], manipulated[6] and read-out[7] optically. Resonant excitation, i.e. coherent laser spectroscopy, on single InGaAs/GaAs quantum dots was first developed with differential transmission detection[8], using Stark-shift modulation of the transitions energy along with lock-in detection for noise rejection[9]. The detection scheme exploits an interference between the laser field and the field associated with coherently scattered photons[10]: it provides a sensitive detection scheme but does not provide direct access to the resonance fluorescence, the single photons scattered or emitted by the quantum dot. These photons are crucial to develop a high-fidelity single photon source and, further afield, in developing a quantum dot-based quantum network with applications in quantum communication[11].

Recently, the resonance fluorescence of a semiconductor quantum dot[3,12–21] has been observed. The challenge experimentally is to distinguish quantum dot-scattered light from scattered laser light. With non-resonant excitation, this separation is trivial to achieve on account of the widely different wavelengths. With resonant excitation, this scheme fails. One scheme for the detection of resonance fluorescence exploits the different wave vectors of the laser light and the resonance fluorescence[12–15]. This is very much in the spirit of the original ensemble experiments in atomic physics in which resonance fluorescence was detected in a direction orthogonal to the carefully defined propagation direction of the laser[22,23]. In a semiconductor context, one implementation of this scheme involves coupling laser light to a waveguide containing quantum dots with edge illumination, detecting the resonance fluorescence in the orthogonal vertical direction[12,13,15]. Another scheme exploits a further property of light: its polarization. The idea is to operate in the dark-field as defined by the polarization: the laser and the detection are defined to have orthogonal polarization states. Provided laser scattering preserves the polarization, the crossed polarizer configuration ensures that scattered laser light is prevented from entering the detection mode. Success has been achieved

using crossed linear polarizations[3,16–21].

In our experiments, we have pursued the polarization-based dark-field technique as, first, it doesn't require a specially fabricated waveguide and second, space limitations in the bore of a superconducting magnet limit the possibilities for efficient edge illumination. It is clear that achieving sufficient laser rejection based on polarization requires both high quality polarizing optics and exquisite angular control. Our first experiments achieved success but only for times of a few minutes after which the dark-field setting had to be re-optimized. This is likely to be a common problem. Here, we present both the mechanical and optical design of a dark-field microscope for resonance fluorescence experiments on a quantum dot. All the figures of merit are excellent, state-of-the art or better: polarization filtering allows us to suppress the excitation laser in the detection beam path by up to 8 orders of magnitude; even with a modest light collection efficiency, resonance fluorescence can be measured with a signal-to-background ratio exceeding 10^4 : 1. The property we emphasize however is *stability*. The long-term stability is such that the microscope can be operated for many days in a set-and-forget mode.

Our own motivation for developing the dark-field microscope was to push forward a research programme on single self-assembled quantum dots. However, we stress that our dark-field microscope is not limited to this field. It will be a perfect tool in the exploration of other quantum emitters for instance colour centres in diamond, single molecules and colloidal quantum dots.

1.2 Description of the dark-field microscope

The design of the dark-field microscope makes no particular demands on the sample although a flat, smooth surface is best. Once the wavelength range of the optics is adapted to the emission range, the dark-field concept operates equally well with the sample at room temperature or at low temperature. Here, as an example of a two-level system in the solid state, we study self-assembled InGaAs quantum dots emitting at wavelengths around 950 nm at low temperature. The microscope combines both high spatial resolution, implemented by a confocal set-up, and dark-field performance. It is designed to allow background-free detection of resonance fluorescence while operating in a set-and-forget mode.

1.2.1 Dark-field concept

The excitation and detection beams both follow the main axis of the microscope. Thus, laser light back-reflected at the sample has to be suppressed. Apart from its spatial mode, monochromatic laser light is characterized by two distinct features: its frequency and its state of polarization. Laser light cannot be distinguished from the quantum dot emission in frequency as it is a resonant scattering process. However, the state of polarization allows a discrimination to be made between laser and quantum dot photons. The light excitation and detection polarization states have to be orthogonal, here linear s and linear p.

Laser light suppression is implemented by means of orthogonal excitation/collection polarization states, in our case by two polarizing beam splitters (PBS), one linear polarizer and a quarter-wave plate. Their spatial arrangement is shown in Fig. 1.1. The purpose of the PBSs is to reject back-scattered laser light; the linear polarizer and quarter-wave plate define and control the state of light polarization. In this scheme, the PBSs define linear s-polarization and linear p-polarization for excitation and detection, respectively. The linear polarizer sets the polarization of the laser light to s-polarization before striking the PBS, the quarter-wave plate controls the polarization thereafter. In particular, the quarter-wave plate allows for a compensation should an ellipticity be inadvertently induced. The back-scattered s-polarized laser light is reflected by both the first and second PBS by $90\,^\circ$ such that the s-polarization is highly suppressed in transmission. The p-polarized component of the quantum dot emission, however, is transmitted and can be detected.

The confocal configuration improves the microscope's dark-field performance. Both light scattering at surface imperfections in the detection beam path and the p-polarized field component in the focal spot are highly suppressed. The more field confinement at the focus the larger is the p-polarized field component of the focal spot of an incident s-polarized laser beam[24]. However, the intensity distribution of the p-polarized component has a clover-leaf pattern with an antinode at the centre, i.e. it is highly suppressed by the confocal detection.

1.2.2 Dark-field microscope design

Experiments on single semiconductor quantum dots typically require low temperatures. The dark-field microscope is therefore integrated into a free-beam microscope system developed for low temperature experiments. The microscope optics apart from the objective lens remain under ambient conditions, as shown in Fig. 1.1. The construction

4
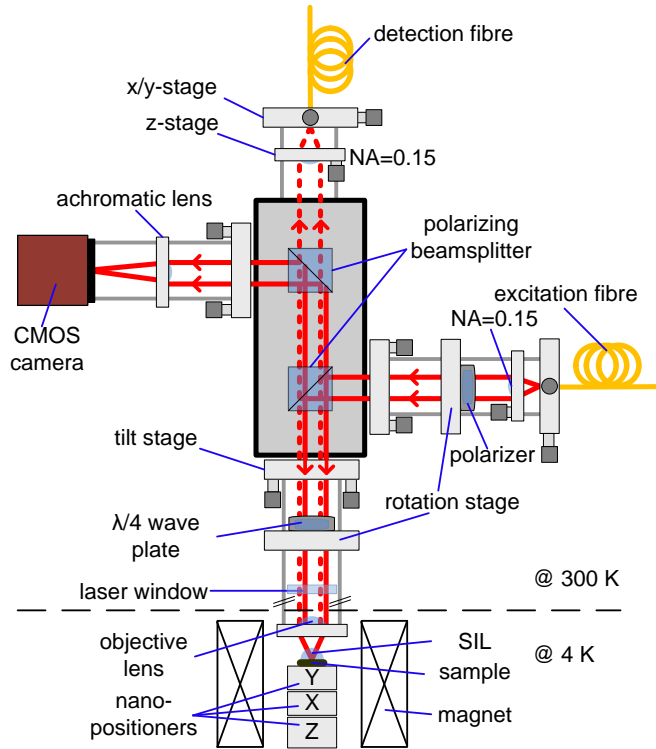
Fig. 1.1. Microscope set-up for resonance fluorescence experiments on a single InGaAs quantum dot. Two-level systems implemented in different materials can be studied both at room temperature and at low temperature. Here, a set-up to probe semiconductor quantum dots is shown. The sample with a hemispherical solid immersion lens (SIL) and the objective lens are located inside a bath cryostat, the rest of the microscope remains at room temperature. Optical access is provided by a sealed laser window. The microscope design: three modules, the lower horizontal microscope arm, the vertical arm and the upper horizontal arm are fixed to a central cage containing two polarizing beam splitters (PBSs). The excitation laser is injected via the lower horizontal arm; the vertical arm is used for detection; and the upper horizontal arm for imaging the sample surface. Optical fibres connect the microscope to lasers and detectors mounted on an adjacent optical table. Laser suppression is implemented by means of orthogonal excitation/collection polarization states: the linear polarizer sets the laser polarization to s, matching the lower PBS; the quarter-wave plate controls the state of polarization; and the PBSs reject the s-polarized back-reflected laser light. Solid lines indicate s-polarization, dashed lines p-polarization.

frame for the microscope "head" is a 30 mm cage system that allows a modular design: the lower horizontal microscope "arm" provides the excitation laser, the vertical arm is used for light detection and the upper horizontal arm to image the sample surface. Each module is attached to a central cage, hosting the PBSs.

The lower horizontal microscope arm provides a link between remote excitation sources and the microscope. Its output is a well collimated beam of coherent laser light, precisely controlled in linear polarization, and used to excite a single quantum dot res-

onantly. A single mode (SM) fibre (FONT Canada SM fibre NA = 0.12, mode field diameter (MDF) $5.2\,\mu$m) interconnects the microscope and the excitation laser (Toptica DL pro 940). By adjusting an x/y-translation stage (Thorlabs CP1XY), the fibre core can be centered on the optical axis defined by the collimator (Thorlabs C280TME-B NA = 0.15, f = 18.4 mm) which is mounted in a z-translation stage (Thorlabs SM1Z). Aspheric lenses are used to collimate/focus the laser beam, as they provide diffraction limited performance for monochromatic applications. A metallic nanoparticle linear film polarizer (Thorlabs LPVIS050-MP) mounted on a rotary stepper positioner (attocube ANR240) polarizes the excitation laser linearly and additionally allows the axis of linear polarization to be precisely controlled. The polarizer's transmission is 82 % and its extinction ratio exceeds 8 orders of magnitude at a wavelength of 950 nm. The piezo-driven rotary stepper positioner provides both 360 $^\circ$ endless rotation and a step size as small as $1\,$m$^\circ$. Furthermore, after aligning the polarizer position by means of the control electronics (attocube ANC300), the piezos are grounded and their position is locked, providing outstanding long-term stability. The four cage rods of the excitation arm are connected to a tilt stage (Thorlabs KC1-T/M) which is attached to the central beam splitter cage and allows for a compensation of any angular displacement of the beam.

The vertical microscope arm is designed to collect light efficiently with a confocal rejection of any stray light. This relies on coupling into a SM fibre (FONT Canada SM fibre NA = 0.12, MDF $5.2\,\mu$m) which interconnects the microscope and the detectors. The same optical and opto-mechanical components as for the light collimation unit of the horizontal arm are used. The vertical arm is assembled directly on to the PBS cage. The lower tilt stage allows to correct for a misalignment with respect to the optical axis of the objective lens (Thorlabs 352330-B NA = 0.68, f = 3.1 mm).

The upper horizontal microscope arm provides the possibility of monitoring the objective lens focal plane, i.e. the sample surface. An achromatic lens (Thorlabs AC254-150-B-ML, f = 150 mm) focuses light onto the chip of a complementary metal oxide semiconductor (CMOS) camera (Allied Vision Technologies Guppy F-503B), resulting in a magnified image (magnification of 48) of the sample surface. Again a tilt stage allows angular control of the optical axis.

All modules of the microscope are attached to a central cage made from a solid piece of aluminum. It provides stability to the microscope and at the same time hosts two PBSs (B. Halle & Nachfolger PTW 2.10), crucial to implement the polarization filtering. The PBSs allow beam splitting sensitive to the polarization of the incident beam. Two right angle prisms made of flint glass are cemented together to form a cube. A dielectric

beam-splitter coating which is deposited on one of the prisms provides a close to unity transmission for p-polarized and close to zero transmission for s-polarized light. The polarization suppression exceeds 4 orders of magnitude.

A quarter-wave plate (B. Halle & Nachfolger RZQ 4.10) is mounted beneath the PBSs on a second piezo rotary stage. (Note that the quarter-wave plate behaves as a half-wave plate for the reflected laser light as the laser beam passes it twice.) On the one hand, it is useful during the set-up procedure to misalign the quarter-wave plate deliberately and allow some reflected laser light into the detection arm. On the other hand, the quarter-wave plate represents an extra degree of freedom and it turns out that this is crucial: it compensates for any distortion from linear to elliptical polarization in the two polarization states. It is not exactly clear where these small distortions arise, but they are probably related to a birefringence of the sample (GaAs with thin metal layer), solid immersion lens, objective lens or the cryostat window. The quarter-wave plate used here is a zero order wave plate designed for 946 nm and was chosen because, first, it is less temperature sensitive than the multi-order counterparts; and, second, its performance at these particular wavelengths 950 ± 20 nm surpasses the performance of achromatic wave plates. The accuracy on the path difference of the quarter-wave plate is ± 2 nm. Again a crucial point for the long-term behaviour of the dark-field microscope is that the quarter-wave plate is mounted on a piezo positioner, as for the linear polarizer.

The microscope is inserted into a 2 inch bore stainless steel tube, evacuated, and filled with ~ 25 mbar He gas (exchange gas) at room temperature. The tube is then slowly inserted into a He bath cryostat equipped with a 9 T superconducting solenoid. The optics at 300 K are possibly subject to thermal drift but these are minimized by working in a $\pm 1\,^{\circ}$C temperature stabilized laboratory.

1.2.3 Dark-field microscope alignment

The microscope operates in both confocal and dark-field modes. For confocal performance, the excitation and collection beams must be concentric and parallel to the optical axis of the objective lens. While monitoring the focal spots on the sample surface, the tilt stages are aligned in order to superimpose the focal spots. The z-position of the sample relative to the objective focal plane is adjusted by moving the sample with nanometer precision. During this alignment step, laser light is also coupled into the fibre of the vertical microscope arm. Subsequently, once the confocal condition has been achieved, the linear polarizer and quarter-wave plate are aligned to suppress the back-reflected laser light. The linear polarizer is aligned to define the polarization of the

laser to s. A rough alignment is done by monitoring the transmitted signal at the PBS as the polarizer is moved. A minimum in transmission is required. The dark-field point is set by monitoring the back-reflected laser intensity. First, the linear polarizer is fine aligned by minimizing the back-reflected light and secondly the quarter-wave plate. We find that iterative fine tuning of the polarizer and quarter-wave plate angles enhances the rejection further, typically by a factor of 10 after ~ 3 iterations. Piezo-electronics allow remote control of both the angle of the linear polarizer and the quarter-wave plate. Once the angles are set, the piezos are grounded.

1.3 Dark-field microscope performance

The performance of the dark-field microscope is characterized under real, experimental conditions: the laser is focused on a quantum dot sample in a low temperature experiment.

1.3.1 Quantum dot sample

The InGaAs quantum dots are grown by molecular beam epitaxy utilizing a strain-driven self-assembly process and are embedded in a Schottky diode[25,26]. They are separated from an n^+ back contact by a $25\,nm$ thick GaAs tunnel barrier. On top of the quantum dots is a capping layer of thickness $150\,nm$, followed by a blocking barrier, an AlAs/GaAs superlattice of thickness $272\,nm$. The samples are processed with Ohmic contacts to the back contact, grounded in the experiment, and with a semi-transparent gate electrode on the surface (3/7 nm Ti/Au) to which a gate voltage V_g is applied. The number of carriers confined to the quantum dot can be precisely controlled by the applied voltage, allowing the different charged excitons to be addressed. Detuning of the exciton energy with respect to the constant laser frequency is achieved by sweeping V_g on account of the dc Stark effect. The laser spectroscopy is carried out at $4.2\,K$ by focusing a $1\,MHz$ linewidth laser to a $0.5\,\mu m$ spot on the sample surface. A ZrO_2 solid immersion lens is mounted directly on top of the sample in order to enhance the collection efficiency and to reduce the spot size[27]. The signal is recorded with a silicon avalanche photodiode (Excelitas SPCM-AQRH-16, photon detection efficiency at $950\,nm \sim 25\,\%$, dark count rate $14\,Hz$) in photon counting mode.
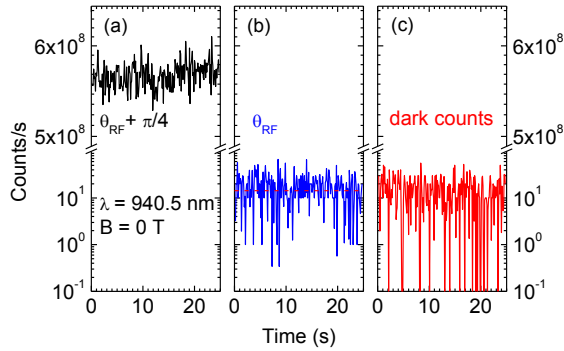
Fig. 1.2. Laser suppression. Reflected laser light is monitored at two different angles θ of the quarter-wave plate. At $\theta_{RF} + \pi/4$ (a) the laser is optimally transmitted, at $\theta = \theta_{RF}$ (b) it is optimally filtered. The count rate decreases from 580 MHz to 4 Hz (corrected for dark counts), corresponding to a laser suppression exceeding 8 orders of magnitude. A silicon avalanche photodiode in photon counting mode with a dark count rate of 14 Hz (c) is used to detect the laser light reflected from a quantum dot sample (GaAs plus thin metal layer, reflectivity $\sim 50\%$). The mean laser count rate (4 Hz) is less than the mean dark count rate (14 Hz). Integration time per point 0.1 s.

1.3.2 Laser suppression and long-term stability

In order to observe resonance fluorescence with a high signal-to-background ratio the microscope's laser suppression has to be high. The laser rejection can be determined by rotating the quarter-wave plate, switching between laser rejection maximally on and maximally off. The back-reflected laser light intensity depends periodically on the quarter-wave plate angle with a period of $\pi/2$. A laser suppression exceeding 10^8, corresponding to an optical density (OD) of 8 is achieved. (The OD is defined as $OD = -\log(1/T)$ with transmission T.) Fig. 1.2 shows a time trace of the detected laser light with and without laser rejection. An initial count rate of 580 MHz is reduced to 4 Hz by switching on the suppression. A single PBS achieves an extinction ratio of OD 5, a second PBS enhances the laser suppression. However, it is not increased by a further 5 orders of magnitude. We believe this difference is due to a stress induced birefringence of the PBSs, defining an upper limit for the laser suppression.

The effort to align the dark-field microscope is low. However, how stable is the alignment? Fig. 1.3 shows how the optical density depends on the quarter-wave plate angle: it is an extremely sensitive dependence. A change as small as a few m° can worsen the rejection by one order of magnitude. On the one hand, it emphasizes the need for a m° positioning resolution and on the other hand, the need for an extreme mechanical and thermal stability to achieve good long-term dark-field performance.

Despite the high sensitivity to the quarter-wave plate angle (Fig. 1.3), the long-term stability of the microscope is outstanding. It can be operated in a set-and-forget mode: an optical density close to 7, see Fig. 1.4, is achieved over an arbitrary period of time, exceeding typical measurement times by orders of magnitude.

1.4 Resonance fluorescence on a single quantum dot

Once the required high laser suppression is realized, the resonance fluorescence signal-to-background ratio on a single quantum dot is measured. Resonance fluorescence spectra of the single negatively charged exciton X^{1-} recorded at different laser powers and zero magnetic field are shown in Fig. 1.5. The lineshape of the optical resonance is Lorentzian, the full-width at half-maximum (FWHM) is $1.6\,\mu$eV at "low" power and $7.1\,\mu$eV at "high" power. The increase in linewidth with power reflects power broadening. Whereas the background, the residual laser signal, increases linearly with laser power, the quantum dot emission saturates and, thus, the signal-to-background ratio is power dependent. At an excitation power below quantum dot saturation the signal-to-background ratio is as high as $39,000:1$ (Fig. 1.5 (a)). Above saturation, a ratio $> 10^3:1$ (Fig. 1.5 (b)) is achieved.

One experiment which requires a high signal-to-background ratio and long integration times (and hence a stable set-up) is a $g^{(2)}$ measurement, i.e. an intensity correlation experiment. Laser light and a stream of single photons exhibit quite different $g^{(2)}(t=0)$
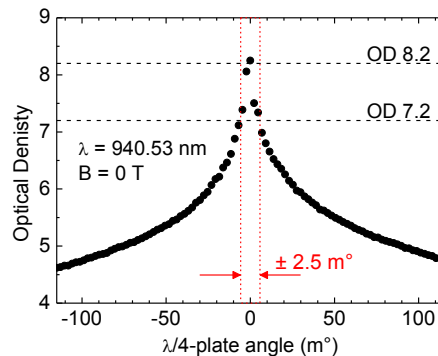
Fig. 1.3. Sensitivity of the laser suppression to the quarter-wave plate angle. The laser light reflected at the quantum dot sample (GaAs plus thin metal layer) is recorded by a silicon avalanche photodiode in photon counting mode as the quarter-wave plate angle is varied, and the corresponding optical density is calculated. At the angle of optimum laser rejection (OD > 8) a change in angle of only $2.5\,\text{m}^\circ$ causes the OD to decrease by one order of magnitude.
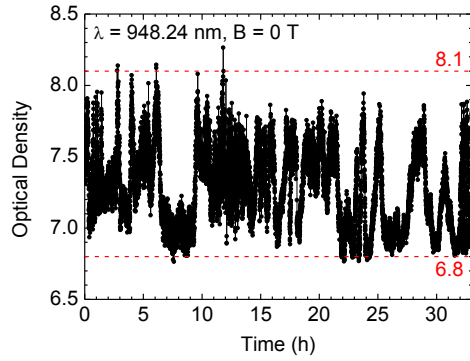
Fig. 1.4. Long-term behaviour. The microscope is aligned to reject the laser reflected at the quantum dot sample (GaAs plus thin metal layer) and the residual counts are recorded by a single photon detector. The optical density (OD), defined as $OD = -\log(1/T)$ with transmission T, is plotted as a function of time. The microscope is stable over many hours with an $OD > 6.8$.
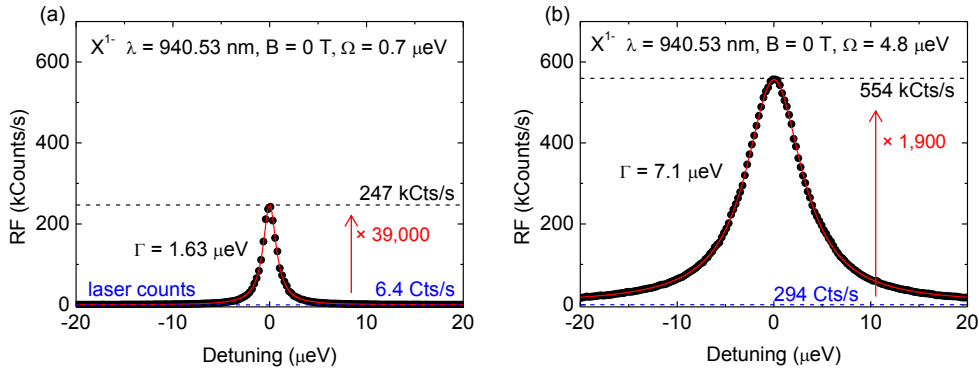
Fig. 1.5. Resonance fluorescence on a single InGaAs quantum dot with different optical Rabi couplings. Resonance fluorescence spectra are recorded with a single photon detector at constant laser frequency. Detuning is achieved by sweeping the gate voltage with respect to the laser frequency. (a) Below quantum dot saturation, at an excitation power corresponding to a Rabi energy Ω of $0.7\,\mu$eV, a signal-to-background ratio of $39,000 : 1$ is achieved. (b) At high pump power, where power broadening dominates the optical linewidth, a signal-to-background ratio $> 10^3 : 1$ is realized. Solid red lines show Lorentzian fits to the data (black points), blue dashed lines indicate the background.

values, 1 and 0, respectively, such that a leakage of laser light into the single photon stream is very detrimental. The time-dependence of $g^{(2)}$ was measured with a Hanbury Brown-Twiss interferometer (Fig. 1.6). There is a very clear dip at time delay zero, demonstrating anti-bunching in the photon statistics of the neutral exciton X^0. Note that even with a single channel count rate of $250\,$kHz, an integration time of ~ 9 hours was required to achieve a high signal-to-noise ratio in the $g^{(2)}$ measurement: the stability of the dark-field microscope was clearly important. It turns out that the residual value
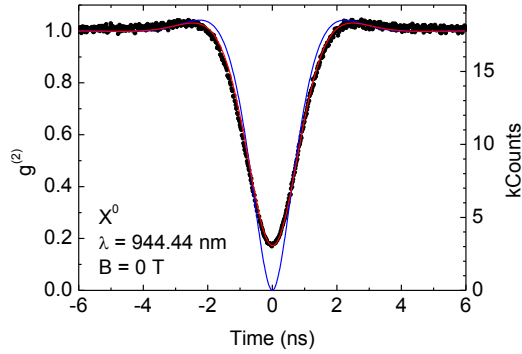
Fig. 1.6. $g^{(2)}$ measurement of the resonance fluorescence from the neutral exciton X^0 in a single InGaAs quantum dot. A clear dip at zero time delay demonstrates photon anti-bunching. The red curve shows the convolution of the two-level atom result [28], $g^{(2)}(t) = 1 - [\cos(\lambda t) + 3/(2\tau\lambda)\sin(\lambda t)]\exp[-3t/(2\tau)]$ with $\lambda = (\Omega^2 - 1/4\tau^2)^{1/2}$, Rabi frequency Ω and radiative lifetime τ, with the response of the detectors (Gaussian with FWHM 0.67 ns) and provides a very good description of the data (black points). The blue curve shows the two-level atom response only. A lifetime of $\tau = (1.0 \pm 0.1)$ ns and a Rabi frequency $\Omega = (0.9 \pm 0.1)\,\mu$eV were determined by fitting the data to the convolution. The measurement time was 9 hours with a single channel count rate of 250 kHz.

$g^{(2)}(t=0)$ is determined entirely (within the signal:noise) by the jitter in the detectors (~ 0.6 ns) which is comparable to the radiative decay time (~ 1 ns). Within error ($\sim 1\%$), the true quantum dot $g^{(2)}(t=0)$ is 0.00.

The resonance fluorescence, presented in Fig. 1.5 and Fig. 1.6, was measured on different excitons, the single negatively charged exciton X^{1-} and the neutral X^0, respectively. The resonance fluorescence of the X^0 is linearly polarized (π_x or π_y); the resonance fluorescence of the X^{1-} is unpolarized in the absence of a magnetic field, $B = 0$, circularly polarized (σ^+ or σ^-) for $B \neq 0$. The optics of the dark-field microscope define linear s for the excitation and linear p for the detection polarization. Nevertheless, resonance fluorescence of both optically active excitons can be measured independent of the selection rules, provided that the sample and microscope axes are not aligned. Ideally, the s/p basis is rotated by 45° with respect to the π_x/π_y basis.

The dark-field microscope works well across the entire ensemble of quantum dots spanning a bandwidth of about 60 nm in wavelength. The dark-field point is so sensitive to the polarization axes that small achromaticities in the polarizers play a role: a change in wavelength $\Delta\lambda$ requires a re-adjustment of the quarter-wave plate and linear polarizer alignments for optimum dark-field performance, typically a few tens of m° for $\Delta\lambda = 1$ nm. Furthermore, resonance fluorescence on a single quantum dot can be recorded not just at $B = 0$ but also at high B. At high B, a high suppression

12
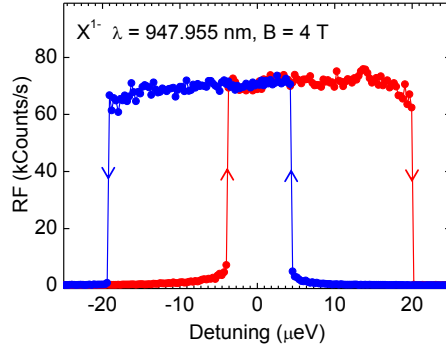
Fig. 1.7. Resonance fluorescence spectra of a single InGaAs quantum dot in a magnetic field. The laser suppression at high magnetic field is as good as that achieved at zero magnetic field. At $B = 4\,T$ the lineshape is a top hat and there is a hysteresis between forward and backward scanning directions. This effect is referred to as dragging[30,31].

of scattered laser light can be achieved. As for a change in wavelength, for optimum dark-field performance the quarter-wave plate and polarizer alignment have to be re-adjusted as the magnetic field increases. Crucial for the performance at high magnetic field is the linear polarizer angle, differing significantly ($\sim 10\,^\circ$) from the zero field angle probably due to a Faraday effect[29] of the objective lens, solid immersion lens or sample. Rotating the polarizer introduces a small p-polarization to the dominantly s-polarized beam propagating to the sample. A $10\,^\circ$ rotation results in a rotation of the polarization axis by $\sim 1\,^\circ$ on account of the properties of the PBS. A resonance fluorescence spectrum of an X^{1-} recorded at a magnetic field B of $4\,T$ is shown in Fig. 1.7. The lineshape of the optical resonance is clearly non-Lorentzian, and there is a hysteresis between forward (red) and backward (blue) detuning. A dynamic nuclear spin polarization locks the quantum resonance to the laser energy as the gate voltage is tuned, an effect referred to as dragging[30,31].

1.5 Outlook

As an outlook, we comment that the microscope can be developed further in some simple ways. For instance, given that the quantum dot basis (π_x/π_y) is dot-dependent[32], it may be valuable in the future to include also a way of rotating the microscope basis (s/p) relative to the π_x/π_y basis, either by inserting an additional wave plate or by rotating the sample. It may also be interesting to develop the capability of operating the microscope not with s/p polarizations but with σ^+/σ^- polarizations. Finally, we

note that the quantum efficiency of the resonance fluorescence collection is limited by the high refractive index of the sample: light is refracted to such large angles at the GaAs/vacuum interface that it is collected inefficiently. In this experiment, this situation was rectified to some degree (factor of ~ 5 in signal strength) by the solid immersion lens. Despite this low quantum efficiency, the rejection of the scattered laser light in our dark-field microscope is more than sufficient to observe background-free resonance fluorescence from single quantum dots. The next step is therefore to increase the collection efficiency: the dark-field performance is already more than good enough. Candidate structures are resonant micro-cavities, photonic nanowires, or, following the spirit of these experiments, ultra-high index solid immersion lenses.

References

1. Shields, A. J. *Nature Photon.* **1**, 215 (2007).

2. Warburton, R. J. *Nature Mater.* **12**, 483 (2013).

3. Kuhlmann, A. V., Houel, J., Ludwig, A., Greuter, L., Reuter, D., Wieck, A. D., Poggio, M., and Warburton, R. J. *Nature Phys.* **9**, 570 (2013).

4. Atatüre, M., Dreiser, J., Badolato, A., Högele, A., Karrai, K., and Imamoglu, A. *Science* **312**, 551–553 (2006).

5. Gerardot, B. D., Brunner, D., Dalgarno, P. A., Ohberg, P., Seidl, S., Kroner, M., Karrai, K., Stoltz, N. G., Petroff, P. M., and Warburton, R. J. *Nature* **451**, 441 (2008).

6. Press, D., Ladd, T. D., Zhang, B., and Yamamoto, Y. *Nature* **456**, 218–221 (2008).

7. Vamivakas, A. N. and Atatüre, M. *Contemp. Phys.* **51**, 17–36 (2010).

8. Högele, A., Seidl, S., Kroner, M., Karrai, K., Warburton, R. J., Gerardot, B. D., and Petroff, P. M. *Phys. Rev. Lett.* **93**, 217401 (2004).

9. Alén, B., Bickel, F., Karrai, K., Warburton, R. J., and Petroff, P. M. *Appl. Phys. Lett.* **83**, 2235–2237 (2003).

10. Karrai, K. and Warburton, R. J. *Superlattice Microst.* **33**, 311 – 337 (2003).

11. Kimble, H. J. *Nature* **453**, 1023–1030 (2008).

12. Muller, A., Flagg, E. B., Bianucci, P., Wang, X. Y., Deppe, D. G., Ma, W., Zhang, J., Salamo, G. J., Xiao, M., and Shih, C. K. *Phys. Rev. Lett.* **99**, 187402 (2007).

13. Ates, S., Ulrich, S. M., Reitzenstein, S., Löffler, A., Forchel, A., and Michler, P. *Phys. Rev. Lett.* **103**, 167402 (2009).

14. Nguyen, H. S., Sallen, G., Voisin, C., Roussignol, P., Diederichs, C., and Cassabois, G. *Appl. Phys. Lett.* **99**, 261904 (2011).

15. Ulhaq, A., Weiler, S., Ulrich, S. M., Roszbach, R., Jetter, M., and Michler, P. *Nature Photon.* **6**, 238–242 (2012).

16. Vamivakas, A. N., Zhao, Y., Lu, C. Y., and Atatüre, M. *Nature Phys.* **5**, 198 – 202 (2009).

17. Vamivakas, A. N., Lu, C. Y., Matthiesen, C., Zhao, Y., Fält, S., Badolato, A., and Atatüre, M. *Nature* **467**, 297–300 (2010).

18. Yilmaz, S. T., Fallahi, P., and Imamoglu, A. *Phys. Rev. Lett.* **105**, 033601 (2010).

19. Matthiesen, C., Vamivakas, A. N., and Atatüre, M. *Phys. Rev. Lett.* **108**, 093602 (2012).

20. Houel, J., Kuhlmann, A. V., Greuter, L., Xue, F., Poggio, M., Gerardot, B. D., Dalgarno, P. A., Badolato, A., Petroff, P. M., Ludwig, A., Reuter, D., Wieck, A. D., and Warburton, R. J. *Phys. Rev. Lett.* **108**, 107401 (2012).

21. Gao, W. B., Fallahi, P., Togan, E., Miguel-Sanchez, J., and Imamoglu, A. *Nature* **491**, 426–430 (2012).

22. Schuda, F., Jr, C. R. S., and Hercher, M. *J. Phys. B* **7**, L198 (1974).

23. Wu, F. Y., Grove, R. E., and Ezekiel, S. *Phys. Rev. Lett.* **35**, 1426–1429 (1975).

24. Novotny, L. and Hecht, B. *Principles of Nano-Optics.* Cambridge University Press, (2008).

25. Drexler, H., Leonard, D., Hansen, W., Kotthaus, J. P., and Petroff, P. M. *Phys. Rev. Lett.* **73**, 2252–2255 (1994).

26. Warburton, R. J., Schäflein, C., Haft, D., Bickel, F., Lorke, A., Karrai, K., Garcia, J., Schoenfeld, W., and Petroff, P. *Nature* **405**, 926 – 929 (2000).

27. Gerardot, B. D., Seidl, S., Dalgarno, P. A., Warburton, R. J., Kroner, M., Karrai, K., Badolato, A., and Petroff, P. M. *Appl. Phys. Lett.* **90**, 221106 (2007).

28. Loudon, R. *The Quantum Theory of light.* Oxford Science Publications, (2009).

29. Bennett, H. S. and Stern, E. A. *Phys. Rev.* **137**, A448–A461 (1965).

30. Latta, C., Högele, A., Zhao, Y., Vamivakas, A. N., Maletinsky, P., Kroner, M., Dreiser, J., Carusotto, I., Badolato, A., Schuh, D., Wegscheider, W., Atatüre, M., and Imamoglu, A. *Nature Phys.* **5**, 758–763 (2009).

31. Högele, A., Kroner, M., Latta, C., Claassen, M., Carusotto, I., Bulutay, C., and Imamoglu, A. *Phys. Rev. Lett.* **108**, 197403 (2012).

32. Seidl, S., Gerardot, B. D., Dalgarno, P. A., Kowalik, K., Holleitner, A. W., Petroff, P. M., Karrai, K., and Warburton, R. J. *Physica E* **40**, 2153–2155 (2008).

16

Chapter 2

Charge fluctuations in a semiconductor

We probe local charge fluctuations in a semiconductor via laser spectroscopy on a nearby self-assembled quantum dot. We demonstrate that the quantum dot is sensitive to changes in the local environment at the single charge level. By controlling the charge state of localized defects, we are able to infer the distance of the defects from the quantum dot with ± 5 nm resolution. The results identify and quantify the main source of charge noise in the commonly-used optical field-effect devices.

(Experiments and results presented in this chapter were obtained in close collaboration with Dr. Julien Houel, who wrote software for Monte Carlo simulations.)

2.1 Introduction

Condensed matter systems, notably quantum dots in III-V semiconductors and colour centres in diamond, are very attractive as the building blocks for quantum light sources[1] and spin qubits[2]. For instance, an InGaAs quantum dot is a robust, high repetition rate, narrow linewidth source of on-demand single photons and polarization-entangled photons, properties not shared by any other emitter. In the future, the demands placed on the quality of the single photons will increase. For instance, the creation of remote entanglement via photon interference and associated applications as a quantum repeater require Fourier-transform-limited single photons, i.e. wavepackets with a spectral bandwidth determined only by the radiative lifetime. This is hard to achieve in a semiconductor. On the one hand, a quantum dot is extremely sensitive to the local electric field via the Stark effect[3,4] leading to a stringent limit on the acceptable charge noise. Charge noise can also lead to spin dephasing[5,6]. On the other hand, phonons in the host semiconductor can lead to dephasing[7]. However, at low temperature and with weak optical excitation, phonon scattering is suppressed in a quantum dot by the strong quantum confinement[8,9], and the remaining broadening arises from relatively slow fluctuations of the environment leading to spectral fluctuations[10]. Transform-limited lines have not been routinely achieved, with typical optical linewidths a factor of at least 2 or 3 above the theoretical limit[10–13]. While spectral fluctuations in self-assembled quantum dots have been investigated with non-resonant excitation[14,15], their origin in the case of true resonant excitation is not known with any precision and are potentially complex with contributions from various sources of charge noise. Spin noise arising from the fluctuating nuclear spins can also play a role[16]. Notably, spectral fluctuations are a common feature in condensed matter systems, arising also in diamond[17], semiconductor nanocrystals[18] and nanowires[19].

We report new insights into local charge fluctuations in a semiconductor. High resolution laser spectroscopy on a single quantum dot is used as an ultra-sensitive sensor of the local environment. We observe single charge fluctuations in the occupation of a small number of defects located within ~ 100 nm of the quantum dot. We control the occupation of these close-by defects with an additional non-resonant excitation. Once the defects are fully occupied, there is a strong suppression of the charge noise. This understanding is tested in a new heterostructure in which the fluctuators are positioned further away from the quantum dot. As predicted by our model, this change reduces significantly the quantum dot optical linewidth.

2.2 Methods

2.2.1 Quantum dot sample

The InGaAs quantum dots are embedded in a Schottky diode[20,21], Fig. 2.1(a). They are separated from an n^+ back contact by a $d_{\mathrm{tun}} = 25$ nm thick GaAs tunnel barrier. Directly on top of the dots is a capping layer of thickness d_{cap}, 30 nm in samples A and B, followed by a blocking barrier, an AlAs/GaAs superlattice: $d_{\mathrm{SL}} = 120$ nm in sample A, 240 nm in sample B. Sample C has $d_{\mathrm{cap}} = 150$ nm and $d_{\mathrm{SL}} = 240$ nm. Samples B and C were grown under identical conditions. The samples are processed with Ohmic contacts to the back contact, grounded in the experiment, and with a semi-transparent gate electrode on the surface (5 nm NiCr sample A; 3/7 nm Ti/Au samples B and C) to which a gate voltage V_g is applied.
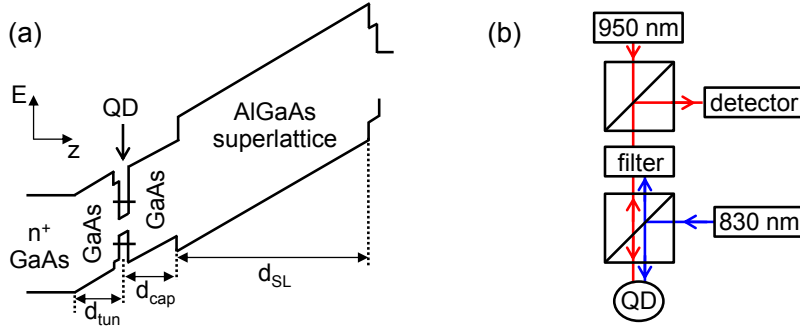
Fig. 2.1. (a) Band diagram of the devices. (b) The optical set-up for $\Delta R/R$ measurements.

2.2.2 Laser spectroscopy set-up

Laser spectroscopy is carried out on the charged exciton X^{1-} at 4.2 K by focusing the linearly-polarized output of a 1 MHz linewidth laser (external cavity semiconductor diode laser) to a ~ 0.5 μm spot on the sample surface. The power of the resonant laser is ~ 1 nW to avoid power broadening. The key advance here is to illuminate the sample simultaneously with a weak non-resonant source at 830 nm (edge-emitting laser diode), Fig. 2.1(b), with power P. Resonant excitation of the quantum dot is detected either with differential reflectivity $\Delta R/R$[22] including a filter to reject the 830 nm light, Fig. 2.1(b), or with resonance fluorescence exploiting a dark-field technique (see chapter 1). The integration time per point is typically 500 (250) ms in $\Delta R/R$ (resonance fluorescence). Spectra are recorded either by sweeping V_g (changing the

detuning via the Stark effect) or by tuning the laser.

2.3 Laser spectroscopy with simultaneous non-resonant excitation

Fig. 2.2(a) shows typical laser spectroscopy results both without and with "high" non-resonant excitation, $P = 325$ nW, for a quantum dot in sample A. In both cases, the absorption lines are close to Lorentzians with linewidth $2.5\,\mu$eV. The radiative lifetime at this wavelength is 800 ps[23], implying transform-limited linewidths of $0.8\,\mu$eV, a factor of 3 smaller than observed in the experiment. Other groups achieve similar linewidths[10–13]. The main effect of the non-resonant excitation is to shift the resonance to more negative voltages, in this case by $\Delta V_g = -80$ mV, for the same laser wavelength, equivalently a blue-shift of $\Delta E = 60\,\mu$eV for the same gate voltage, Fig. 2.2(a). Fig. 2.2(b) shows $\Delta R/R$ over 4 decades of P. Remarkably, the dot evolves from the low-P region (single Lorentzian line independent of P) to the high-P region (single Lorentzian line shifting monotonically with P) via a series of steps. These steps occur rather abruptly, over just a decade in P. For this particular quantum dot, 4 steps (equivalently 5 $\Delta R/R$ lines) are observed. The energy separation of the lines varies from about 4 to 10 μeV, and the linecuts, Fig. 2.3(c)-(e), show that within each line there is also a sub-structure. The observation of these absorption steps and their behaviour as a
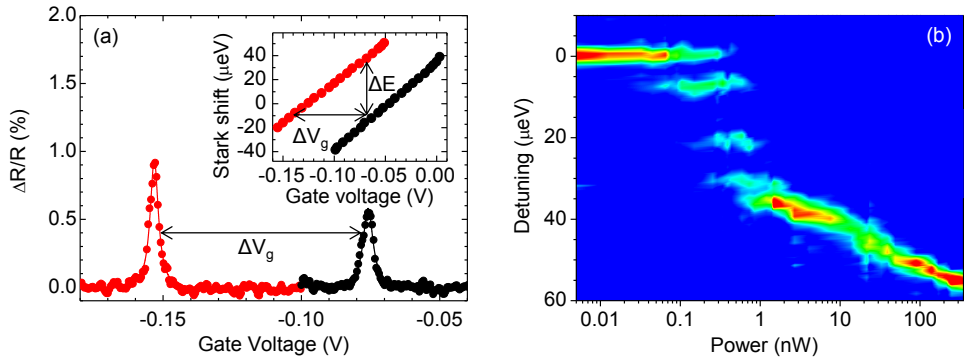
Fig. 2.2. (a) $\Delta R/R$ versus gate voltage for constant resonant laser wavelength (951.1150 nm) and power (1.0 nW) for a quantum dot in sample A ($d_{\text{cap}} = 30$ nm) both without (black) and with (red) $P = 325$ nW of 830 nm laser light. Solid lines show Lorentzian fits of the data. The inset shows the resonance position versus V_g. The Stark shift depends linearly on voltage away from the plateau edges; the Stark parameter decreases by only 10% at $P = 325$ nW. (b) Colour-scale plot (linear scale, blue: 0.061%; red: 0.61%) of $\Delta R/R$ versus non-resonant laser power P.

function of the control parameter P constitute our main experimental discovery.

We find that the $P = 0$ and $P = 100\,\mathrm{nW}$ behaviour are very similar for all dots. Also, the intrinsic properties (radiative lifetime, Stark shift, Coulomb shifts on charging) are all broadly similar. Despite this, the transition region is highly dot dependent. The number of steps lies typically between 3 and 6; the energy separations between the lines lie between ~ 4 and $20\,\mu\mathrm{eV}$ (sample A) with each quantum dot having its own unique "finger print" in the P-dependence. We therefore look for an explanation of the steps in terms of the dots' environment, i.e. a mesoscopic effect.

Our hypothesis is that non-resonant excitation creates holes at the capping layer/blocking barrier interface, Fig. 2.1(a). $830\,\mathrm{nm}$ light creates electron-hole pairs in the wetting layer. The electrons relax rapidly to the back contact, the holes to the capping layer/blocking barrier interface where at low temperature they can be trapped, creating a positive space charge in the device. The trapped holes mean that the same electric field is achieved at the location of the quantum dot only by applying a more negative voltage to the gate, consistent with Fig. 2.2(a). At large P, a 2D hole gas is formed, and the shift in V_g of the optical resonance allows the hole density N_h to be estimated. For intermediate P where we observe the steps, the hole density can be estimated for sample B to be $\sim 10^{10}\,\mathrm{cm}^{-2}$, similar to reported values at the metal-insulator transition[24]. The steps arise in the localization regime. In particular, the steps reflect a change of just one hole in occupation of the localization centres close to the dot. Quantitatively, occupying a localization centre immediately above a quantum dot at $d_{\mathrm{cap}} = 30\,\mathrm{nm}$ changes the electric field by $-1.50\,\mathrm{kVcm}^{-1}$ (taking into account the image charge in the back contact), shifting the optical resonance by $20\,\mu\mathrm{eV}$ via the Stark shift. This corresponds closely to the maximum observed step separation. This, and the agreement with our simulations (see section 2.4), justifies our hypothesis. Smaller steps arise from the occupation of localization centres which are laterally displaced.

Our interpretation leads to two immediate results. First, the location of the energy line of the quantum dot is a direct measure of the number of charges stored directly above the quantum dot. In the low-P regime, the quantum dot senses the nearby environment with single charge resolution. Secondly, the number of steps observed equals the number of holes which can be trapped above the dot, 4 for the dot in Fig. 2.2(d).

2.4 Monte Carlo simulations

We underpin our experimental results with a Monte Carlo simulation of the effects of occupying an array of valence band localization centres at the capping layer/blocking barrier interface (appendix A). We take an array of localization centres all distance d_{cap} above the quantum dots but at different locations $\mathbf{r}_i = (r_i, \theta_i)$ within the 2D plane. We position by hand a small number of localization centres, between 1 and 4, each with $r \leq 50\,\text{nm}$. Additionally, we take a full 2D array of randomly placed defects with 2D density N_{2D}. The occupation of a defect changes the local electric field at the quantum dot and hence the absorption spectrum via the Stark effect. This is calculated by, first, calculating the additional electrostatic potential; second, the associated electric field; and third, the energy shift of the exciton via the Stark effect. The Stark shift from the vertical electric field is calculated from the measured Stark effect, i.e. from the V_g-dependence of each particular quantum dot (modelled as a permanent dipole moment in an electric field[25]). The lateral electric field component cannot be accessed directly in the experiment but the effects are smaller: we assume that there is no linear term (i.e. no permanent dipole moment in the lateral plane) and that the quadratic component scales with the fourth power of the wave function extent of the quantum dot ground state which is known reasonably well[25]. The localization centres i are each occupied with a probability $\alpha_i p$ which rises with p, the control parameter in the simulation ($0 \leq p \leq 1$), until $\alpha_i p$ reaches 100%. α_i can vary from centre to centre and expresses the relative probability of occupying a particular centre. With a full 2D array, α_i depends on r_i through a Gaussian function with full-width-at-half-maximum (FWHM) Γ_L which describes the spatial extent of the non-resonant beam focus. For the defects directly above the quantum dot, the α_i are treated as fit parameters. For a fixed defect distribution and for a given p, we occupy the defects with a random number generator; from this charge distribution we calculate the net Stark shift, and at this energy we place a Lorentzian absorption spectrum with FWHM Γ. The process is repeated N times, keeping the defect distribution constant but each time creating a new charge distribution with the random number generator. The whole procedure is then repeated as a function of p. We model the experiment by relating p linearly to the control parameter P. Further details are provided in appendix A.

Our simulation reproduces the steps in the absorption spectra as a function of P for sample A, adding considerable weight to our assertion that the charge fluctuations arise from trapped holes at the capping layer/blocking barrier interface. The exact energy steps turn out to be very sensitive to the locations r_i of the localization centres.
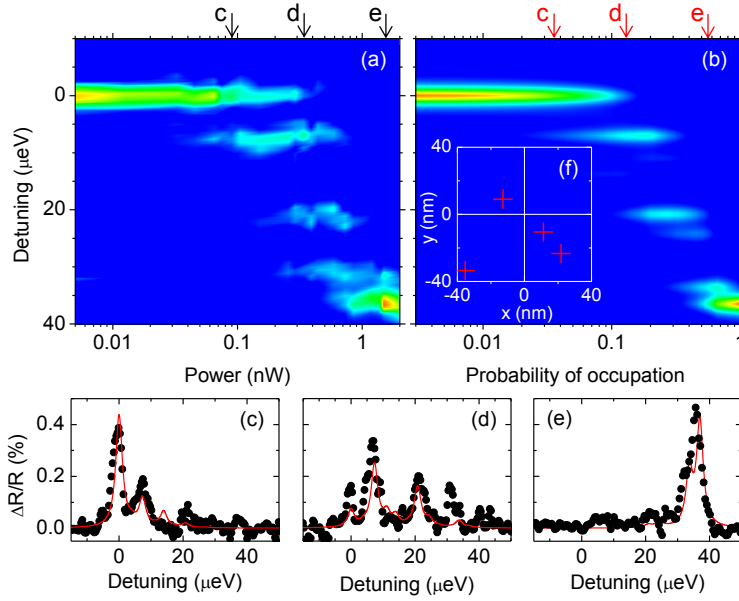
Fig. 2.3. (a) $\Delta R/R$ versus P for a quantum dot in sample A, as in Fig. 2.2(b). (b) Monte Carlo simulation with 4 hole localization centres located above the dot with $r_i = (32.0, 15.4, 15.7, 48.8)$ nm, $\alpha_i = (5.0, 1.5, 1.5, 1.0)$, $\Gamma = 2.5\,\mu$eV, $\Gamma_L = 1.0\,\mu$m and $N = 2,500$ (parameters described in the text). (c)-(e) Line cuts showing experimental data at $P = 0.09, 0.34, 1.39$ nW (black) and simulation results for $p = 0.042, 0.16, 0.65$ (red). (f) Lateral location of localization centres with dot at $\mathbf{r} = 0$.

(The dependence on θ_i is much weaker.) We can match the energies of the steps, their P-dependence and the substructure within each step with a set of r_i and $N_{2D} = 0$. However, we need to depart from $\alpha_i = 1$ to reproduce the relative intensities of the various lines (appendix A). Fig. 2.3 shows the result of this procedure: the Monte Carlo simulation, Fig. 2.3(b), reproduces the main experimental features, Fig. 2.3(a). Furthermore, the line-cuts at specific P are in very close agreement with the complicated experimental spectra, Fig. 2.3(c)-(e). The localization centre array is shown in Fig. 2.3(f). The different α_i presumably reflect some connectivity between the localization centres such that a "deep" one is much more likely to be occupied than a "shallow" one. The energy shifts on adding holes to these defects one by one are so sensitive to the set of r_i that the random error on each r_i is as small as ± 5 nm. In this sense, the experiment provides $\sim \lambda/100$ spatial resolution in the spacings between the localization centres. The high spatial resolution, well beyond the conventional diffraction limit, relies on the interpretation of the precisely-measured energy shifts as holes are added one by one. An analogy can be drawn to a completely different system, a conjugated polymer, where the locations of localized charges have been determined with very high resolution, in

this case via the adverse influence of the trapped charge on the fluorescence intensity[26]. Both techniques do not produce a direct image, but in both cases, interpreting the optical data with a model allows a mapping of the local environment.

We have attempted to reproduce results such as those in Fig. 2.3(a) with just a random distribution of localization centres, $N_{2D} \neq 0$. The large net shift between P "low" and "high" pins down N_{2D} to $\sim 10^{10}$ cm^{-2}. For this N_{2D}, the Monte Carlo simulations predict only in very rare cases $3 - 5$ steps (appendix A) yet this is the standard experimental result. Furthermore, in the simulation for $N_{2D} \sim 10^{10}$ cm^{-2}, each line has a strong P-dependence (appendix A), not a feature in the experiment. In the simulations, the only configurations which describe sample A are those with a cluster of localization centres immediately above the dots with otherwise a sparse distribution for $r \leq 100$ nm, an extremely unlikely outcome with a random distribution of localization centres. The conclusion is that the localization centres are not randomly distributed in the 2D plane. Instead, the dot itself induces the formation of a small number of localization centres directly above it. The mechanism for this is likely to be the strain field which extends beyond the quantum dot in combination with roughness at the capping layer/blocking layer interface.

2.5 Quantum dot optical linewidth: towards the transform-limit

Sample A has $\Gamma = 2.5\,\mu$eV, well above the transform-limit. As described above, this is unlikely to be related to fluctuations in a 2D array of localization centres at the capping layer/blocking barrier interface. The origin of this broadening is not known precisely but there are hints that it is related to the surface of the device. We switch to sample B which clearly demonstrates the consequences of a fluctuating 2D array. Fig. 2.4(a) shows resonance fluorescence from a single dot in sample B. At $P = 0$, the FWHM is comparable to those of dots in sample A but there are large fluctuations in the signal which are not reproducible from one spectrum to the next. The fluctuations disappear only when we integrate for more than 50 s per point, Fig. 2.4(c), demonstrating that they have a component at very low frequency (sub-Hz). A characteristic feature is the rather abrupt turn on at negative detunings and the abrupt turn off at positive detunings. Turning on the non-resonant excitation reveals also a series of steps (appendix A), as in Fig. 2.2(b), and at "high" P, this sub-Hz frequency component is eliminated. We interpret the $P = 0$ results with the Monte Carlo simulations, Fig. 2.4(b), with the hypothesis that the μeV-scale fluctuations in Fig. 2.4(a) arise from fluctuations amongst
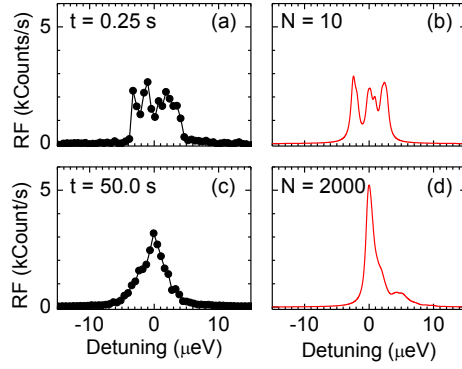
Fig. 2.4. Resonance fluorescence from a single quantum dot in sample B (1.0 nW at $\lambda = 962.2500$ nm) at $P = 0$ with integration time per point 0.25 s in (a), 50.0 s in (c). Monte Carlo simulation with $N_{2D} = 1.0 \times 10^{10}$ cm^{-2}, $\Gamma = 0.8\,\mu$eV, $\Gamma_L = 10.0\,\mu$m, $p = 4.4\%$ (to represent $P = 0$) with $N = 10$ in (b), $N = 2000$ in (d).

a large number of localization centres all with $r \leq 100$ nm. With this hypothesis we can reproduce the experiment, Fig. 2.4(b),(d), provided p is small, i.e. the defects are each occupied with small probability. The defects (two in this case) directly above the quantum dot are therefore unlikely to be occupied. Only a small fraction of the available configurations are occupied within the measurement time, leading to the spectrum-to-spectrum changes. Fig. 2.4(b) reproduces the abrupt turn on/turn off of the spectrum, the FWHM, and the characteristic energy splitting between the sub-peaks using $N_{2D} = 1.0 \times 10^{10}$ cm^{-2}, $p = 4.4\%$ and $N = 10$. Significantly, the jagged nature of the spectra in Fig. 2.4(a) can only be reproduced with a small homogeneous broadening, $\Gamma = 0.8\,\mu$eV. This is evidence that on short enough time scales, the defect occupation is frozen, and the dot's optical linewidth is close to transform-limited. The behaviour for longer integration times, Fig. 2.4(c), is reproduced in the simulations with the same parameters but by increasing N, the number of hole configurations, in accordance with the integration time in the experiment, Fig. 2.4(d).

A key conclusion for sample B is that local fluctuations of hole charges are responsible for the spectral fluctuations and an increase in the optical linewidths in time-integrated spectra above the transform-limit. This conclusion can be tested by increasing the capping layer thickness in order to position the fluctuators further from the quantum dots: this should reduce the hole-induced electric field at the location of the dots by ensuring a closer match between the electric field from an occupied defect and its image charge. Fig. 2.5 shows resonance fluorescence from a dot in sample C with an increased capping layer thickness, $d_{cap} = 150$ nm. There are two striking features. First, the
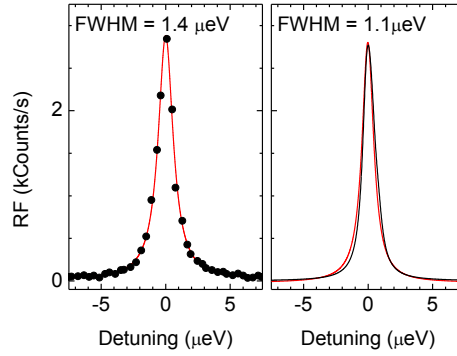
Fig. 2.5. (a) Resonance fluorescence (0.25 nW at $\lambda = 951.6040$ nm, $P = 0$, 0.25 s integration time) from a dot in Sample C with $d_{\mathrm{cap}} = 150$ nm (black points; red line Lorentzian fit). (b) Monte Carlo simulation using $N_{2D} = 1.0 \times 10^{10}$ cm^{-2}, $\Gamma = 0.8\,\mu$eV, $N = 10$, $p = 4.4\%$ (black points; red line Lorentzian fit).

linewidth has reduced to $1.4\,\mu$eV. The average linewidth for quantum dots in sample C is $1.60\,\mu$eV with standard deviation $0.22\,\mu$eV. Second, the fluctuations in Fig. 2.4(a) disappear. We attempt to reproduce this behaviour in the simulations by keeping N_{2D}, Γ, N and N_h exactly the same as for sample B, changing only the capping layer thickness, Fig. 2.5(b). This results in a close-to-Lorentzian line with FWHM $1.1\,\mu$eV, Fig. 2.5(b), in very close agreement with the experiment. Quantitative understanding of the valence band localization centres has therefore been achieved.

Achieving transform-limited optical linewidths requires controlling these trapped holes. Eliminating these holes completely may be challenging: the hole density ($N_h = pN_{2D}$) estimated in sample B at $P = 0$ is very small. We find that N_h is not related to the weak resonant excitation but it is roughly consistent with the p-type background doping of $\sim 10^{14}$ cm^{-3}. A large capping layer in a field-effect structure is an important step in reducing charge noise as it positions the fluctuating charges far enough from the quantum dots for their influence to be minimized.

26

References

1. Shields, A. J. *Nature Photon.* **1**, 215 (2007).

2. Hanson, R. and Awschalom, D. D. *Nature* **453**, 1043–1049 (2008).

3. Alén, B., Bickel, F., Karrai, K., Warburton, R. J., and Petroff, P. M. *Appl. Phys. Lett.* **83**, 2235–2237 (2003).

4. Vamivakas, A. N., Zhao, Y., Fält, S., Badolato, A., Taylor, J. M., and Atatüre, M. *Phys. Rev. Lett.* **107**, 166802 (2011).

5. Greilich, A., Carter, S. G., Kim, D., Bracker, A. S., and Gammon, D. *Nature Photon.* **5**, 703–709 (2011).

6. De Greve, K., McMahon, P. L., Press, D., Ladd, T. D., Bisping, D., Schneider, C., Kamp, M., Worschech, L., Hoefling, S., Forchel, A., and Yamamoto, Y. *Nature Phys.* **7**, 872–878 (2011).

7. Ramsay, A. J., Gopal, A., Gauger, E. M., Nazir, A., Lovett, B. W., Fox, A. M., and Skolnick, M. S. *Phys. Rev. Lett.* **104**, 017402 (2010).

8. Bayer, M., Ortner, G., Stern, O., Kuther, A., Gorbunov, A. A., Forchel, A., Hawrylak, P., Fafard, S., Hinzer, K., Reinecke, T. L., Walck, S. N., Reithmaier, J. P., Klopf, F., and Schäfer, F. *Phys. Rev. B* **65**, 195315 (2002).

9. Langbein, W., Borri, P., Woggon, U., Stavarache, V., Reuter, D., and Wieck, A. D. *Phys. Rev. B* **70**, 033301 (2004).

10. Högele, A., Seidl, S., Kroner, M., Karrai, K., Warburton, R. J., Gerardot, B. D., and Petroff, P. M. *Phys. Rev. Lett.* **93**, 217401 (2004).

11. Atature, M., Dreiser, J., Badolato, A., Hogele, A., Karrai, K., and Imamoglu, A. *Science* **312**, 551–553 (2006).

12. Xu, X., Sun, B., Berman, P. R., Steel, D. G., Bracker, A. S., Gammon, D., and Sham, L. J. *Science* **317**, 929–932 (2007).

13. Vamivakas, A. N., Zhao, Y., Lu, C. Y., and Atatuere, M. *Nature Phys.* **5**, 198–202 (2009).

14. Robinson, H. D. and Goldberg, B. B. *Phys. Rev. B* **61**, R5086–R5089 (2000).

15. Berthelot, A., Favero, I., Cassabois, G., Voisin, C., Delalande, C., Roussignol, P., Ferreira, R., and Gerard, J. M. *Nature Phys.* **2**, 759–764 (2006).

16. Latta, C., Högele, A., Zhao, Y., Vamivakas, A. N., Maletinsky, P., Kroner, M., Dreiser, J., Carusotto, I., Badolato, A., Schuh, D., Wegscheider, W., Atatüre, M., and Imamoglu, A. *Nature Phys.* **5**, 758–763 (2009).

17. Robledo, L., Bernien, H., van Weperen, I., and Hanson, R. *Phys. Rev. Lett.* **105**, 177403 (2010).

18. Müller, J., Lupton, J. M., Rogach, A. L., Feldmann, J., Talapin, D. V., and Weller, H. *Phys. Rev. Lett.* **93**, 167402 (2004).

19. Sallen, G., Tribu, A., Aichele, T., Andre, R., Besombes, L., Bougerol, C., Richard, M., Tatarenko, S., Kheng, K., and Poizat, J. *Nature Photon.* **4**, 696–699 (2010).

20. Drexler, H., Leonard, D., Hansen, W., Kotthaus, J. P., and Petroff, P. M. *Phys. Rev. Lett.* **73**, 2252–2255 (1994).

21. Warburton, R. J., Schäflein, C., Haft, D., Bickel, F., Lorke, A., Karrai, K., Garcia, J., Schoenfeld, W., and Petroff, P. *Nature* **405**, 926 – 929 (2000).

22. Alén, B., Högele, A., Kroner, M., Seidl, S., Karrai, K., Warburton, R. J., Badolato, A., Medeiros-Ribeiro, G., and Petroff, P. M. *Appl. Phys. Lett,* **89**, 123124 (2006).

23. Dalgarno, P. A., Smith, J. M., McFarlane, J., Gerardot, B. D., Karrai, K., Badolato, A., Petroff, P. M., and Warburton, R. J. *Phys. Rev. B* **77**, 245311 (2008).

24. Simmons, M. Y., Hamilton, A. R., Pepper, M., Linfield, E. H., Rose, P. D., Ritchie, D. A., Savchenko, A. K., and Griffiths, T. G. *Phys. Rev. Lett.* **80**, 1292–1295 (1998).

25. Warburton, R. J., Schulhauser, C., Haft, D., Schaflein, C., Karrai, K., Garcia, J. M., Schoenfeld, W., and Petroff, P. M. *Phys. Rev. B* **65**, 113303 (2002).

26. Bolinger, J. C., Traub, M. C., Adachi, T., and Barbara, P. F. *Science* **331**, 565–567 (2011).

Chapter 3

Charge noise and spin noise in a semiconductor

Solid-state systems which mimic two-level atoms are being actively developed. Improving the quantum coherence of these systems, for instance spin qubits or single photon emitters using semiconductor quantum dots, involves dealing with noise. The sources of noise are inherent to the semiconductor device and are complex. Charge noise results in a fluctuating electric field, spin noise in a fluctuating magnetic field at the location of the qubit, and both can lead to dephasing and decoherence of optical and spin states. We investigate noise in an ultra-pure semiconductor device using a minimally-invasive, ultra-sensitive, local probe: resonance fluorescence from a single quantum dot. We distinguish between charge noise and spin noise via a crucial difference in their optical signatures. Noise spectra for both electric and magnetic fields are derived from 0.1 Hz to 100 kHz. The charge noise dominates at low frequencies, spin noise at high frequencies. The noise falls rapidly with increasing frequency allowing us to demonstrate transform-limited quantum dot optical linewidths by operating the device above 50 kHz.

3.1 Introduction

Semiconductor quantum dots are hosts for spin qubits [1,2]. Optically-active quantum dots, for instance self-assembled quantum dots, are in addition potentially excellent single photon sources [3]. Optimizing performance demands an understanding of noise and a strategy to circumvent its deleterious effects [4]. There are two main sources of noise in a semiconductor. Charge noise arises from occupation fluctuations of the available states and leads to fluctuations in the local electric field. This results in shifts in the optical transition energy of a quantum dot via the dc Stark effect and is one mechanism by which the optical linewidth of a self-assembled quantum dot can be significantly increased above the transform limit [5–7]. Charge noise can also result in spin dephasing via the spin-orbit interaction, and, in particular for hole spins, via the electric field dependence of the g-factor [8,9]. The second source of noise, spin noise, arises typically from fluctuations in the nuclear spins of the host material and, on account of the hyperfine interaction, results in a fluctuating magnetic field (the Overhauser field) experienced by an electron spin [10,11]. Spin noise from noisy nuclei results in rapid spin dephasing in an InGaAs quantum dot [12–14].

Strategies for reducing noise involve working with ultra-clean materials to minimize charge noise, and possibly nuclear spin-free materials to eliminate spin noise. Abandoning GaAs comes however with a significant loss of flexibility for both spin qubits and quantum photonics applications. A second powerful paradigm is the use of dynamic decoupling, schemes which employ complex echo-like sequences to "protect" the qubit from environmental fluctuations [15–17]. In this case, it is absolutely crucial that the noise power decreases with increasing frequency.

For quantum dot-based single photon sources, the linewidths are in the best case (high quality material with resonant excitation) typically about a factor of two larger than the transform limit in which the linewidth is determined only by the radiative decay time [5–7]. This is a poor state of affairs for applications which rely on photon indistinguishability, the resource underpinning a quantum repeater for instance. On the positive side, there is evidence that with low power, resonant excitation, there is no significant upper level dephasing apart from radiative recombination [18,19]. It has been surmised that the increase in linewidth above the ideal limit arises from a spectral wandering [5,7] but the origin of the noise and its frequency dependence has not been pinned down. Concerning spin qubits, untreated noisy nuclei limit the electron spin coherence qubit [10,11]. However, the mesoscopic nature – a quantum dot contains $10^5 - 10^6$ nuclear spins – allows the nuclear spins to be manipulated, both quietened down
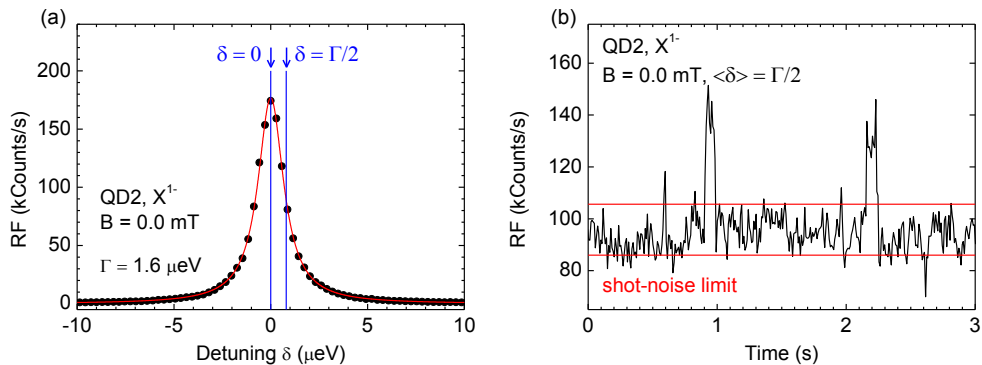
Fig. 3.1. Resonance fluorescence (RF) on a single quantum dot. (a) RF recorded on a single InGaAs quantum dot at wavelength 950.61 nm at a power corresponding to a Rabi energy of 0.55 μeV at a temperature of 4.2 K without external magnetic field. The RF was detected with a silicon avalanche photo-diode operating in single photon mode; the detuning was achieved by sweeping the gate voltage with respect to the laser using the dc Stark effect. In this case, the integration time per point was 100 ms. The solid line is a Lorentzian fit to the data with linewidth $\Gamma = 1.6$ μeV (390 MHz). (b) A time-trace of the RF recorded with detuning set to half the linewidth, $\langle \delta \rangle = \Gamma/2$. The arrival time of each detected photon is stored allowing a time trace to be constructed post-experiment with an arbitrary binning time. An example is shown using a binning time of 10 ms.

and polarized[20].

Some progress has been made in understanding noise in semiconductor quantum devices. In the context of quantum transport, a spin noise spectrum has been deduced at high frequencies from the time dependence of spin qubit dynamic decoupling[21], and at low frequencies from successive spin qubit readout operations[22], leaving a gap at intermediate frequencies[23]. A spin noise spectrum has also been determined via the Faraday rotation of a detuned laser on an ensemble of quantum dots[24] but not at the local, single quantum dot level.

We present here an investigation of noise in an ultra-clean semiconductor quantum device, using a minimally-invasive, ultra-sensitive, local probe: resonance fluorescence (RF) from a single quantum dot, Fig. 3.1(a). We present noise spectra with 6 decades of resolution in the noise power over 6 decades of frequency, from 0.1 Hz to 100 kHz, Fig. 3.2. Significantly, we have discovered a spectroscopic way to distinguish charge noise from spin noise, Fig. 3.3. We find that the charge noise gives large noise powers but only at low frequencies. The spin noise gives much weaker noise powers but over a much larger bandwidth. Remarkably, our experiment is able to reveal the full spectrum of the fluctuating nuclear spin ensemble. We translate the resonance fluorescence noise spectrum into two separate noise spectra, one for the local electric field (charge noise) and

one for the local magnetic field (spin noise). The charge noise spectrum is Lorentzian with a small $1/f$-like component; the spin noise spectrum is purely Lorentzian, falling as $1/f^2$ at "high" frequency. The combined noise falls rapidly with frequency becoming insignificant above 50 kHz for the quantum dot optical transition as signalled by transform-limited linewidths.

A typical time trace of the RF is shown in Fig. 3.1(b) with binning time 10 ms. At first sight, one might think that the time trace is unlikely to be very revealing about the local environmental noise as the experiment itself and not just the quantum dot is a source of noise, mostly shot noise. However, this experimental noise is highly reproducible. We record its spectrum carefully and, using a protocol (see appendix B) subtract it from the total noise to determine the noise power of the normalized RF signal, $N_{\mathrm{QD}}(f)$.

3.2 Charge noise versus spin noise

$N_{\mathrm{QD}}(f)$ is shown in Fig. 3.2. In this case, the gate voltage V_g is set so that the quantum dot contains a single electron and the laser drives the trion resonance, X^{1-}. Two features can be made out in the noise spectrum, a roll-off-like spectrum with "high" power and "low" characteristic frequency, and a roll-off-like spectrum with "low" power and "high" characteristic frequency. This points to the presence of two noise sources in the semiconductor.
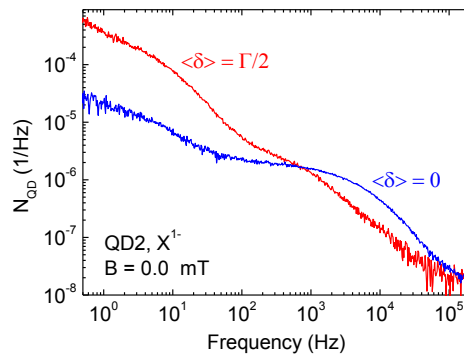
Fig. 3.2. Resonance fluorescence noise. RF noise spectra recorded on a quantum dot occupied with a single electron, the trion X^{1-}, for average detuning equal to zero, $\langle \delta \rangle = 0$ (blue), and for $\langle \delta \rangle = \Gamma/2$ (red) at 4.2 K and $B = 0.0$ mT. Following the scheme in Fig. 3.3, the noise at low frequencies is shown to originate from charge noise, that at high frequencies from spin noise. Plotted is the noise power spectrum of the normalized RF, $S(t)/\langle S(t) \rangle$, where $S(t)$ is the RF signal, $\langle S(t) \rangle$ the average RF signal, corrected for external sources of noise (see appendix B).

To identify the two noise sources, we present noise spectra taken with two detunings, one with detuning averaged over the experiment zero $\langle \delta \rangle = 0$, the other with average detuning half a linewidth, $\langle \delta \rangle = \Gamma/2$, Fig. 3.2. Switching from $\langle \delta \rangle = 0$ to $\langle \delta \rangle = \Gamma/2$ causes the noise power of the low frequency component to increase by about one order of magnitude and the power of the high frequency component to decrease (by about a factor of three at a few kHz), Fig. 3.2. This crucial information allows the nature of the noise, charge or spin, to be identified.

As the local electric field F fluctuates, the detuning δ of the quantum dot optical resonance with respect to the constant laser frequency fluctuates on account of the dc Stark effect. For small electric field fluctuations, the Stark shift is linear: the optical resonance shifts rigidly backwards and forwards on the detuning axis, as shown in Fig. 3.3(a),(b). The response in the RF to charge noise has a first order component in electric field for $\delta = \Gamma/2$ giving rise to large changes in the RF. Conversely, for $\delta = 0$ the first order component vanishes. Sensitivity to charge noise in the RF is therefore weak for $\langle \delta \rangle = 0$ yet strong for $\langle \delta \rangle = \Gamma/2$. Spin noise results in a complementary behaviour in the absence of an external magnetic field, $B = 0$. Fluctuations in the local magnetic field B_N arising from spin noise do *not* shift the X^{1-} resonance backwards and forwards. Instead, a typical B_N fluctuation induces a sub-linewidth Zeeman splitting of the X^{1-} resonance, as shown in Fig. 3.3(d). An oscillatory B_N results in a "breathing motion" of the RF spectrum. Sensitivity to spin noise in the RF is therefore strong for $\langle \delta \rangle = 0$, weak for $\langle \delta \rangle = \Gamma/2$. The crucial point is that, for X^{1-} at $B = 0$, the dependence of the RF noise on $\langle \delta \rangle$ is *opposite* for charge noise and spin noise. Applying this concept to the quantum dot response in Fig. 3.2 leads to the unambiguous conclusion that the noise at low frequencies arises from charge noise and that the noise at high frequencies arises from spin noise. The noise spectrum at $\langle \delta \rangle = 0$ measured on an empty quantum dot, driving the neutral exciton X^0 transition, also shows two noise features, again charge noise and spin noise, Fig. 3.5(a). The X^0 and X^{1-} have similar levels of charge noise. This is expected as the X^0 and X^{1-} dc Stark shifts are similar and each exciton probes exactly the same environment. The X^0 spin noise is less however. Part of the explanation is that the X^0 splits into two states even at $B = 0$ (the so-called fine structure, a consequence of an anisotropy in the electron-hole exchange) such that the dispersion for small B_N is quadratic and not linear, reducing massively the sensitivity of X^0 to spin noise (see appendix B).

The noise behaviour X^0 versus X^{1-} supports the charge/spin assignment of the noise processes. Further confirmation is provided in Fig. 3.6 which shows $N_{\mathrm{QD}}(f)$ curves measured on the same quantum dot over the course of the experiment (several months)
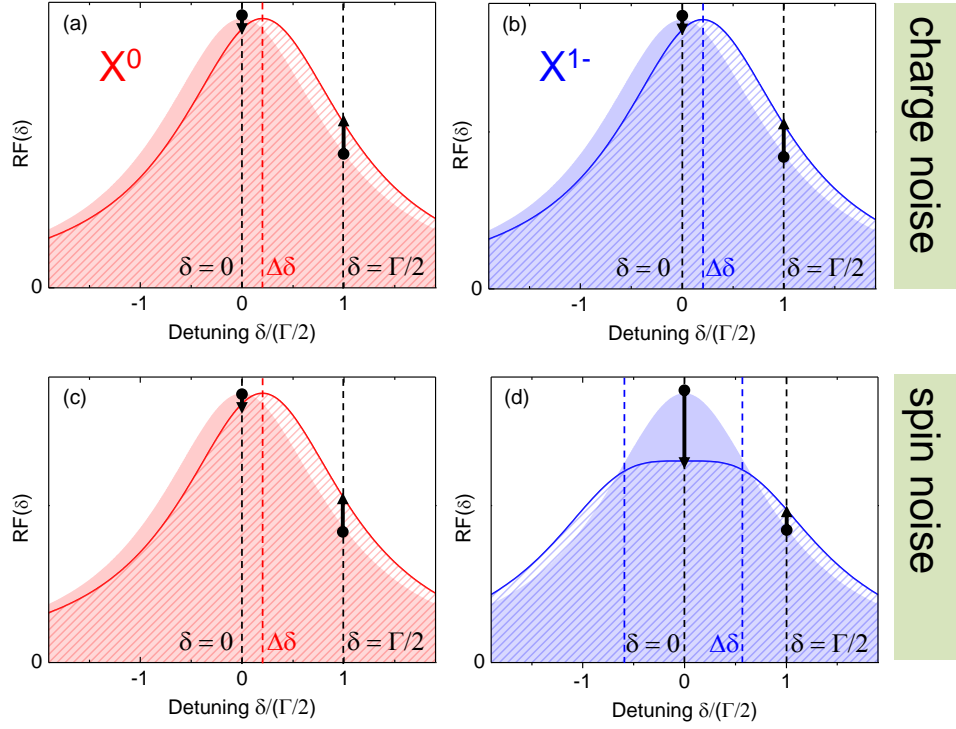
Fig. 3.3. Distinguishing between charge noise and spin noise. (a)-(d) Schematic showing the effect of charge noise and spin noise on the neutral, X^0, and charged, X^{1-}, excitons (applied magnetic field zero). Charge noise (noise in the local electric field) results in a "rigid" shift of the optical resonance leading to a small change in resonance fluorescence (RF) for zero detuning $\delta = 0$ and a large change in RF at $\delta = \Gamma/2$. This applies for both X^0 and X^{1-}, (a), (b). Without an external magnetic field, spin noise (noise in the local magnetic field experienced by a conduction electron) results in a small shift in the X^0 resonance position, qualitatively as for charge noise, (c). (d) For X^{1-} however, spin noise induces a Zeeman splitting in the resonance resulting in a large change in RF at $\delta = 0$ and a small change in RF at $\delta = \Gamma/2$ (zero for $\delta = \Gamma/2\sqrt{3}$), opposite to charge noise. This difference, a "rigid" shift of the X^{1-} resonance from charge noise, a "breathing motion" in the X^{1-} resonance from spin noise, allows charge noise and spin noise to be identified.

under nominally identical conditions. There are changes in the low frequency noise power (up to a factor of 10) but the high frequency noise remains exactly the same. It is known that the charge state of the sample can change depending on the sample's history: these charge rearrangements result in changes in charge noise at low frequency. The spin noise arises from the host nuclear spins of the quantum dot which remain the same and retain their properties: this results in the unchanging spin noise at high frequency. Further confirmation in the charge/spin assignment comes from noise spectra in a small B (see appendix B).

3.3 Noise levels

Once the noise sources have been identified, the simple rules (see Supplementary Information) connecting RF intensity with the local electric field F (charge noise) and with the local magnetic field B_N (spin noise) allow quantitative statements on the noise to be made. The charge noise has root-mean-square (rms) electric field noise $F_{\mathrm{rms}} = 0.46$ Vcm^{-1} (bandwidth starting at 0.1 Hz). It is striking that, first, the charge noise is very small: the rms noise in the local potential is just 1.2 μV. This is a consequence of both the ultra-pure material and also the carefully controlled experimental conditions. The sensitivity of the quantum dot to the small levels of charge noise via the Stark effect reflects on the one hand, the potential of quantum dots as ultra-sensitive electrometers[7,25,26]; and, on the other hand, the difficulty in generating transform-limited single photons from individual quantum dots. Secondly, it is striking that the charge noise is concentrated at such low frequencies.

The rms noise in the Overhauser field measured on X^0 amounts to $B_{N,\mathrm{rms}} = 193$ mT with a characteristic frequency 180 kHz (correlation time 5.5 μs). $B_{N,\mathrm{rms}}$ measured on X^{1-} is smaller, 9 mT, with correlation time 100 μs (see Supplementary Information). The random fluctuations of N nuclear spins lead to a $B_{N,\mathrm{rms}}$ which scales as $1/\sqrt{N}$[10,11]; applied to an InGaAs quantum dot with $N \sim 10^5$, the expectation is $B_{N,\mathrm{rms}} \sim 20$ mT[27,28]. On X^0, the large $B_{N,\mathrm{rms}}$ and small correlation time both provide clear evidence that continuous resonant X^0 excitation agitates the nuclear spins. The X^0 and X^{1-} correlation times, a few tens of μs, identify the process responsible for the spin noise as the nuclear spin dipole-dipole interaction[10] (see appendix B).

3.4 Quantum dot optical linewidth

A clear result is that both charge and spin noise fall rapidly with increasing frequency such that above 100 kHz, the RF noise power reduces by about 4 orders of magnitude compared to the low frequency limit. The noise curves predict therefore that the exciton dephasing processes are slow relative to radiative decay which occurs at a GHz rate. To explore this, we measure the X^0 linewidth as the measurement frequency f_{scan} is gradually increased (see appendix B). Fig. 3.4(c) shows that the RF linewidth Γ decreases from 1.60 μeV to 0.93 μeV as f_{scan} increases from 1 Hz to 50 kHz. At higher f_{scan}, Γ remains constant. Furthermore, within our experimental error (0.1 μeV), this constant value at high f_{scan} corresponds to the transform limit, Γ_0. A transform-limited RF spectrum is shown in Fig. 3.4(a). In other words, the increase in Γ over Γ_0 at low f_{scan}
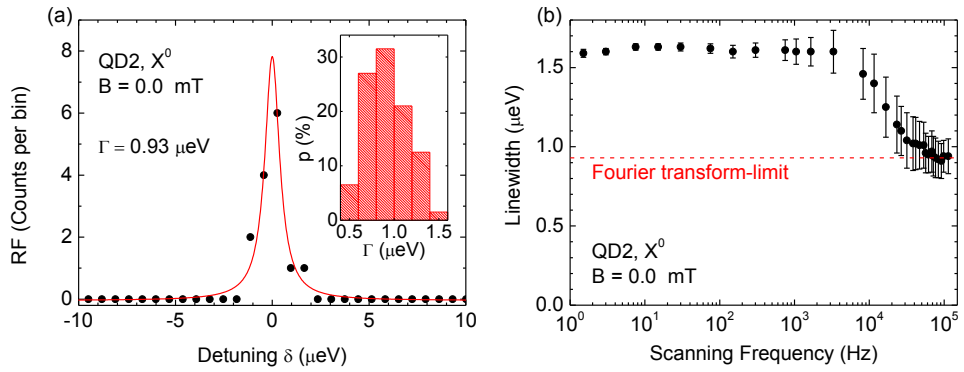
Fig. 3.4. Optical linewidth. (a) An example X^0 RF spectrum ($\Gamma = 0.93 \pm 0.10$ μeV) measured with $f_{\text{scan}} = 58$ kHz and $t_{\text{bin}} = 13$ μs. The scanning frequency is defined as $d\delta/dt/\Gamma_0$ where Γ_0 is the transform-limited linewidth. Inset: histogram of 200 linewidths recorded also with $f_{\text{scan}} = 58$ kHz. (b) RF linewidth against scanning frequency. The radiative lifetime is $\tau_r = (700 \pm 50)$ ps. Γ approaches Γ_0 for scanning frequencies above 50 kHz. For each f_{scan}, the error bar represents the standard deviation of several hundred linewidth scans.

reflects the influence of processes which are slow not just relative to the recombination rate (GHz) but also relative to our maximum experimental "speed" (100 kHz). These results are confirmed by measuring also X^{1-} with the same procedure. In this case, the linewidth decreases to 0.75 μeV at high scan rates, a lower value than for X^0, reflecting the slightly larger radiative decay time[29] for X^{1-} (see appendix B). We note that the low-frequency X^0 and X^{1-} linewidths are caused by spin noise, not by charge noise: the charge noise implies a line broadening of < 0.05 μeV, whereas the $B_{N,\text{rms}}$ values allow us to reproduce both the X^0 and X^{1-} linewidths. Using in this way the low-frequency linewidths as a noise integrator adds weight to our analysis of the noise spectra.

3.5 Charge noise and spin noise spectra

The charge noise in $N_{\text{QD}}(f)$ is the sum of a Lorentzian spectrum and a $1/f^\alpha$ component with $\alpha \sim 0.8$. The Lorentzian part is characteristic of a two-level fluctuator[30].

A single two-level fluctuator would lead to pronounced telegraph noise in the RF which we do not observe in this experiment. Instead, we postulate that the Lorentzian noise arises from fluctuations in an *ensemble* of two-level fluctuators, each with approximately the same transition rates, $0 \to 1$, $1 \to 0$. The particular fluctuators are hole localization centres at an interface 150 nm above the quantum dot, identified by the sign and magnitude of very occasional telegraph-like features (see appendix B). This assertion is supported by the fact that the Lorentzian noise disappears when the interface is
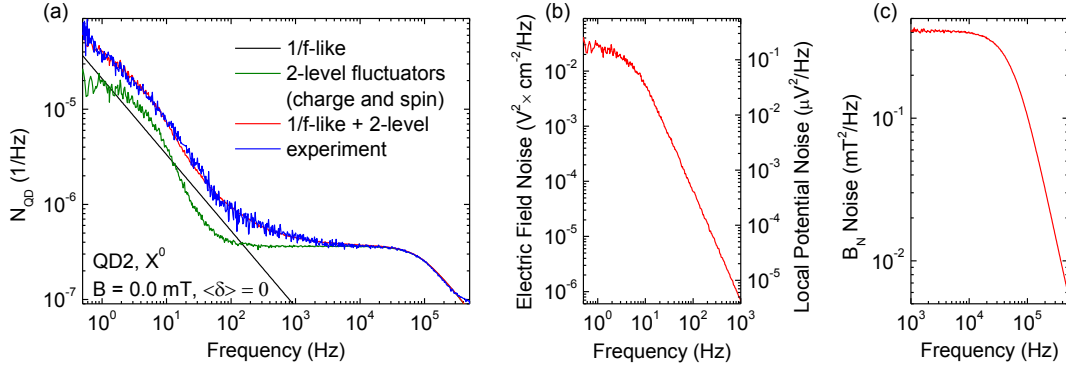
Fig. 3.5. Noise spectra of local electric and magnetic fields. (a) Experimental RF noise spectrum (blue) recorded on the neutral exciton X^0 with result of simulation (red). The simulation uses parameters $a = 0.032\ \mu eVcm/V$, $N_c = 1.0 \times 10^{10}\ cm^{-2}$, $\tau_0 = 30$ s, $\tau_1 = 0.03$ s, $p = 0.1$ % to model charge noise and $g = -0.5$, $\Delta = 17.3\ \mu eV$, $N_{eff} = 65$, $A = 90\ \mu eV$, $\tau_0 = \tau_1 = 5.5\ \mu s$ for spin noise (see appendix B). To fully describe charge noise a $1/f^\alpha$ noise component with $\alpha = 0.8$ is added. (b) Local electric field noise (left axis), local potential noise (right axis) from the two-level fluctuators, and (c) local magnetic field noise, both deduced from the simulations of the RF noise in (a).

located much further away from the quantum dots (see appendix B). We note that surplus electrons relax rapidly into the Fermi sea whereas surplus holes, minority carriers, can be trapped in the active part of the device. Electrostatic noise arises on account of fluctuations in the exact configuration of occupied (state 0) and unoccupied (state 1) localization sites in the ensemble. We simulate the noise by taking (i) a fixed array of localization centres, (ii) a fixed average hole concentration, (iii) a centre-independent capture/escape rate, and (iv) a Monte Carlo procedure (see appendix B). The $1/f$-like charge noise is quantum dot dependent with an unknown origin.

The spin noise is modelled in a similar way to the Lorentzian charge noise, by treating each nuclear spin as a fictitious two-level system (see appendix B). The simulations yield time traces $F(t)$ and $B_N(t)$. The RF signal $S(t)$ is then calculated according to the known dependence of RF on F and B_N (see appendix B), and then a simulated noise power $N_{QD}(f)$ is calculated using exactly the same routine used to process the experimental data. The complete simulation accounts for simultaneous F and B_N fluctuations; it allows us to draw precise conclusions on the charge and spin noise without assuming for instance an over-simplified dependence of RF on F, B_N; and it enables us to perform a stringent test of the specific charge noise model.

The result of the simulation is shown in Fig. 3.5(a) where very close correspondence with the measured noise spectrum has been achieved. The low frequency noise power, the charge noise, depends sensitively on the number, location and occupation probability
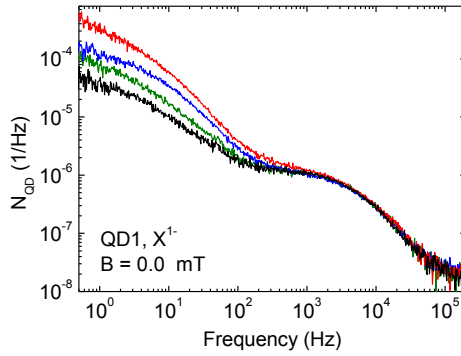
Fig. 3.6. RF noise spectra recorded on X^{1-} with $\langle\delta\rangle = 0$ under identical experimental conditions (4.2 K, $B = 0.0$ mT) in the course of the experiment. The charge noise at low frequency depends on the sample history; the spin noise at high frequency does not.

of the localization centres; the characteristic roll-off frequency on the capture/escape rates. The high frequency noise power, the spin noise, depends sensitively on $B_{N,\text{rms}}$; its associated characteristic frequency depends on the nuclear spin flip rate. The success of the simulation allows us to present the noise spectra of F and B_N individually, Fig. 3.5 (b),(c).

3.6 Sample history

It is known that the optical resonance frequency of a particular quantum dot varies slightly from cool down to cool down. Fig. 3.6(b) shows in addition that the charge noise at low temperature is dependent on the sample's history. The low frequency noise power varies by up to a factor of ten depending on the particular charge state of the sample. For this particular sample, the low noise state can be reached by temporary illumination with non-resonant laser light, followed by a wait of a few hours during which the noise at very low frequencies gradually reduces. This information is crucial in optimizing performance of the device as spin or optical qubit. The point we stress is that the noise spectrum is much more revealing about the dephasing processes than the optical frequency or optical linewidth alone.

3.7 Role of non-resonant excitation

The RF experiment involves driving the optical resonance with coherent laser light at photon energies far below the band gap of the host semiconductor and the charge

noise powers are very small. The situation changes profoundly if RF is detected in the presence of a second laser with photon energy above the band gap, non-resonant excitation. Even very small non-resonant intensities result in much increased noise. Initially, as the non-resonant power is increased, there is a rapid increase in noise at low frequencies, Fig. 3.7(a), such that the $1/f$-like noise is rapidly swamped. Even measured slowly with 0.1 s integration time per point, there are massive changes in the RF, and, as a consequence, large changes in the exact lineshape from scan to scan, Fig. 3.7(b). On increasing the non-resonant power, this low frequency noise goes away – the noise at the lowest frequencies returns almost to its original level – but noise now appears at higher frequencies, Fig. 3.7(c), in particular between 10 Hz and 10 kHz. Measured slowly, the spectrum acquires a Lorentzian-shape without scan-to-scan fluctuations, Fig. 3.7(b), but with an increased linewidth as a consequence of the extra noise at frequencies above 10 Hz. At these non-resonant powers, the photoluminescence induced by the non-resonant laser is *weaker* than the RF induced by the resonant laser. At higher non-resonant laser powers, the photoluminescence dominates over the RF and the noise increases further[31]. These results demonstrate that while non-resonant illumination can change and possibly reduce fluctuations at low-frequency, it results in a *net increase* in noise. The standard optical technique, detection of photoluminescence with non-resonant excitation, has this serious flaw, expressed quantitatively in this experiment.

3.8 Outlook

As an outlook, we comment that (i) the high frequency limit of our experiment is limited only by the photon flux which can be increased relatively simply using either a micro-cavity or photonic nanowire to enhance the photon extraction efficiency from the device. Our technique is potentially capable of mapping the noise from sub-Hz frequencies up to the GHz regime where spin noise corresponding to electron spin precession in B_N may be revealed[10]. (ii) The charge noise is measured here in a simple device and represents a baseline for the local charge noise in an ultra-pure semiconductor. The noise probe can be applied to micro- or nano-structured devices. (iii) The technique opens a new route to probing spin noise. Its dependence on external magnetic field, charge state of the quantum dot, laser excitation etc. can all be probed simply by recording time traces of the RF. (iv) The experiment demonstrates that the dephasing processes which limit the T_2^* of the quantum dot exciton are all slow with respect to radiative recombination; and that charge and spin noise reduce rapidly for increasing frequencies. These results
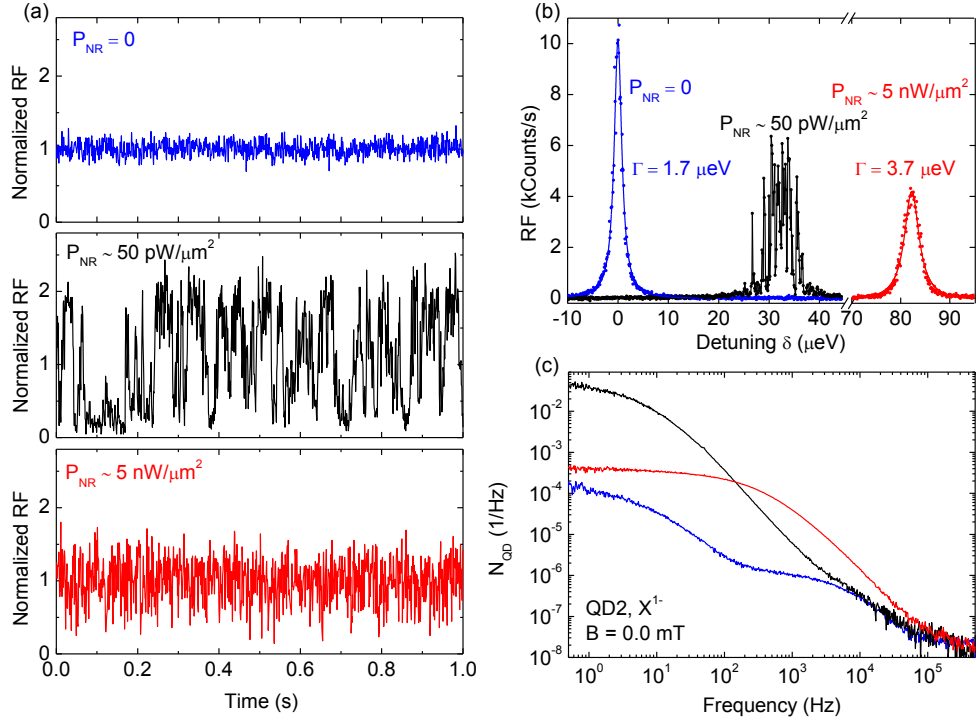
Fig. 3.7. Noise and above band gap excitation. (a) Normalized RF time traces from a single quantum dot, (b) RF spectra (0.1 s integration per point), and (c) noise spectra plotted for X^{1-} non-resonant power zero (blue), 1.3 nW (black) and 168 nW (red) focused to a spot area of $\sim 20~\mu m^2$. The non-resonant excitation induces initially considerable noise at low frequencies; larger non-resonant excitation sees the low frequency noise return close to the value observed without non-resonant excitation but considerable noise now appears above a few tens of Hz.

all point to the possibilities of achieving close to dephasing-free qubit operations by working at very high frequencies or at lower frequencies by exploiting echo-like schemes.

3.9 Methods

The InGaAs quantum dots are embedded in an ultra-clean n-i-Schottky structure with tunnel barrier 25 nm and capping layer thickness 150 nm. A single quantum dot optical resonance is driven in the linear regime with a resonant laser (1 MHz linewidth). Detuning of the quantum dot relative to the constant frequency laser is achieved by tuning the quantum dot via the dc Stark effect. Resonance fluorescence is detected, rejecting reflected laser light with a dark field technique [7,18,32]. The arrival time of each

photon is recorded over the entire measurement time T.

Post measurement, a binning time t_{bin} is selected, typically 1 μs. The number of counts in each time bin is $S(t)$, the average number of counts per bin $\langle S(t) \rangle$. The fast Fourier transform of the normalized RF signal $S(t)/\langle S(t) \rangle$ is calculated to yield a noise power spectrum, $N_{RF}(f) = |\text{FFT}[S(t)/\langle S(t) \rangle]|^2 (t_{bin})^2/T$. The quantum dot noise spectrum $N_{QD}(f)$ is determined from $N_{RF}(f)$ by subtracting the experimental noise (see appendix B). No resonances in $N_{QD}(f)$ have been discovered; thus we present $N_{QD}(f)$ after averaging at each f over a frequency range yielding equidistant data points on a logarithmic scale.

The quantum dot optical linewidth Γ is determined by applying a triangle voltage signal to the gate which induces a time-dependent detuning δ. The scan frequency is defined as $f_{scan} = d\delta/dt/\Gamma_0$ where $\Gamma_0 = \hbar/\tau_r$ with τ_r the radiative lifetime.

The resonance fluorescence depends on the detuning which in turn depends on the local electric and magnetic fields, $F(t)$ and $B_N(t)$ via a Stark shift and Zeeman effect (see appendix B). Simulations are used to calculate $F(t)$ and $B_N(t)$, adjusting parameters to give the same noise spectrum as in the experiment. The simulations consider an ensemble of independent two-level fluctuators[30], charge localization centres (charge noise) and spins (spin noise).

References

1. Loss, D. and DiVincenzo, D. P. *Phys. Rev. A* **57**, 120–126 (1998).

2. Petta, J. R., Johnson, A. C., Taylor, J. M., Laird, E. A., Yacoby, A., Lukin, M. D., Marcus, C. M., Hanson, M. P., and Gossard, A. C. *Science* **309**, 2180–2184 (2005).

3. Shields, A. J. *Nature Photon.* **1**, 215 (2007).

4. Fischer, J. and Loss, D. *Science* **324**, 1277–1278 (2009).

5. Högele, A., Seidl, S., Kroner, M., Karrai, K., Warburton, R. J., Gerardot, B. D., and Petroff, P. M. *Phys. Rev. Lett.* **93**, 217401 (2004).

6. Atatüre, M., Dreiser, J., Badolato, A., Högele, A., Karrai, K., and Imamoglu, A. *Science* **312**, 551–553 (2006).

7. Houel, J., Kuhlmann, A. V., Greuter, L., Xue, F., Poggio, M., Gerardot, B. D., Dalgarno, P. A., Badolato, A., Petroff, P. M., Ludwig, A., Reuter, D., Wieck, A. D., and Warburton, R. J. *Phys. Rev. Lett.* **108**, 107401 (2012).

8. Klotz, F., Jovanov, V., Kierig, J., Clark, E. C., Rudolph, D., Heiss, D., Bichler, M., Abstreiter, G., Brandt, M. S., and Finley, J. J. *Appl. Phys. Lett.* **96**(5), 053113 (2010).

9. Pingenot, J., Pryor, C. E., and Flatté, M. E. *Phys. Rev. B* **84**, 195403 (2011).

10. Merkulov, I. A., Efros, A. L., and Rosen, M. *Phys. Rev. B* **65**, 205309 (2002).

11. Khaetskii, A. V., Loss, D., and Glazman, L. *Phys. Rev. Lett.* **88**, 186802 (2002).

12. Greilich, A., Yakovlev, D. R., Shabaev, A., Efros, A. L., Yugova, I. A., Oulton, R., Stavarache, V., Reuter, D., Wieck, A., and Bayer, M. *Science* **313**, 341–345 (2006).

13. Xu, X., Sun, B., Berman, P. R., Steel, D. G., Bracker, A. S., Gammon, D., and Sham, L. J. *Nature Phys.* **4**, 692–695 (2008).

14. Press, D., De Greve, K., McMahon, P. L., Ladd, T. D., Friess, B., Schneider, C., Kamp, M., Höfling, S., Forchel, A., and Yamamoto, Y. *Nature Photon.* **4**, 367–370 (2010).

15. Barthel, C., Medford, J., Marcus, C. M., Hanson, M. P., and Gossard, A. C. *Phys. Rev. Lett.* **105**, 266808 (2010).

16. de Lange, G., Wang, Z. H., Ristè, D., Dobrovitski, V. V., and Hanson, R. *Science* **330**, 60–63 (2010).

17. Bluhm, H., Foletti, S., Neder, I., Rudner, M., Mahalu, D., Umansky, V., and Yacoby, A. *Nature Phys.* **7**, 109–113 (2011).

18. Matthiesen, C., Vamivakas, A. N., and Atatüre, M. *Phys. Rev. Lett.* **108**, 093602 (2012).

19. Nguyen, H. S., Sallen, G., Voisin, C., Roussignol, P., Diederichs, C., and Cassabois, G. *Appl. Phys. Lett.* **99**, 261904 (2011).

20. Urbaszek, B., Marie, X., Amand, T., Krebs, O., Voisin, P., Maletinsky, P., Högele, A., and Imamoglu, A. *Rev. Mod. Phys.* **85**, 79–133 (2013).

21. Medford, J., Cywiński, L., Barthel, C., Marcus, C. M., Hanson, M. P., and Gossard, A. C. *Phys. Rev. Lett.* **108**, 086802 (2012).

22. Reilly, D. J., Taylor, J. M., Laird, E. A., Petta, J. R., Marcus, C. M., Hanson, M. P., and Gossard, A. C. *Phys. Rev. Lett.* **101**, 236803 (2008).

23. Fink, T. and Bluhm, H. *Phys. Rev. Lett.* **110**, 010403 (2013).

24. Crooker, S. A., Brandt, J., Sandfort, C., Greilich, A., Yakovlev, D. R., Reuter, D., Wieck, A. D., and Bayer, M. *Phys. Rev. Lett.* **104**, 036601 (2010).

25. Alén, B., Bickel, F., Karrai, K., Warburton, R. J., and Petroff, P. M. *Appl. Phys. Lett.* **83**, 2235–2237 (2003).

26. Vamivakas, A. N., Zhao, Y., Fält, S., Badolato, A., Taylor, J. M., and Atatüre, M. *Phys. Rev. Lett.* **107**, 166802 (2011).

27. Coish, W. A. and Baugh, J. *Phys. Status Solidi* **246**, 2203–2215 (2009).

28. Kloeffel, C., Dalgarno, P. A., Urbaszek, B., Gerardot, B. D., Brunner, D., Petroff, P. M., Loss, D., and Warburton, R. J. *Phys. Rev. Lett.* **106**, 046802 (2011).

29. Dalgarno, P. A., Smith, J. M., McFarlane, J., Gerardot, B. D., Karrai, K., Badolato, A., Petroff, P. M., and Warburton, R. J. *Phys. Rev. B* **77**, 245311 (2008).

30. Machlup, S. *J. Appl. Phys.* **25**, 341–343 (1954).

31. Berthelot, A., Favero, I., Cassabois, G., Voisin, C., Delalande, C., Roussignol, P., Ferreira, R., and Gerard, J. M. *Nature Phys.* **2**, 759–764 (2006).

32. Yilmaz, S. T., Fallahi, P., and Imamoglu, A. *Phys. Rev. Lett.* **105**, 033601 (2010).

Chapter 4

Charge noise reduction with a dynamic feedback technique

Single quantum dots are solid-state emitters which mimic two-level atoms but with a highly enhanced spontaneous emission rate. A single quantum dot is the basis for a potentially excellent single photon source. One outstanding problem is that there is considerable noise in the emission frequency, making it very difficult to couple the quantum dot to another quantum system. We solve this problem here with a dynamic feedback technique that locks the quantum dot emission frequency to a reference. The incoherent scattering (resonance fluorescence) represents the single photon output whereas the coherent scattering (Rayleigh scattering) is used for the feedback control. The fluctuations in emission frequency are reduced to 20 MHz, just $\sim 5\%$ of the quantum dot optical linewidth, even over several hours. By eliminating the $1/f$-like noise, the relative fluctuations in quantum dot noise power are reduced to $\sim 10^{-5}$ at low frequency. Under these conditions, the antibunching dip in the resonance fluorescence is described extremely well by the two-level atom result. The technique represents a way of removing charge noise from a quantum device.

(Experiments and results presented in this chapter were obtained in close collaboration with Jonathan H. Prechtel.)

4.1 Introduction

Single photons are ideal carriers of quantum information[1–3]. A quantum state stored in one of the degrees of freedom of the photon's wave packet (polarization, phase or time-bin) can be maintained over long distances. Single photons are therefore important in quantum communication[3], for coupling remote stationary qubits[4], the basis of a quantum repeater[5], or for coupling different elements in a quantum device. Furthermore, single photons are the seed for a variety of quantum optics experiments[6,7].

Key parameters for a single photon source are fidelity of the antibunching, flux, wavelength and photon indistinguishability[8]. Remarkably, solid-state emitters are presently better able to meet these demands than atomic systems[6,7]. In particular, spontaneous emission from individual quantum dots embedded in an inorganic semiconductor is a very promising source of highly antibunched, high flux, indistinguishable photons[7,9,10]. The antibunching, particularly with resonant excitation, is very high[11]. The radiative lifetime is very short, typically just less than $1\,\mathrm{ns}$[12]. The flux is usually limited by the poor collection efficiency: most of the light is internally reflected at the GaAs-vacuum interface. However, this problem can be solved by nano-structuring the photonic modes to create a micro-cavity[13] or a photonic nanowire[14]. In the latter case, collection efficiencies of $\sim 70\%$ have been achieved. The photon indistinguishability is very high for successive photons[10]. Based on the optical linewidth, typically a factor of two above the transform limit when measured with resonant excitation[15–18], the indistinguishability is also reasonably high for photons emitted widely separated in time. Furthermore, a single quantum dot has also been developed as a spin qubit[19], facilitating an interface between stationary qubits and photons[20–22].

Unlike a real atom, the exact transition wavelength of a quantum dot is not locked to any particular wavelength and varies considerably from quantum dot to quantum dot. However, the host semiconductor can be designed so that considerable possibilities for tuning the emission wavelength exist. Electric field tuning[23,24] and strain tuning[25,26] allow the emission wavelength to be tuned over several nanometres. A major problem remains. The emission wavelength is not constant: it varies randomly over time, even in very controlled environments at low temperature. The culprit at low frequency is electrical noise in the semiconductor which shifts the emission wavelength via the Stark effect[18]. This noise has a $1/f$-like power spectrum resulting in, first, large and uncontrolled drifts at low frequencies and second, an undefined mean value. This noise, while poorly understood, is ubiquitous in semiconductors and makes it very difficult to couple an individual quantum dot to another quantum system, another quantum dot

for instance, or an ensemble of cold atoms. We present here a new scheme which solves this problem: we create a stream of single photons with a wavelength which remains constant even over several hours.

The output of our quantum device is a stream of single photons generated by resonance fluorescence (RF) from a single quantum dot. RF has considerable advantages over non-resonant excitation of photoluminescence: the linewidth is much lower[17,18] and the antibunching is much better. We lock the wavelength of the quantum device to a stable reference. We generate an error signal, a signal with large slope at its zero-crossing, by measuring the differential transmission, $\Delta T/T$, simultaneously[15,27,28]. The control variable is the voltage V_g applied to a surface gate which influences the quantum dot frequency via the Stark effect. The performance of the feedback scheme is characterized by, first, measuring a series of snap-shots of the optical resonance to assess the residual frequency jitter; and second, by carrying out a full analysis of the noise in the RF.

Our scheme goes well beyond previous attempts at single emitter stabilization in the solid-state[29,30]. The first experiment on frequency stabilization locked a non-standard quantum dot at $780\,\text{nm}$ to the atomic resonance of Rb[29]. We are not limited to any "magic" wavelengths, and in particular we can stabilize the emission wavelengths of high-quality InGaAs quantum dots which typically emit in the $900 - 1000\,\text{nm}$ range. The second advance of our scheme is a 100 times better frequency stabilization relative to ref.[29]. Here, the absolute frequency of the quantum dot emission is locked with an uncertainty of just $20\,\text{MHz}$. We observe a reduction in the noise power up to a frequency of $\sim 100\,\text{Hz}$, a bandwidth high enough to eliminate the substantial drifts at low frequency.

4.2 Feedback concept

A sketch of the experimental concept is shown in Fig. 4.1(a). A linearly-polarized resonant laser is focused onto the sample surface and drives the optical transition. The resonance fluorescence of the quantum dot is collected with a polarization-based dark field technique[17,20,31], described in detail in chapter 1. Simultaneously, the optical resonance is detected in transmission by superimposing a sub-linewidth modulation to the gate. The transmission signal arises from an interference of quantum dot scattering with the driving laser[28]. The incoherent part, i.e. the resonance fluorescence, averages to zero in transmission; what is detected instead is the coherent scattering, i.e. the Rayleigh scattering. In this way, the experiment utilizes both incoherent and coherent
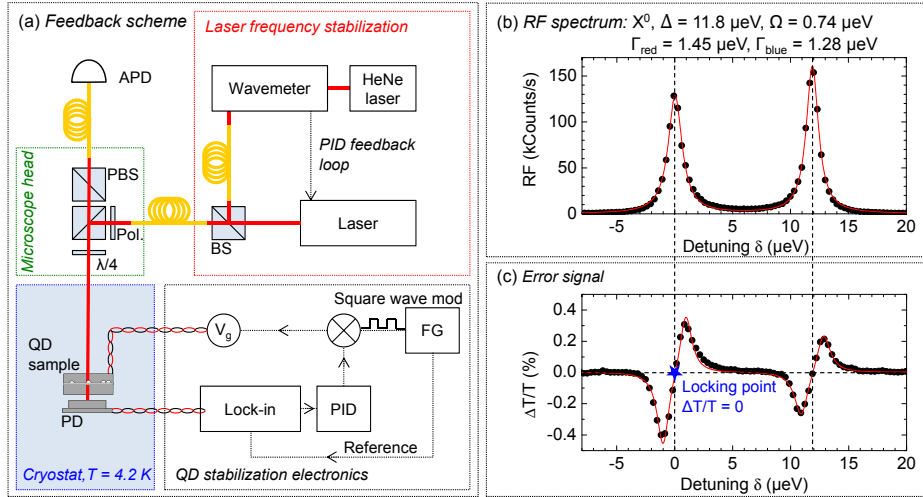
Fig. 4.1. (a) Schematic view of the experiment. The narrowband laser is stabilized to a fixed frequency by a wavemeter which in turn is stabilized to a HeNe laser. Laser light is guided through optical fibres (yellow) and microscope optics before it is focused onto the sample, driving the X^0 transition resonantly (BS = beam-splitter, PBS = polarizing BS, Pol. = linear polarizer). Two simultaneous measurements of X^0 scattering are performed: resonance fluorescence (RF), detected with an avalanche photodiode (APD) and absorption with a photodiode (PD) underneath the sample. The dynamic stabilization is realized with an active PID feedback loop which corrects for fluctuations in the transition energy using the gate voltage V_g and the square wave modulation of a function generator (FG). (b) RF signal of the fine-structure split X^0 emission of a single quantum dot at wavelength 936.5 nm, a power corresponding to a Rabi energy Ω of 0.74 μeV and a temperature of 4.2 K. A detuning is achieved by sweeping the gate voltage. The solid red line is a Lorentzian fit to the data with linewidth $\Gamma = 1.28$ μeV (309 MHz) and $\Gamma = 1.45$ μeV (350 MHz) and with a fine structure splitting $\Delta = 11.6$ μeV. (c) The differential transmission ($\Delta T/T$) signal on the same quantum dot with integration time 100 ms per point. The red curve is a fit to the derivative of the two Lorentzians. The signal around the zero crossing point ($\Delta T/T = 0$) is used to generate an error signal for the feedback scheme.

parts of the scattered light, for the single photon output and control, respectively. With a small modulation, the transmission signal has a large slope with zero crossing at zero detuning and is therefore ideal for the generation of an error signal. $\Delta T/T$, the error signal, is recorded with a lock-in amplifier to reject noise and the lock-in output is fed into a classical feedback scheme. The feedback output is, like the modulation, applied to the gate electrode of the device. The set-point of the control loop is the zero crossing with the goal of locking the peak of the quantum dot RF spectrum to the laser. The laser itself is locked to a HeNe laser reference.

4.3 Feedback scheme

4.3.1 The quantum dot sample

The self-assembled InGaAs quantum dots, grown by molecular beam epitaxy, are integrated into a semiconductor charge-tunable heterostructure[32]. The quantum dots are located 25 nm above a heavily n-doped GaAs back contact ($n = 1.7 \times 10^{18}$ cm^{-3}). The intermediate layer, undoped GaAs, acts as a tunneling barrier. A 150 nm GaAs layer caps the quantum dots and an AlAs/GaAs superlattice (68 periods of AlAs/GaAs 3 nm/1 nm) completes the heterostructure. A Ti/Au (5 nm/10 nm) Schottky gate is deposited on the sample surface; Ohmic contacts are prepared to the back contact. Bias V_g is applied between the Schottky gate and the back contact. The sample is placed in a liquid helium bath cryostat at 4.2 K with a residual magnetic field of 10 mT.

4.3.2 Single quantum dot laser spectroscopy

The single quantum dot spectroscopy is performed with a confocal microscope. The continuous wave laser has a short-term linewidth of 1 MHz. Long-term wavelength stability of $\sim$ 2 MHz is achieved by locking the laser to a high resolution wavemeter, itself locked to a high quality HeNe laser. The size of the focal spot and the collection efficiency of the single quantum dot RF are both enhanced with a half-sphere zirconia solid immersion lens positioned on top of the Schottky gate. Fig. 4.1(b) shows a RF signal from the neutral exciton transition, $|0\rangle \leftrightarrow |X^0\rangle$, where $|X^0\rangle$ represents an electron-hole complex and $|0\rangle$ the crystal ground state. The RF is detected with a silicon avalanche photodiode (APD) in single photon counting mode and the detuning of the quantum dot resonances relative to the constant frequency laser is achieved in this case with the Stark shift induced by the bias V_g. The X^0 exhibits a fine structure splitting of 11.6 μeV, the two lines having linewidths $\Gamma = 1.45$, 1.28μeV close to the transform limit of $\Gamma_0 = \hbar/\tau_r = 0.93 \mu$eV (220 MHz) where τ_r is the radiative lifetime of the exciton transition ($\tau_r = 0.71 \pm 0.01$ ns here).

4.3.3 Feedback loop

A sub-linewidth square-wave modulation at 527 Hz is applied to the Schottky gate. This broadens both X^0 transitions slightly, here the "red" transition from $\Gamma = 1.45$ to $\Gamma = 2.58 \mu$eV. The transmitted light is detected with an in situ photodiode connected to a room temperature current-voltage preamplifier. Lock-in detection of the $\Delta T/T$ signal is shown in Fig. 4.1(c). With the sub-linewidth modulation, the $\Delta T/T$ resonance is

proportional to the derivative of the RF spectrum[27]. There are two points which cross with high slope through zero, one for each X^0 transition. Both crossing points enable a feedback scheme: $\Delta T/T$ provides the error signal, V_g the control parameter. For instance, if the transition energy increases due to electric fluctuations in the sample, $\Delta T/T$ moves away from zero. Once this is detected, a modified V_g is applied to the gate to bring the resonance back to the set point. For the feedback circuit we use a PID loop. The proportional factor $P = 0.1$ is chosen with respect to the slope of the error signal, while the integral $I = 0.06$ and the derivative constant $D = 6 \times 10^{-5}$ were obtained by tuning methods. The signal:noise ratio in the $\Delta T/T$ circuit allows us to run the feedback scheme with a bandwidth up to $\sim 50\,\mathrm{Hz}$ matching the frequency range of the device's charge fluctuations. The fluctuations of the nuclear spins exceed the bandwidth of the feedback[18]. The "red" X^0 transition was used for the subsequent feedback experiments because it has a higher $\Delta T/T$ contrast than the "blue" X^0 transition.

The noise in the device consists of charge noise and spin noise[18]. The charge noise power spectrum consists of $1/f$-like noise and Lorentzian noise, the latter with a characteristic frequency of $\sim 10\,\mathrm{Hz}$[18]. This means that the feedback bandwidth is sufficient to eliminate the low frequency drift and most of the Lorentzian noise. The spin noise power spectrum has a smaller amplitude but higher characteristic frequency, $\sim 10\,\mathrm{kHz}$[18], exceeding the bandwidth of the feedback.

4.4 Feedback performance

4.4.1 Residual frequency jitter

The performance of the single quantum dot frequency stabilization is put to the test in a stroboscopic experiment. The X^0 transition energy is mapped with a second laser (linewidth also $1\,\mathrm{MHz}$). The first laser stabilizes the transition with the feedback scheme at a power corresponding to a Rabi energy Ω of $0.74\,\mu\mathrm{eV}$. A second laser of identical power is tuned with triangular function back and forth through the same transition with a rate of $8.0\,\mu\mathrm{eV/s}$. The sum of the power of both lasers was selected to lie below the power at which power broadening becomes significant. The RF spectrum is fitted to a constant (to describe RF from the first laser) plus Lorentzian function (to describe RF from the second laser) in order to determine the center position of the resonance. In this way, a "snap-shot" of the resonance position is recorded every $5\,\mathrm{s}$ with "exposure time" $100\,\mathrm{ms}$ for a total of $1,000\,\mathrm{s}$. The distribution of the peak position can be seen in the histogram in Fig. 4.2. In Fig. 4.2(a) and (b), the scanning laser results in an asymmetry: the resonance frequency is more likely to lie at positive detunings on
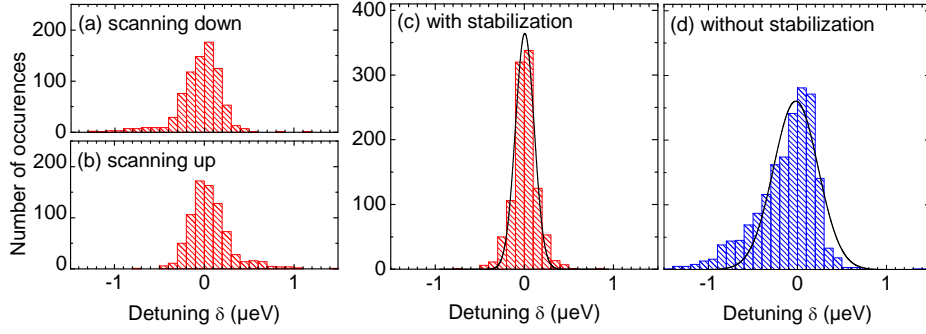
Fig. 4.2. Histogram of the RF peak position with (a, b, c) and without (d) the stabilization scheme. A triangle V_g is applied. The scanning rate of the laser is $8.0\,\mu\text{eV/s}$ with period $10\,\text{s}$. Histograms of the RF peak position for up-sweeps (a) and down-sweeps (b) recorded with feedback. (c) shows the histogram with feedback, negative detunings from the up-sweeps, positive detunings from the down-sweeps. A histogram without feedback is shown in (d). The standard deviation σ is reduced from (d) $0.250\,\mu\text{eV}$ ($61\,\text{MHz}$) without active stabilization to (c) $0.089\,\mu\text{eV}$ ($22\,\text{MHz}$) with active stabilization.

sweeping from negative to positive detunings, and vice versa. This is probably related to the so-called "dragging" effect[33] which is very pronounced on this quantum dot at high magnetic fields (above $0.1\,\text{T}$)[34]: the nuclear spins polarize in such a way as to maintain the resonance with the laser over large detunings. In other words, it is likely that the asymmetries in Fig. 4.2(a) and (b) are first hints of dragging. The histogram in Fig. 4.2(c) is a combination of the data sets of (a) and (b) which are influenced least by dragging (up-sweeps at negative detuning, down-sweeps at positive detuning). Without the stabilizing loop, the long term drift, i.e. the $1/f$-like noise, results in a broader distribution, Fig. 4.2(d). This drift also leads to the asymmetry in Fig. 4.2(d), reflecting a trend to the red in this particular case. The fluctuations in resonance positions are quantified with the standard deviation σ_E of the peak positions. Without stabilization Fig. 4.2(d), $\sigma_E^{\text{OFF}} = 0.250\,\mu\text{eV}$ ($61\,\text{MHz}$). With active stabilization, $\sigma = 0.102\,\mu\text{eV}$ ($25\,\text{MHz}$). This value is small enough to be influenced by shot noise in each data point which results in an energy uncertainty on fitting each spectrum to a Lorentzian. The shot noise results in an energy jitter of $\sigma_{E,\text{shot}} = 0.049\,\mu\text{eV}$, giving $\sigma_E^{\text{ON}} = \sqrt{\sigma^2 - \sigma_{E,\text{shot}}^2} = 0.089\,\mu\text{eV}$ ($22\,\text{MHz}$), 36% of σ_E^{OFF}. The measurement of σ_E represents a measurement of the noise in a bandwidth from $\sim 1\,\text{mHz}$ to $\sim 3.1\,\text{Hz}$. (Noise at higher frequencies is reflected in the linewidth Γ.) The ratio $\sigma_E^{\text{OFF}} : \sigma_E^{\text{ON}}$ would increase if lower frequencies were included on account of the $1/f$-like noise: σ_E^{ON} would remain the same but σ_E^{OFF} would increase.

The ultimate operation capability of the stabilization system is limited by the random noise in the output of the PID electronics. In Fig. 4.1(c) the noise in the $\Delta T/T$ signal is

$\sigma_{\Delta T/T} = 1.45 \times 10^{-4}$. In the ideal case, this determines the energy jitter of the quantum dot resonance position[35],

$$\sigma_{E,\min} = \frac{d\delta}{d\Delta T}\sigma_{\Delta T/T} \simeq 0.013 \ \mu\text{eV} \ (3 \ \text{MHz}) \tag{4.1}$$

where δ is the detuning. This limit, ~ 100 times smaller than the linewidth, illustrates the power of this technique. We have not yet reached this limit in practice. Nevertheless, stabilization with a residual jitter down to just $\sigma_E/h = 22\,\text{MHz}$ is achieved.

4.4.2 Spectral analysis of the noise

The frequency locking feedback scheme was also tested regarding its long term behaviour and bandwidth. The RF signal was recorded over several hours, Fig. 4.3(a), without (blue) and with (red) the stabilizing loop. The measurements are accomplished by tuning the X^0 of the quantum dot via the Stark effect into resonance with the excitation laser ($\delta = 0\,\mu\text{eV}$) and then recording the arrival time of each single photon detected by the APD over the duration of the entire experiment T. Post-experiment, the data are analysed by setting a binning time, $t_{\text{bin}} = 100\,\text{ms}$ in this case. For a fixed V_g, the RF counts show large fluctuations up to a factor of 2 (blue curve). The origin are slow electrical fluctuations in the sample which cause the transition to drift out of resonance with the laser. With the feedback on, these fluctuations disappear and the RF remains at a constant level (red curve). The fluctuations in the red curve arise almost entirely from shot noise in the detector, Fig. 4.3(b). The average RF signal is a little smaller with feedback because the applied modulation broadens slightly the resonance.

Insight into the bandwidth of the stabilization mechanism is revealed by a fast Fourier transform (FFT) of the time trace. Although the shot noise dominates, the shot noise can be independently measured with a small amount of reflected laser light as a source, allowing us to determine the noise coming solely from the quantum dot. The FFT of the normalized RF signal $S(t)/\langle S(t)\rangle$ provides a noise spectrum[18]:

$$N_{\text{RF}}(f) = |\text{FFT}[S(t)/\langle S(t)\rangle]|^2 (t_{\text{bin}})^2/T. \tag{4.2}$$

For $N_{\text{RF}}(f)$, $t_{\text{bin}} = 1\ \mu\text{s}$ and $T = 2$ hours. The noise spectrum of the quantum dot $N_{\text{QD}}(f)$ is obtained by correcting the RF noise by the noise of the experiment $N_{\text{exp}}(f)$ $[N_{\text{QD}}(f) = N_{\text{RF}}(f) - N_{\text{exp}}(f)]$. $N_{\text{QD}}(f)$ corresponding to the time traces of Fig. 4.3(a) are shown in Fig. 4.3(c). Without feedback, $N_{\text{QD}}(f)$ has a $1/f$-like dependence on f as a consequence of charge noise in the device. With feedback, $N_{\text{QD}}(f)$ is reduced by up to
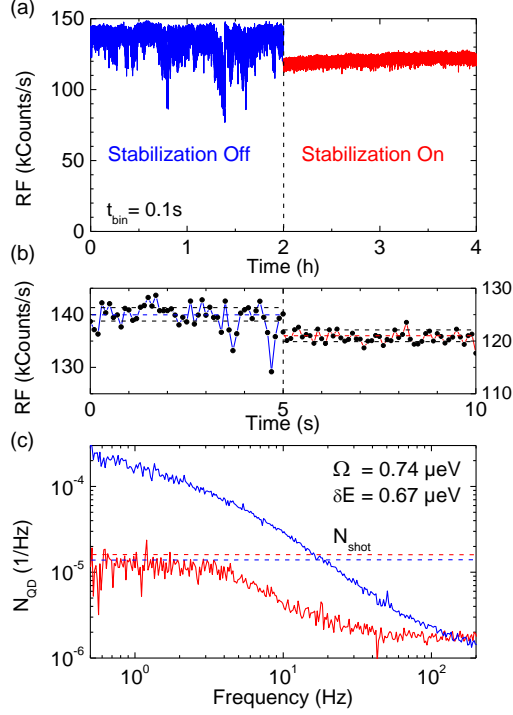
Fig. 4.3. (a) Time trace of the resonance fluorescence (RF) of a single quantum dot (the one from Fig. 4.1) with $\delta = 0\,\mu\text{eV}$ recorded over several hours. The binning time was $t_{\text{bin}} = 100\,\text{ms}$. The time trace is plotted with (red) and without (blue) the dynamic stabilization scheme. (b) $5\,\text{s}$ excerpts of the unstabilized (blue) and stabilized (red) time traces with the dashed lines representing the shot noise limits. (c) Noise spectra of the normalized RF signal, $S(t)/\langle S(t)\rangle$, corresponding to the time traces of (a) after correction for external noise sources. The shot noise in the experiment is shown with the dashed lines.

a factor of 20 at the lowest frequencies, and is constant: the $1/f$-like noise is eliminated. The two curves meet at $f \simeq 130\,\text{Hz}$ once the bandwidth of the PID circuit has been exceeded. At higher frequency the noise spectrum is dominated by spin noise[18].

The two experiments, intensity noise and energy jitter measurements, can be linked to add weight to our analysis. Specifically, we forge a relationship between the RF noise under feedback and the jitter in the energy detuning, σ_E, connecting a measurement of noise in a time trace to a separate measurement of a fluctuation in an energy detuning. The detuning jitter is much less than the linewidth such that the change in the RF signal (ΔRF) is related quadratically to the detuning for fluctuations around $\delta = 0$. The variance of the RF noise, σ_{RF}^2, is related to an integral of the noise curve, $\sigma_{\text{RF}}^2 = \int N_{\text{QD}}(f)df$ [36]. Integrating up to frequency Δf in the regime where $N_{\text{QD}}(f)$ is

approximately constant,

$$\sigma_E^{\text{ON}} = \frac{\Gamma}{2} \left(\frac{N_{\text{QD}}(0)\Delta f}{3} \right)^{\frac{1}{4}}. \tag{4.3}$$

With $\Delta f = 3.1$ Hz, $N_{\text{QD}}(0) = 1.0 \times 10^{-5}$, $\Gamma = 2.58$ μeV this predicts $\sigma_E^{\text{ON}} = 0.073$ μeV, in excellent agreement with the measurement from the stroboscopic experiment (0.089 μeV).

4.4.3 Single photon performance

An intensity correlation measurement $g^{(2)}(t)$ was performed with a Hanbury Brown-Twiss interferometer. Low noise $g^{(2)}(t)$ can only be determined at these count rates (50 kHz per APD) by integrating over several hours and the feedback is therefore important to ensure that the detuning of the quantum dot with respect to the laser remains constant. $g^{(2)}(t)$ is shown in Fig. 4.4 from X^0 of the same quantum dot with zero detuning. $g^{(2)}(t)$ falls to 10% at $t = 0$. This does not reflect $g^{(2)}(0)$ of the quantum dot but rather the timing jitter of the detectors which is comparable to the radiative lifetime. We attempt to describe $g^{(2)}(t)$ with a convolution of $g^{(2)}(t)$ for an ideal two-level atom, $g_{\text{atom}}^{(2)}(t)$, and the response of the detectors $G(t)$:

$$g^{(2)}(t) = g_{\text{atom}}^{(2)}(t) \otimes G(t). \tag{4.4}$$

The detector response is a Gaussian function,

$$G(t) = \frac{1}{\sqrt{2\pi}\sigma_D} \exp\left(-\frac{t^2}{2\sigma_D^2} \right). \tag{4.5}$$

$g_{\text{atom}}^{(2)}(t)$ of a 2-level system with resonant excitation is[37],

$$g_{\text{atom}}^{(2)}(t) = 1 - \left[\cos(\lambda t) + \frac{3}{4\tau_r}\lambda \sin(\lambda t) \right] \exp\left(-\frac{3t}{4\tau_r} \right) \tag{4.6}$$

with $\lambda = (\Omega^2 - (1/4\tau_r)^2)^{1/2}$[37]. The temporal jitter of the detector $\tau_D = 0.40$ ns ns is measured independently. Ω and τ_r are known from other experiments to within $10 - 20\%$ and are allowed to vary in these windows by a fit routine. The convolution provides an excellent description of the measured $g^{(2)}(t)$ with $\Omega = (0.99 \pm 0.1)$ μeV and $\tau_r = (0.78 \pm 0.05)$ ns. In particular, with low systematic error we can set an upper bound to the quantum dot $g^{(2)}(0)$ of 1-2%.
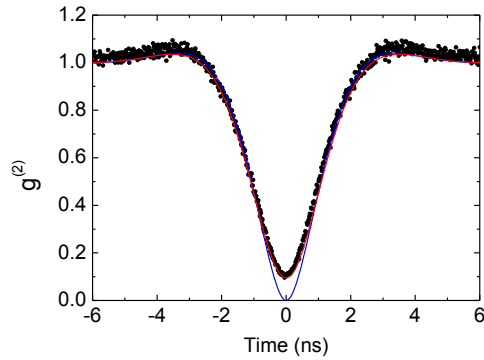
Fig. 4.4. Second-order correlation $g^2(t)$ for the stabilized RF from the X^0 (black points). The red curve shows a convolution of the two-level atom result with a Gaussian distribution which describes the timing jitter of the detectors. The blue curve shows the two-level atom response alone.

4.5 Conclusion and Outlook

In conclusion, we have developed a dynamic method of locking the optical resonance of a single quantum dot to a stabilized laser in order to produce a stream of frequency-stabilized single photons via resonance fluorescence. Generally speaking, the scheme represents a way to reduce the local charge noise in a semiconductor.

Now that the basic principle is established, there are options for improving the feedback scheme. First, the remaining jitter in the quantum dot resonance position can be reduced by reducing the noise in the transmission detection. Presently, we are far from the limit defined by the shot noise in the detector current. With lower noise, the feedback bandwidth can also be increased. The tantalizing prospect is to create transform-limited linewidths routinely with high bandwidth feedback. A bandwidth of about 50 kHz is required[18]. Secondly, the modulation required here to generate the error signal could be eliminated in a number of ways. For instance, a dispersive lineshape can arise naturally in reflectivity via weak coupling to a cavity[38]; or the Faraday effect in a small magnetic field[39] could be used.

References

1. Bennett, C. H. and Brassard, G. In *Proceedings of IEEE International Conference on Computers, Systems and Signal Processing*, (1984).

2. Ekert, A. K. *Phys. Rev. Lett.* **67**, 661–663 (1991).

3. Gisin, N., Ribordy, G., Tittel, W., and Zbinden, H. *Rev. Mod. Phys.* **74**, 145–195 (2002).

4. Bernien, H., Hensen, B., Pfaff, W., Koolstra, G., Blok, M. S., Robledo, L., Taminiau, T. H., Markham, M., Twitchen, D. J., Childress, L., and Hanson, R. *Nature* **497**, 86–90 (2013).

5. Sangouard, N., Simon, C., de Riedmatten, H., and Gisin, N. *Rev. Mod. Phys.* **83**, 33–80 (2011).

6. Buckley, S., Rivoire, K., and Vučković, J. *Rep. Prog. Phys.* **75**(12), 126503 (2012).

7. Shields, A. J. *Nature Photon.* **1**, 215–223 (2007).

8. Lounis, B. and Orrit, M. *Rep. Prog. Phys.* **68**, 1129–1179 (2005).

9. Michler, P., Kiraz, A., Becher, C., Schoenfeld, W. V., Petroff, P. M., Zhang, L. D., Hu, E., and Imamoglu, A. *Science* **290**, 2282 (2000).

10. Santori, C., Fattal, D., Vuckovic, J., Solomon, G. S., and Yamamoto, Y. *Nature* **419**, 594–597 (2002).

11. Muller, A., Flagg, E. B., Bianucci, P., Wang, X. Y., Deppe, D. G., Ma, W., Zhang, J., Salamo, G. J., Xiao, M., and Shih, C. K. *Phys. Rev. Lett.* **99**, 187402 (2007).

12. Dalgarno, P. A., Smith, J. M., McFarlane, J., Gerardot, B. D., Karrai, K., Badolato, A., Petroff, P. M., and Warburton, R. J. *Phys. Rev. B* **77**, 245311 (2008).

13. Vahala, K. J. *Nature* **424**, 839–846 (2003).

14. Claudon, J., Bleuse, J., Malik, N. S., Bazin, M., Jaffrennou, P., Gregersen, N., Sauvan, C., Lalanne, P., and Gerard, J.-M. *Nature Photon.* **4**, 174–177 (2010).

15. Högele, A., Seidl, S., Kroner, M., Karrai, K., Warburton, R. J., Gerardot, B. D., and Petroff, P. M. *Phys. Rev. Lett.* **93**, 217401 (2004).

16. Atatüre, M., Dreiser, J., Badolato, A., Hogele, A., Karrai, K., and Imamoglu, A. *Science* **312**, 551–553 (2006).

17. Houel, J., Kuhlmann, A. V., Greuter, L., Xue, F., Poggio, M., Gerardot, B. D., Dalgarno, P. A., Badolato, A., Petroff, P. M., Ludwig, A., Reuter, D., Wieck, A. D., and Warburton, R. J. *Phys. Rev. Lett.* **108**, 107401 (2012).

18. Kuhlmann, A. V., Houel, J., Ludwig, A., Greuter, L., Reuter, D., Wieck, A. D., Poggio, M., and Warburton, R. J. *Nature Phys.* **9**, 570–575 (2013).

19. Warburton, R. J. *Nature Mater.* **12**, 483 – 493 (2013).

20. Yilmaz, S. T., Fallahi, P., and Imamoglu, A. *Phys. Rev. Lett.* **105**, 033601 (2010).

21. De Greve, K., Yu, L., McMahon, P. L., Pelc, J. S., Natarajan, C. M., Kim, N. Y., Abe, E., Maier, S., Schneider, C., Kamp, M., Hoefling, S., Hadfield, R. H., Forchel, A., Fejer, M. M., and Yamamoto, Y. *Nature* **491**, 421 (2012).

22. Gao, W. B., Fallahi, P., Togan, E., Miguel-Sanchez, J., and Imamoglu, A. *Nature* **491**, 426 (2012).

23. Warburton, R. J., Schulhauser, C., Haft, D., Schäflein, C., Karrai, K., Garcia, J. M., Schoenfeld, W., and Petroff, P. M. *Phys. Rev. B* **65**, 113303 (2002).

24. Bennett, A. J., Pooley, M. A., Stevenson, R. M., Ward, M. B., Patel, R. B., de la Giroday, A. B., Skoeld, N., Farrer, I., Nicoll, C. A., Ritchie, D. A., and Shields, A. J. *Nature Phys.* **6**, 947–950 (2010).

25. Seidl, S., Kroner, M., Högele, A., Karrai, K., Warburton, R. J., Badolato, A., and Petroff, P. M. *Appl. Phys. Lett.* **88**, 203113 (2006).

26. Joens, K. D., Hafenbrak, R., Singh, R., Ding, F., Plumhof, J. D., Rastelli, A., Schmidt, O. G., Bester, G., and Michler, P. *Phys. Rev. Lett.* **107**, 217402 (2011).

27. Alén, B., Bickel, F., Karrai, K., Warburton, R. J., and Petroff, P. M. *Appl. Phys. Lett.* **83**, 2235–2237 (2003).

28. Karrai, K. and Warburton, R. J. *Superlattice Microst.* **33**, 311–337 (2004).

29. Akopian, N., Trotta, R., Zallo, E., Kumar, S., Atkinson, P., Rastelli, A., Schmidt, O. G., and Zwiller, V. *arXiv:1302.2005* (2013).

30. Acosta, V. M., Santori, C., Faraon, A., Huang, Z., Fu, K.-M. C., Stacey, A., Simpson, D. A., Ganesan, K., Tomljenovic-Hanic, S., Greentree, A. D., Prawer, S., and Beausoleil, R. G. *Phys. Rev. Lett.* **108**, 206401 (2012).

31. Matthiesen, C., Vamivakas, A. N., and Atatüre, M. *Phys. Rev. Lett.* **108**, 093602 (2012).

32. Warburton, R. J., Schäflein, C., Haft, D., Bickel, F., Lorke, A., Karrai, K., Garcia, J. M., Schoenfeld, W., and Petroff, P. M. *Nature* **405**, 926–929 (2000).

33. Latta, C., Högele, A., Zhao, Y., Vamivakas, A. N., Maletinsky, P., Kroner, M., Dreiser, J., Carusotto, I., Badolato, A., Schuh, D., Wegscheider, W., Atatüre, M., and Imamoglu, A. *Nature Phys.* **5**, 758–763 (2009).

34. Kuhlmann, A. V., Houel, J., Brunner, D., Ludwig, A., Reuter, D., Wieck, A. D., and Warburton, R. J. *Rev. Sci. Instrum.* **84**, 073905 (2013).

35. Nagourney, W. *Quantum Electronics for Atomic Physics.* Oxford University Press, (2010).

36. Kogan, S. *Electronic noise and fluctuations in solids.* Cambridge University Press, London, (1996).

37. Loudon, R. *The Quantum Theory of Light.* Oxford University Press, (2010).

38. Alén, B., Högele, A., Kroner, M., Seidl, S., Karrai, K., Warburton, R. J., Badolato, A., Medeiros-Ribeiro, G., and Petroff, P. M. *Appl. Phys. Lett,* **89**, 123124 (2006).

39. Atatüre, M., Dreiser, J., Badolato, A., and Imamoglu, A. *Nature Phys.* **3**, 101–105 (2007).

Chapter 5

Linewidth of single photons from a single quantum dot

A semiconductor quantum dot mimics a two-level atom. Performance as a single photon source is limited by decoherence and dephasing of the optical transition. Even with high quality material at low temperature, the optical linewidths are a factor of two larger than the transform limit. It is shown here that the inhomogeneous contribution to the linewidth is caused by nuclear spin noise. This conclusion applies to both neutral and charged excitons. For the neutral exciton, we demonstrate an increase in the spin noise with increasing resonant laser power. Conversely for the charged exciton, we demonstrate a significant decrease in the spin noise with resonant laser power even without an external magnetic field. This noise reduction is exploited to demonstrate transform-limited optical linewidths even when the measurement is performed very slowly.

5.1 Introduction

A single quantum dot is a robust, fast, bright and narrow-linewidth emitter of single photons, features not shared by any other emitter[1-3]. These characteristics are attractive for applications in quantum communication. However, future developments place stringent demands on the quality of the photons. For instance, entangling remote spins via two-photon interference, the concept underpinning a quantum repeater, requires a stream of indistinguishable photons. This can be achieved in a semiconductor only by understanding noise and circumventing its deleterious consequences.

A single quantum dot mimics a two-level atom and single photons are generated either by spontaneous emission from the upper level[1-3] or by coherent scattering of a resonant laser[4-6]. The radiative lifetime is typically $\tau_R = 800$ ps[7]. There is evidence that on this timescale, there is negligible pure upper level decoherence provided the quantum dot is at low temperature[4-6,8]. At low Rabi couplings but higher temperatures (above ~ 20 K)[9,10], equivalently at low temperature but at high Rabi couplings[11,12], phonons dephase the upper level. Provided then that $T \sim 4$ K and Rabi coupling $\Omega \sim \Gamma_0$ (Ω is the optical Rabi coupling and $\Gamma_0 = \hbar/\tau_R$) close-to-ideal performance is achieved on small time-scales[2]. The remaining issue concerns the wandering of the center frequency over long times[13,14]. One way to probe this is with the optical linewidth. Measured on second timescales, the linewidth Γ is typically about a factor of two larger than the transform limit Γ_0[13-15], an effect which reduces the distinguishability of single photons generated far apart in the time domain.

There are two obvious culprits for the optical linewidth, charge noise and spin noise. Charge noise arises from fluctuations in the electrical environment of the quantum dot and results in a fluctuating electric field. Spin noise arises from fluctuations in the nuclear spin ensemble and results in a fluctuating magnetic field (the Overhauser field). A diagnostic tool is to add a single electron to the quantum dot. The optical response to charge noise is largely unchanged – the Stark shifts of the neutral exciton X^0 and the charged exciton X^{1-} are similar[16] – but the response to spin noise is different[17]. The un-paired electron spin in the X^{1-} ground-state splits via the Zeeman effect in the Overhauser field, Fig. 5.1. Conversely, the X^0 state is already split at zero magnetic field $B = 0$ by electron-hole exchange (the "fine structure"[9], Fig. 5.1) such that the X^0 is "shielded" from the nuclear noise by the hole: it is much less sensitive to spin noise than the X^{1-}. In most laser spectroscopy experiments, the linewidths Γ for X^0 and X^{1-} are very similar[13,14] leading naturally to the conclusion that charge noise is responsible for the optical linewidth. We question this conclusion here. In fact, we
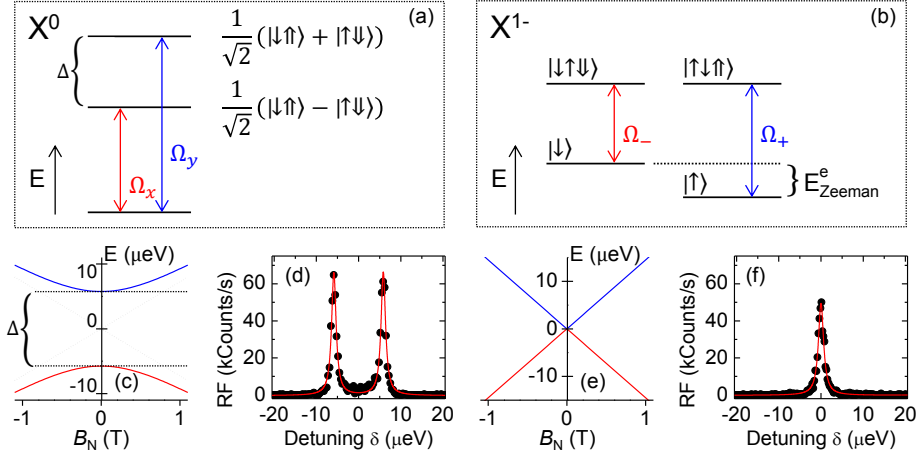
Fig. 5.1. (a) Energy levels of quantum dot neutral exciton X^0 at zero magnetic field, $B = 0$, showing fine structure splitting Δ. (b) Energy levels of charged exciton X^{1-} in an Overhauser field B_N. (c), (e) X^0, X^{1-} energy levels versus B_N with $\Delta = 11.5$ μeV and electron g-factor $g = -0.5$. (d), (f) X^0, X^{1-} resonance fluorescence spectra at 4.2 K, $B = 0.0$ mT with 100 ms integration time per point. The solid lines are Lorentzian fits to the data. The linewidths are $\Gamma^{X^0} = 1.29$ μeV, $\Gamma^{X^{1-}} = 1.49$ μeV; the Rabi energies $\Omega/\Gamma_0 = 0.5$ (X^0), 0.4 (X^{1-}); and transform limits $\Gamma_0^{X^0} = 0.92 \pm 0.10$ μeV, $\Gamma_0^{X^{1-}} = 0.75 \pm 0.10$ μeV.

present compelling evidence that the similar X^0 and X^{1-} linewidths are coincidental. We show instead that spin noise is responsible for the optical linewidths. For the neutral exciton, the nuclear spin noise increases massively with resonant laser excitation whereas for the charged exciton, laser excitation suppresses the nuclear spin noise. This nuclear spin noise suppression is effective even without an applied magnetic field. This new understanding allow us to demonstrate close-to-transform limited optical linewidths, $\Gamma = \Gamma_0$, even when measured on second time-scales.

The key physics which emerges is that the single quantum dot optical linewidths are determined in the best case (low T on high quality material with weak resonant excitation) by nuclear spin noise. It is known that the quantum dot nuclear spins dominate electron spin dephasing[18–22]. Nuclear spins therefore play a central role in dephasing qubits in quantum dots.

5.2 Methods

The quantum dots are self-assembled using InGaAs in high purity GaAs and are embedded between a back contact and a surface gate (see Appendix C))[14,17]. The voltage V_g applied to the gate determines the electron occupation via Coulomb blockade[23].

We drive the optical resonance of a single quantum dot at low temperature, 4 K, with a linearly-polarized, 1 MHz linewidth, continuous wave laser, detecting the resonance fluorescence (RF) with a single photon detector [17,24]. The linewidth is determined by sweeping the laser frequency through the resonance, integrating the counts, typically 100 ms per point. The quantum dot noise is investigated by tuning the laser frequency to the RF maximum, and determining a noise power spectrum $N_{QD}(f)$ with a Fourier transform of the time trace [17]. From the known relationships between RF signal, Rabi coupling Ω, electric field F and the Overhauser field B_N, we can deduce the variances F_{rms} and $B_{N,rms}$ from the RF noise spectrum (see Appendix C) [17]. In a two-laser experiment, a "pump" laser with a relatively high Rabi coupling Ω_2 has a constant detuning δ_2; a "probe" laser with smaller Rabi coupling Ω_1 is tuned (detuning δ_1) through the quantum dot resonance to measure a linewidth. Ω_1 is modulated at 150 Hz; the RF signal is converted into an analogue signal and a lock-in amplifier measures the signal at the modulation frequency.

5.3 Results and Discussion

RF spectra on the neutral, X^0, and charged, X^{1-}, exciton transitions are shown in Fig. 5.1 at $\Omega/\Gamma_0 = 0.5$ (X^0), 0.4 (X^{1-}). The linewidths are almost the same, and are a factor of 1.4 (X^0), 2.0 (X^{1-}) larger than the transform limit ($\Gamma_0^{X^0} = 0.92 \pm 0.10$ μeV, $\Gamma_0^{X^{1-}} = 0.75 \pm 0.10$ μeV). The increase above the transform-limit, $\Gamma - \Gamma_0$, represents a sum over all noise sources from the measurement frequency, about 1 Hz, to Γ_0, about 1 GHz. Our strategy to determine the pertinent noise process, charge or spin, is to identify the contributions of charge noise and spin noise in $N_{QD}(f)$ separately.

Noise spectra for X^{1-} and X^0 are shown in Fig. 5.2. In both cases, there is a roll-off feature in the noise at low frequencies (linewidth $\sim$ 30 Hz) arising from charge noise and a second roll-off feature at higher frequencies (linewidth $\sim$ 200 kHz (X^0), 10 kHz (X^{1-})) arising from spin noise. (The key evidence is the change in N_{QD} on X^{1-} on switching from $\delta = 0$ to $\delta = \Gamma/2$ which increases/decreases the sensitivity to charge/spin noise [17].) The two components can be integrated separately: the f-sum over the charge noise gives a contribution to Γ of < 0.05 μeV for both X^0 and X^{1-} (see Appendix C), a negligible value. The electrical noise in the device is so low that the contribution to the optical linewidth is irrelevant despite the large Stark shifts.

If exciton dephasing from charge noise is irrelevant then spin noise must be important. This is surprising as X^0 and X^{1-} respond in quite different ways to an Overhauser field – X^{1-} has a first order response, X^0 only a second order response, Fig. 5.1 – yet
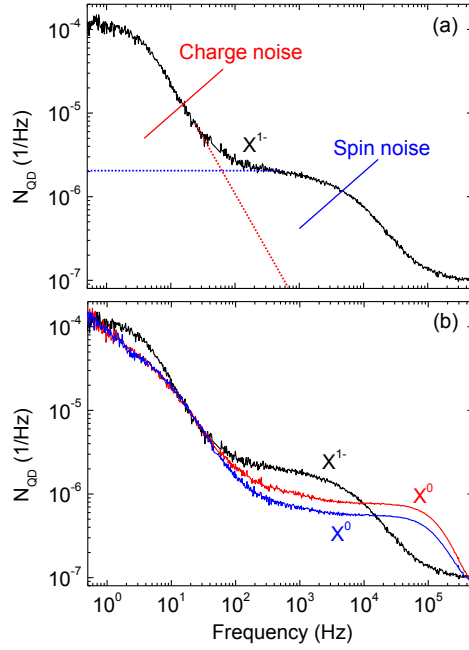
Fig. 5.2. (a) Power spectrum of quantum dot noise, $N_{\mathrm{QD}}(f)$, as determined from a time trace of the X^{1-} resonance fluorescence showing charge noise and spin noise. (b) $N_{\mathrm{QD}}(f)$ from X^0 "blue" and "red" resonance fluorescence. Data on quantum dot from Fig. 1 recorded at $B = 0.0$ mT and 4.2 K.

$\Gamma^{X^0} \simeq \Gamma^{X^{1-}}$. The noise spectra enable us to resolve this conundrum. In the bandwidth where spin noise dominates, $f > 1$ kHz, $N_{\mathrm{QD}}(f)$ on X^{1-} is only slightly larger than $N_{\mathrm{QD}}(f)$ on X^0 despite the huge difference in sensitivity to B_N, Fig. 5.2. A quantitative analysis (see Appendix C) shows that $B_{N,\mathrm{rms}}^{X^0} = 210 \pm 20$ mT yet $B_{N,\mathrm{rms}}^{X^{1-}} = 9 \pm 3$ mT. Concomitant with the different $B_{N,\mathrm{rms}}$ values are the associated B_N-correlation times, much shorter for X^0 (5 μs) than for X^{1-} (100 μs). Without optical excitation, $B_{N,\mathrm{rms}} \sim 20$ mT[25], and arises from incomplete cancellation of the hyperfine interaction in the mesoscopic-like nuclear spin ensemble of $N \sim 10^5$ nuclei[18,19]. A clear result emerges: the noise in the nuclear spin ensemble is massively increased over its "dark" value when X^0 is driven resonantly. X^0 has a much larger $B_{N,\mathrm{rms}}$ than X^{1-} yet the broadening of X^0 is much less sensitive to $B_{N,\mathrm{rms}}$ than X^{1-}: the two features conspire to give similar optical linewidths.

The Ω-dependence of $N_{\mathrm{QD}}(f)$ is highly revealing, Fig. 5.3. As Ω increases, the X^0 spin noise *increases*, Fig. 5.3(a). $B_{N,\mathrm{rms}}^{X^0}$ increases roughly linearly with Ω reaching at the highest couplings extremely high values, 300 mT, Fig. 5.3(b). In complete contrast, the X^{1-} spin noise *decreases* as Ω increases, Fig. 5.3(c), equivalently $B_{N,\mathrm{rms}}^{X^{1-}}$. Resonant laser excitation *increases* the nuclear spin noise on an empty quantum dot, yet

63
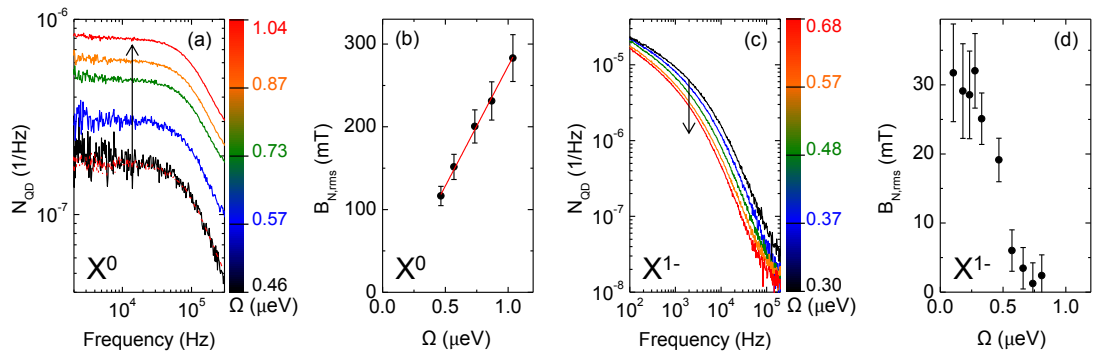
Fig. 5.3. ((a) $N_{QD}(f)$ on X^0 for a series of Rabi couplings Ω at $B = 10.0$ mT. The experimental data for $\Omega = 0.46$ μeV (black curve) is accompanied by the Monte Carlo fit (red dashed curve). (c) $N_{QD}(f)$ on X^{1-} for a series of Rabi couplings Ω (taken at $B = 10.0$ mT to enhance the sensitivity to spin noise[17]). (b),(d) $B_{N,rms}$ versus Ω for X^0, X^{1-}. All data on same quantum dot as Figs 1 and 2.

decreases the nuclear spin noise when the same quantum dot is occupied with a single electron. ($B_{N,rms}^{X^0}$ is determined by a Monte Carlo simulation of $N_{QD}(f)$ of an ensemble of fluctuating nuclei – this is robust as X^0 is sensitive only to the vertical component of B_N (see Appendix C). X^{1-} responds to all three components of B_N, a more complex problem, and instead $B_{N,rms}^{X^{1-}}$ is determined with lower systematic error from the 2-laser experiment.)

We address whether the spin noise reduction in the case of X^{1-} is sufficient to achieve transform-limited optical linewidths. The Ω-dependence of $\Gamma^{X^{1-}}$ can be described extremely well with the two-level result including an inhomogeneous broadening γ, Fig. 5.4(b) (see Appendix C). At low Ω, Γ is determined by Γ_0 and γ; at higher Ω, Γ increases ("power broadening") and γ becomes irrelevant. The solid line in Fig. 5.4(b) therefore represents the ideal limit (Γ versus Ω with $\gamma = 0$). A linewidth measurement is complex in the sense that the spin noise is a function of both Rabi energy and detuning. To simplify matters, we performed the experiment with two lasers. The concept is that the stronger, constant frequency pump laser (Ω_2, δ_2) determines the nuclear spin noise, and the weaker probe laser (Ω_1, δ_1) measures the optical linewidth. Fig. 5.4(a) shows $\Gamma^{X^{1-}}$ measured by sweeping δ_1 versus δ_2 for $\Omega_1 = 0.23, \Omega_2 = 0.80$ μeV. For large δ_2, the pump laser has no effect on Γ; power broadening is irrelevant and Γ is far from the transform limit. For small δ_2 however, Γ decreases, despite the power broadening induced by Ω_2. Taking into account power broadening, Γ reduces to the ideal limit. Fig. 5.4(b) shows the results as Ω_2 increases: for $\Omega/\Gamma_0 > 0.75$, ideal linewidths are achieved.

The spin noise reduction on driving X^{1-} with the pump laser is accompanied by a profound change in the probe spectrum: the optical resonance now splits into two
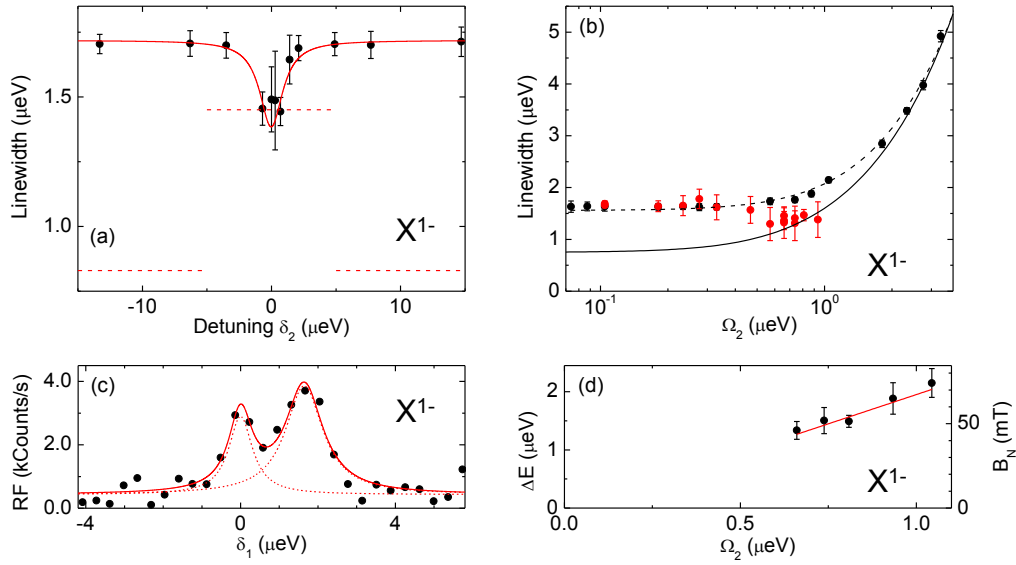
Fig. 5.4. Results of the two-laser experiment ($B = 0.0$ mT, $T = 4.2$ K) on X^{1-}. (a) optical linewidth measured with the probe laser ($\Omega_1 = 0.23$ μeV) versus detuning of the pump laser δ_2 for $\Omega_2 = 0.80$ μeV. The dashed lines show the ideal case (zero inhomogeneous broadening) in two limits, $\Omega = \Omega_1$ and $\Omega = \Omega_1 + \Omega_2$, appropriate for large δ_2 and $\delta_2 = 0.0$ μeV, respectively, the difference arising from power broadening. (b) Optical linewidth in one-laser experiment (black points) versus Ω with fit to 2-level model ($\gamma = 1.35$ μeV, black curve). The optical linewidth in two-laser experiment ($\Omega_1 = 0.23$ μeV, $\delta_2 = 0$) versus Ω_2 (red points). (c) Probe spectrum with $\Omega_1 = 0.23$ μeV, $\Omega_2 = 0.80$ μeV and $\delta_2 = 0.0$ μeV (points) with a two Lorentzian fit (solid line, energy separation 1.6 μeV, linewidths 0.8 ± 0.3, 1.2 ± 0.3 μeV). (e) Splitting from (d) versus Ω_2.

resonances, Fig. 5.4(c). The splitting reflects a static electron Zeeman splitting in the single electron ground-state, $B_N = 58$ mT in Fig. 5.4(c), with B_N increasing with Ω_2, Fig. 5.4(d). Equivalently, even without an applied magnetic field[26], a nuclear spin polarization is created by the optical coupling. This demonstrates that the laser locks the nuclear spins into an eigenstate of the ΣI_z operator.

The mechanisms underpinning the increase (X^0) and decrease (X^{1-}) in charge noise on resonant excitation are unknown. We speculate that in the case of X^{1-}, the laser scattering with the narrow band laser constitutes a projective measurement of the nuclear spin ensemble, and that an analogy may be drawn to the quantum Zeno effect[27]. In the case of X^0, the excited states are antisymmetric ("red") and symmetric ("blue") combinations of the two bright states ($J_z = \pm 1$) and are therefore not eigenstates of the spin operator S_z which we speculate leads to a quantum anti-Zeno effect in the nuclear spin ensemble.

It is surprising that the nuclear spins and not charge noise dominate the optical

linewdiths of both quantum dot excitons in this regime (low temperature, high quality material, resonant excitation) as the hyperfine interaction is weak, the Stark effect strong[28,29]. We mention other evidence which supports this result. First, there are strong hints that the "blue" X^0 has a smaller linewidth than the "red" X^0 (see Appendix C). This is impossible to explain with a charge noise model: both excitons experience exactly the same electrical fluctuations and have equal Stark coefficients (see Appendix C) resulting in identical charge noise, Fig. 5.2(b). The spin noise is however higher for the red X^0, Fig. 5.2(b), consistent with the larger linewidth. Secondly, both the Stark coefficient and the optical linewidth vary from quantum dot to quantum dot yet there is no correlation between the two (see Appendix C), pointing also to the unimportance of charge noise in the optical linewidth. Thirdly, several groups have reported similar linewidths on samples from different sources[13–15,20] yet charge noise can be highly variable from one sample to the next. This hints at a common, fundamental noise source, identified here as the nuclear spins. Finally, single photons generated not by spontaneous emission but by coherent Rayleigh scattering from the X^0 in the limit $\Omega \ll \Gamma_0$ are faithful replicas of the laser field[4–6]. In the light of the experiments presented here, it becomes clearer why: charge noise is too small and too slow to dephase X^0 significantly; X^0 nuclear spin noise at very low Ω is close to the $\Omega = 0$ limit; the fine structure protects the X^0 from the residual nuclear spin noise.

5.4 Conclusion

In conclusion, we demonstrate the dominant role of nuclear spin noise and not charge noise in inducing slow dephasing of quantum dot excitons. Resonant laser excitation increases the nuclear spin noise for an empty quantum dot yet decreases nuclear spin noise for a quantum dot occupied with a single electron. With laser-cooled nuclei, transform-limited optical linewidths are demonstrated even when the linewidths are measured very slowly. It is therefore possible to generate truly indistinguishable photons from the same solid-state emitter even when the photons are created at widely different moments in time.

References

1. Michler, P., Kiraz, A., Becher, C., Schoenfeld, W. V., Petroff, P. M., Zhang, L. D., Hu, E., and Imamoglu, A. *Science* **290**, 2282 (2000).

2. Santori, C., Fattal, D., Vuckovic, J., Solomon, G. S., and Yamamoto, Y. *Nature* **419**, 594–597 (2002).

3. Shields, A. J. *Nature Photon.* **1**, 215–223 (2007).

4. Nguyen, H. S., Sallen, G., Voisin, C., Roussignol, P., Diederichs, C., and Cassabois, G. *Appl. Phys. Lett.* **99**, 261904 (2011).

5. Matthiesen, C., Vamivakas, A. N., and Atatüre, M. *Phys. Rev. Lett.* **108**, 093602 (2012).

6. Matthiesen, C., Geller, M., Schulte, C. H. H., Le Gall, C., Hansom, J., Li, Z., Hugues, M., Clarke, E., and Atatüre, M. *Nat. Commun.* **4**, 1600 (2013).

7. Dalgarno, P. A., Smith, J. M., McFarlane, J., Gerardot, B. D., Karrai, K., Badolato, A., Petroff, P. M., and Warburton, R. J. *Phys. Rev. B* **77**, 245311 (2008).

8. Langbein, W., Borri, P., Woggon, U., Stavarache, V., Reuter, D., and Wieck, A. D. *Phys. Rev. B* **70**, 033301 (2004).

9. Bayer, M. and Forchel, A. *Phys. Rev. B* **65**, 041308 (2002).

10. Kroner, M., Remi, S., Högele, A., Seidl, S., Holleitner, A. W., Warburton, R. J., Gerardot, B. D., Petroff, P. M., and Karrai, K. *Physica E* **40**, 1994–1996 (2008).

11. Ramsay, A. J., Gopal, A., Gauger, E. M., Nazir, A., Lovett, B. W., Fox, A. M., and Skolnick, M. S. *Phys. Rev. Lett.* **104**, 017402 (2010).

12. Ulrich, S. M., Ates, S., Reitzenstein, S., Löffler, A., Forchel, A., and Michler, P. *Phys. Rev. Lett.* **106**, 247402 (2011).

13. Högele, A., Seidl, S., Kroner, M., Karrai, K., Warburton, R. J., Gerardot, B. D., and Petroff, P. M. *Phys. Rev. Lett.* **93**, 217401 (2004).

14. Houel, J., Kuhlmann, A. V., Greuter, L., Xue, F., Poggio, M., Gerardot, B. D., Dalgarno, P. A., Badolato, A., Petroff, P. M., Ludwig, A., Reuter, D., Wieck, A. D., and Warburton, R. J. *Phys. Rev. Lett.* **108**, 107401 (2012).

15. Atatüre, M., Dreiser, J., Badolato, A., Högele, A., Karrai, K., and Imamoglu, A. *Science* **312**, 551–553 (2006).

16. Warburton, R. J., Schulhauser, C., Haft, D., Schäflein, C., Karrai, K., Garcia, J. M., Schoenfeld, W., and Petroff, P. M. *Phys. Rev. B* **65** (2002).

17. Kuhlmann, A. V., Houel, J., Ludwig, A., Greuter, L., Reuter, D., Wieck, A. D., Poggio, M., and Warburton, R. J. *Nature Phys.* **9**, 570–575 (2013).

18. Merkulov, I. A., Efros, A. L., and Rosen, M. *Phys. Rev. B* **65**, 205309 (2002).

19. Khaetskii, A. V., Loss, D., and Glazman, L. *Phys. Rev. Lett.* **88**, 186802 (2002).

20. Xu, X., Sun, B., Berman, P. R., Steel, D. G., Bracker, A. S., Gammon, D., and Sham, L. J. *Nature Phys.* **4**, 692–695 (2008).

21. Press, D., De Greve, K., McMahon, P. L., Ladd, T. D., Friess, B., Schneider, C., Kamp, M., Hoefling, S., Forchel, A., and Yamamoto, Y. *Nature Photon.* **4**, 367–370 (2010).

22. Warburton, R. J. *Nature Mater.* **12**, 483 – 493 (2013).

23. Warburton, R. J., Schaflein, C., Haft, D., Bickel, F., Lorke, A., Karrai, K., Garcia, J. M., Schoenfeld, W., and Petroff, P. M. *Nature* **405**, 926–929 (2000).

24. Kuhlmann, A. V., Houel, J., Brunner, D., Ludwig, A., Reuter, D., Wieck, A. D., and Warburton, R. J. *Rev. Sci. Instrum.* **84**, 073905 (2013).

25. Braun, P. F., Marie, X., Lombez, L., Urbaszek, B., Amand, T., Renucci, P., Kalevich, V. K., Kavokin, K. V., Krebs, O., Voisin, P., and Masumoto, Y. *Phys. Rev. Lett.* **94**, 116601 (2005).

26. Chekhovich, E. A., Makhonin, M. N., Kavokin, K. V., Krysa, A. B., Skolnick, M. S., and Tartakovskii, A. I. *Phys. Rev. Lett.* **104**, 066804 (2010).

27. Klauser, D., Coish, W. A., and Loss, D. *Phys. Rev. B* **78**, 205301 (2008).

28. Schulhauser, C., Haft, D., Warburton, R. J., Karrai, K., Govorov, A. O., Kalameitsev, A. V., Chaplik, A., Schoenfeld, W., Garcia, J. M., and Petroff, P. M. *Phys. Rev. B* **66**, 193303 (2002).

29. Vamivakas, A. N., Zhao, Y., Fält, S., Badolato, A., Taylor, J. M., and Atatüre, M. *Phys. Rev. Lett.* **107**, 166802 (2011).

Chapter 6

Conclusions and Outlook

In this thesis the resonance fluorescence from single semiconductor quantum dots is used to investigate noise in a semiconductor quantum device. The two main sources of noise, charge noise and spin noise, are identified and explored quantitatively. Strategies to circumvent the deleterious effects of the noise are implemented and the quantum performance of the devices is improved.

Resonance fluorescence is introduced as a novel technique of coherent laser spectroscopy of single semiconductor quantum dots. A polarization-based dark-field microscope is developed with excellent figures of merit, state-of-the art, or better: the excitation laser is suppressed in the detection beam path by up to 8 orders of magnitude; even with a modest light collection efficiency, resonance fluorescence can be measured with a signal-to-background ratio exceeding $10^4 : 1$. However, most impressive is the microscope's stability. It can be operated for many days in a set-and-forget mode. The resonance fluorescence displaces the differential transmission detection in the field of coherent laser spectroscopy for practical reasons. The signal-to-background ratio of resonance fluorescence exceeds by far the one of transmission measurements even without lock-in detection for noise rejection. Furthermore, the resonance fluorescence provides direct access to the single photons scattered or emitted by a quantum dot. The microscope can be developed further in some simple ways. For instance, it may be valuable to include a way of rotating the microscope basis relative to the crystal axes or even to operate the microscope with σ^+/σ^- polarizations. Whereas the microscope's achromaticity is improvable, the laser suppression is more than sufficient. The next step is to increase the light collection efficiency that is limited by the high refractive index of the sample. Candidate structures are resonant micro-cavities, photonic nanowires or ultra-high index solid immersion lenses. The challenge is to increase the light collection efficiency without increasing charge noise due to the presence of close-by free surfaces. Towards an ultra-bright source of single photons the resonance

69

fluorescence provides a tool to investigate how the sample structure affects charge noise.

In chapter 2 local charge fluctuations in a semiconductor are probed with high resolution laser spectroscopy on a nearby single quantum dot. A self-assembled quantum dot is extremely sensitive to the local electrical field via the Stark effect. Single charge fluctuations in the occupation of a small number of defects located within $\sim 100\,\text{nm}$ of the quantum dot are observed. An additional non-resonant excitation allows the occupation of these close-by defects to be controlled. Remarkably, for heterostructures with $30\,\text{nm}$ capping layer thickness the quantum dot resonance evolves with a series of steps in energy as the non-resonant excitation power increases. The steps reflect a change of just one hole in occupation of the localization centres close to the quantum dot. The number of steps and their energy separation is highly quantum dot dependent reflecting the quantum dot's local environment. Monte Carlo simulations enable the main source of charge noise to be identified and quantitatively analysed: holes fluctuating at localization centres at the capping layer/blocking barrier interface. The radial distance of the defects from the quantum dot is determined with $\pm 5\,\text{nm}$ resolution. Once the defects are fully occupied at high non-resonant excitation power, there is a strong suppression of the charge noise. This understanding is tested in an improved heterostructure in which the fluctuators are positioned further away from the quantum dot. The capping layer thickness is increased from $30\,\text{nm}$ to $150\,\text{nm}$. As predicted by the model, this change reduces significantly the quantum dot optical linewidth. The average linewidth for quantum dots with increased capping layer is $1.60\,\mu\text{eV}$ with standard deviation $0.22\,\mu\text{eV}$, yet a factor of 2 above the transform limit. A large capping layer in a field-effect heterostructure is therefore an important step in reducing charge noise as it positions the fluctuating charges far enough from the quantum dots for their influence to be minimized. Eliminating these fluctuating holes completely may be challenging as they arise from a p-type background doping during the growth process, underlining the need of ultra-pure quality material.

There are two sources of noise inherent to a semiconductor, charge noise and spin noise. The origin of charge noise is identified and quantitatively analysed in chapter 2. The frequency dependence and the origin of charge noise and spin noise are revealed in chapter 3. Noise is investigated in an ultra-pure semiconductor device using a minimally-invasive, ultra-sensitive, local probe: resonance fluorescence from a single quantum dot. Noise spectra with 6 decades of resolution in the noise power over 6 decades of frequency, from $0.1\,\text{Hz}$ to $100\,\text{kHz}$, are presented. Significantly, charge noise

is distinguished from spin noise. Charge noise gives large noise powers but only at low frequencies; spin noise gives weaker noise powers but over a much larger bandwidth. Remarkably, the full spectrum of the fluctuating nuclear spin ensemble is revealed. Noise spectra for both electric and magnetic fields are derived. The integrated charge noise is very small and implies a linewidth broadening of $< 0.05\,\mu\text{eV}$. The rms noise in the Overhauser field measured on X^0 amounts to $B_{N,\text{rms}} = 193$ mT; $B_{N,\text{rms}}$ measured on X^{1-} is smaller, $9\,\text{mT}$. For X^0, continuous resonant excitation agitates the nuclear spins. The $B_{N,\text{rms}}$ values enable the observed linewidths to be reproduced, thus, spin noise and not charge noise is the dominant exciton dephasing process. The X^{1-} correlation time, a few tens of μs, identify the process responsible for the spin noise as the nuclear spin dipole-dipole interaction. The noise falls rapidly with increasing frequency such that transform-limited quantum dot optical linewidths are demonstrated by operating the device above 50 kHz. Furthermore, the negative effect of non-resonant excitation is demonstrated: non-resonant excitation introduces charge noise to the device.

This technique is potentially capable of mapping the noise from sub-Hz frequencies up to the GHz regime where spin noise corresponding to electron spin precession in B_N may be revealed. The high frequency limit is limited only by the photon flux which can be increased relatively simply using either a micro-cavity, a photonic nanowire or a high refractive index solid immersion lens to enhance the photon extraction efficiency from the device. The charge noise is measured here in a simple device and represents a baseline for the local charge noise in an ultra-pure semiconductor. The noise probe can be applied to micro- or nano-structured devices. The technique opens a new route to probing spin noise. Its dependence on external magnetic field, charge state of the quantum dot, laser excitation etc. can all be probed simply by recording time traces of the RF. The experiment demonstrates that the dephasing processes which limit the T_2^* of the quantum dot exciton are all slow with respect to radiative recombination. This result points to the possibilities of achieving close to dephasing-free qubit operations by working at very high frequencies or at lower frequencies by exploiting echo-like schemes.

Charge noise and spin noise cause the quantum dot emission wavelength to fluctuate. This problem is solved in chapter 4 with a dynamic feedback technique that locks the quantum dot emission frequency to a reference in order to produce a stream of frequency-stabilized single photons via resonance fluorescence. The noise in the device is reduced up to a frequency of $\sim 100\,\text{Hz}$. Thus, the scheme represents a way to reduce the local charge noise in a semiconductor. Now that the basic principle is established, there are options for improving the feedback scheme. First, the remaining jitter in the

quantum dot resonance position can be reduced by reducing the noise in the transmission detection. Presently, the performance is far from the limit defined by the shot noise in the detector current. With lower noise, the feedback bandwidth can also be increased. The tantalizing prospect is to create transform-limited linewidths routinely with high bandwidth feedback. A bandwidth of about 50 kHz is required. Secondly, the modulation required here to generate the error signal could be eliminated in a number of ways. For instance, a dispersive lineshape can arise naturally in reflectivity via weak coupling to a cavity; or the Faraday effect in a small magnetic field could be used.

There are two obvious culprits for the quantum dot optical linewidth, charge noise and spin noise. Even with high quality material at low temperature, the optical linewidths are a factor of two larger than the transform limit. It is demonstrated in chapter 5 that the inhomogeneous contribution to the linewidth is caused by spin noise. The charge noise is so low that the contribution to the linewidth is irrelevant. Resonant laser excitation increases the nuclear spin noise for the neutral exciton yet decreases nuclear spin noise for the charged exciton. With laser-cooled nuclei, transform-limited optical linewidths are demonstrated even when the linewidths are measured very slowly. It is therefore possible to generate truly indistinguishable photons from the same solid-state emitter even when the photons are created at widely different moments in time.

Appendix A

Supplementary information to chapter 2 "Charge fluctuations in a semiconductor"

In chapter 2 "Charge fluctuations nearby a quantum dot", a single quantum dot is used as a nano-sensor of its own local electrical environment. The understanding of the local electrical fluctuations has led to a new sample design where close-to-transform-limited linewidths are routinely achieved. These conclusions rely on experimental results which we model with Monte Carlo simulations. The details of the simulation are explained in this supplementary information. We explain how the input parameters are determined and how the results depend on the defect density, defect position and occupation probability.

A.1 Monte Carlo simulation of the charge fluctuations: calculation

A.1.1 Stark shift

The interpretation of the experiments relies on the dc Stark effect of the single negatively charged exciton, X^{1-}. The dependence of the X^{1-} emission energy as a function of an external electric field $\mathbf{F}_0$ is given by[1]:

$$E_{X^{1-}}^{(1)} = E_0 + \Sigma_{i=x,y,z}(-p_i F_{0,i} + \beta_i F_{0,i}^2) \tag{A.1}$$

where p_i, β_i and $F_{0,i}$ are the permanent dipole moment, the polarizability and the bare electric field in direction i, respectively. The emission energy with an additional electric field $\mathbf{F}_h$ is similarly given by:

$$E_{X^{1-}}^{(2)} = E_0 + \Sigma_{i=x,y,z}(-p_i (F_{0,i} + F_{h,i}) + \beta_i (F_{0,i} + F_{h,i})^2). \tag{A.2}$$

The energy shift ΔE induced by the additional electric field $\mathbf{F}_h$ is then given by:

$$\Delta E = E_{X^{1-}}^{(2)} - E_{X^{1-}}^{(1)} = \Sigma_{i=x,y,z}(-p_i F_{h,i} + \beta_i F_{h,i}(F_{h,i} + 2F_{0,i})). \tag{A.3}$$

A.1.2 Electric field created by a single hole

We consider a single positive charge located at distance d_{cap} from the QD in the growth direction (z), at lateral coordinate $\mathbf{r} = (x,y) = (r,\theta)$ with the dot at $\mathbf{r} = 0$, Fig. A.1. The back contact is treated as a metallic layer, implying the creation of a negative image charge. The resulting potential is then given by:

$$V_h(x,y,z) = \frac{e}{4\pi\varepsilon_0\varepsilon_r} \left[\frac{1}{\sqrt{(\delta - z)^2 + x^2 + y^2}} - \frac{1}{\sqrt{(\delta + z)^2 + x^2 + y^2}} \right]. \tag{A.4}$$

The electric field created by this single charge is deduced from $\mathbf{F}_h = -\nabla V_h$:

$$
\begin{aligned}
F_{h,x}(x,y,z) &= \frac{ex}{4\pi\varepsilon_0\varepsilon_r} \left[\frac{1}{((\delta - z)^2 + x^2 + y^2)^{\frac{3}{2}}} - \frac{1}{((\delta + z)^2 + x^2 + y^2)^{\frac{3}{2}}} \right], \\
F_{h,y}(x,y,z) &= \frac{ey}{4\pi\varepsilon_0\varepsilon_r} \left[\frac{1}{((\delta - z)^2 + x^2 + y^2)^{\frac{3}{2}}} - \frac{1}{((\delta + z)^2 + x^2 + y^2)^{\frac{3}{2}}} \right], \\
F_{h,z}(x,y,z) &= \frac{-e}{4\pi\varepsilon_0\varepsilon_r} \left[\frac{\delta - z}{((\delta - z)^2 + x^2 + y^2)^{\frac{3}{2}}} + \frac{\delta + z}{((\delta + z)^2 + x^2 + y^2)^{\frac{3}{2}}} \right].
\end{aligned}
\tag{A.5}
$$
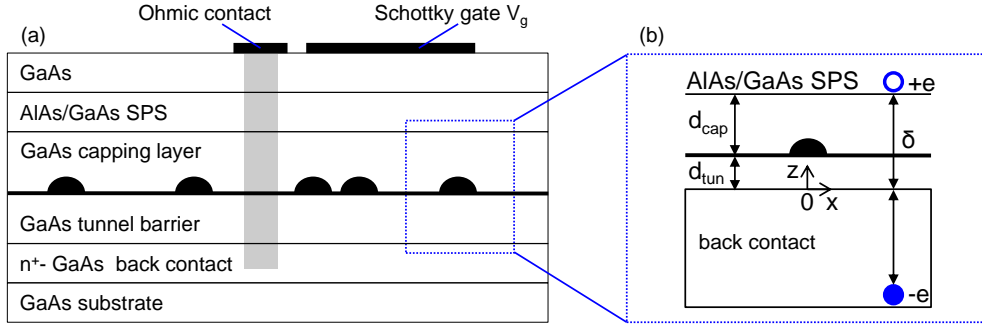
Fig. A.1. (a) Sample layer structure. The active layer consists of a layer of quantum dots, a GaAs tunnel barrier below the QDs and a GaAs capping layer above. An AlAs/GaAs short period superlattice (SPS) is grown on top of the capping layer. The Schottky gate is a semi-transparent metal layer deposited on the sample surface. Ohmic contacts are prepared to the back contact. (b) Zoom-in of the active region in (a). A QD is separated from the capping layer/SPS interface by distance d_{cap} and from the back contact by distance d_{tun}. A single hole is shown at the capping layer/SPS interface at $z = \delta$, creating a negative image charge at $z = -\delta$.

The electric field at the location of the QD is given by Eq. A.5 with $z = d_{tun}$.

A.1.3 Stark shift parameters in the growth direction

In the growth direction, the dipole moment and polarizability, p_z and β_z, are determined by fitting the voltage dependence of the X^{1-} photoluminescence (PL) emission spectrum[1]. The non-resonant laser in PL experiments creates stored holes at the capping layer/short period superlattice (SPS) interface, a space charge, shifting the charging plateau in gate voltage. In this case, $F_{0,z}$ is given by:

$$F_{0,z} = \frac{V_0 - V_g}{D} + \Delta F_{NR} \tag{A.6}$$

where V_g, V_0 and D are the applied gate voltage, the Schottky barrier of the gate, and the back contact to surface distance, respectively. ΔF_{NR} is the additional electric field arising from the space charge. ΔF_{NR} is determined by insisting that the local absorption shift measured with resonant laser spectroscopy, $765\,\mu eV/V$ for the QD of sample A (see chapter 2), is reproduced. For this particular QD, the fixed parameters

are $D = 175\,\text{nm}$, $V_\text{g} = -0.05\,\text{V}$ and $V_0 = 0.62\,\text{V}$. From the fit, we obtain:

$$
\begin{aligned}
p_\text{z} &= -0.231\,\text{nm} \\
\beta_\text{z} &= -0.386\,\mu\text{eV}/(\text{kV}/\text{cm})^2 \\
\Delta F_\text{NR} &= 9.0\,\text{kV}/\text{cm}.
\end{aligned}
\tag{A.7}
$$

A.1.4 Stark shift parameters in the QD plane

The in-plane permanent dipole moments p_x and p_y are assumed to be zero[2]. Assuming a harmonic confining potential, the polarizability in the QD plane is given by[3]:

$$
\beta_\text{x} = \beta_\text{y} = -e^2 \frac{m_\text{e} l_\text{e}^4 + m_\text{h} l_\text{h}^4}{2\hbar^2}
\tag{A.8}
$$

where $m_\text{e} = 0.07\,\text{m}_\text{o}$ and $m_\text{h} = 0.25\,\text{m}_\text{o}$ are the electron and hole in-plane effective masses, and l_e and l_h are the lateral extents of the electron and hole wave functions, respectively[1]. The parameters l_e and l_h can be determined from the PL charging diagram[3]; specifically, from the extent of the neutral exciton charging plateau $\Delta V(\text{X}^0)$ and from the PL energy difference between X^{1-} and X^0, $\Delta E_\text{PL}(\text{X}^{1-} - \text{X}^0)$[4]. l_e can be expressed as a function of the electron-electron interaction energy in the ground state E_ee^ss:

$$
l_\text{e} = \frac{e^2}{4\pi\varepsilon_0\varepsilon_\text{r}}\sqrt{\frac{\pi}{2}}\frac{1}{E_\text{ee}^\text{ss}},
\tag{A.9}
$$

with[3]:

$$
E_\text{ee}^\text{ss} = \frac{\Delta V(\text{X}^0)}{\lambda} - 2E_\text{j}
\tag{A.10}
$$

where λ is the sample lever arm and E_j the Coulomb energy of an electron in the QD with its image charge in the back contact ($E_\text{j} = 1.1\,\text{meV}$ for $d_\text{tun} = 25\,\text{nm}$). Once l_e is known, l_h can be determined from the electron-hole Coulomb energy:

$$
E_\text{eh}^\text{ss} = \frac{e^2\sqrt{\pi}}{4\pi\varepsilon_0\varepsilon_\text{r}}\frac{1}{\sqrt{l_\text{e}^2 + l_\text{h}^2}} = E_\text{ee}^\text{ss} - \Delta E_\text{PL}(\text{X}^{1-} - \text{X}^0).
\tag{A.11}
$$

This gives $l_\text{e} = 4.24\,\text{nm}$ and $l_\text{h} = 2.45\,\text{nm}$ for the QD from sample A in chapter 2, leading to $\beta_\text{x} = \beta_\text{y} = -2.06\,\mu\text{eV}/(\text{kV}/\text{cm})^2$. Finally, as the applied electric field is in the growth direction, we take $F_{0,\text{x}} = F_{0,\text{y}} = 0$.

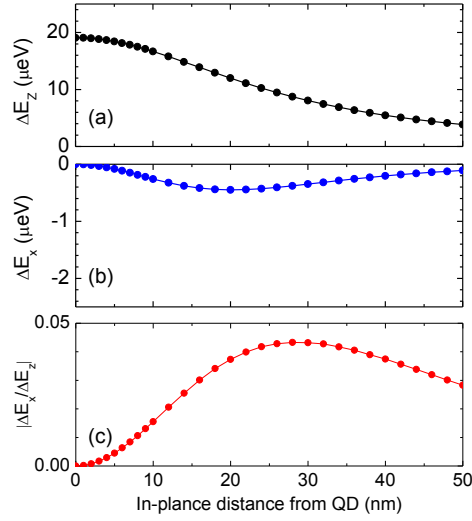Fig. A.2. (a) ΔE_z and (b) ΔE_x as a function of the in-plane defect distance from the QD, calculated using the parameters from sections A.1.3 and A.1.4. (b) Ratio $|\Delta E_x/\Delta E_z|$ as a function of the in-plane defect distance from the QD. The in-plane Stark shift is always more than one order of magnitude smaller than the Stark shift in the growth direction. The largest ratio is $|\Delta E_x/\Delta E_z| \approx 4\%$.

A.1.5 Stark shifts: growth direction versus in-plane fields

With the parameters obtained above for the QD in sample A, we compare the contributions of electric fields and Stark shifts generated in the growth and in-plane directions for $d_{\text{cap}} = 30\,\text{nm}$ and $d_{\text{tun}} = 25\,\text{nm}$. As a typical case, we consider a single hole trapped at the capping layer/SPS interface with in-plane coordinates $(x, y) = (10, 0)\,\text{nm}$. We obtain:

$$
\begin{aligned}
F_z &= -1.29\,\text{kV/cm} \\
F_x &= -0.35\,\text{kV/cm} \\
F_y &= 0 \\
\Delta E_z &= 16.7\,\mu\text{eV} \\
\Delta E_x &= -0.26\,\mu\text{eV} \\
\Delta E_y &= 0.
\end{aligned}
\tag{A.12}
$$

We observe that the effect of the in-plane component is two orders of magnitude smaller than that in the growth direction. We generalize this comparison in Fig. A.2 where ΔE_z, ΔE_x and the ratio $|\Delta E_x/\Delta E_z|$ are plotted as a function of the in-plane defect location, showing that for all x, $|\Delta E_x| \ll |\Delta E_z|$.

A.1.6 The Monte Carlo population of the defects with holes

An array of defects is considered at the capping layer/SPS interface. The defects are populated randomly in a Monte Carlo simulation. Defect i is populated with a weighted probability $\alpha_i p$, where p is the control parameter of the simulations, $0 \leq p \leq 1$. $\alpha_i p$ rises with p until it reaches 100%; at larger values of p, the probability is clamped to 100%. The α-parameter can change from defect to defect and represents, at a particular p, the relative probability of occupying a particular localization centre. Its value is $\alpha_i \geq 1$ for all i to ensure that all the defects are populated at $p = 1$.

A defect array is defined, specifying for each defect the location (x_i, y_i) and the weighting factor α_i. A value of p is then chosen. Each defect is "tested" with respect to a random number g, $0 \leq g \leq 1$. If $\alpha_i p > g$, defect i is populated with one hole. If $\alpha_i p \leq g$, defect i is not populated. This process is repeated for each defect, generating a new random number g for each defect. In this way, a distribution of localized charges at the capping layer/SPS interface is created. The electric field at the location of the quantum dot arising from the localized holes is calculated by adding up the electric field from each localized charge (repeated use of Eq. A.5). The Stark shift of the optical transition is then calculated with Eq. A.3. These successive steps consider one and only one particular charge distribution at the interface. In order to reproduce the experiments, we run this procedure N times. From one run to the next, the spatial distribution of the defects remains the same, as does the control variable p, but otherwise the runs are not correlated with each other. The final optical spectrum is a sum over N runs. The entire process is then repeated as a function of p.

A.1.7 Spatial modulation of the probability of occupation

In order to include the Gaussian beam profile of the non-resonant excitation, the weighting factors α_i are multiplied by a normalized Gaussian function, the Gaussian a function of r_i, centred on the QD, with a full width at half maximum (FWHM) Γ_{L}.

A.1.8 Exciton inhomogeneous broadening

The exciton spectrum is broadened, in general with homogeneous and inhomogeneous components. Each discrete energy shift obtained in the simulation is replaced with a normalized Lorentzian with full-width-at-half-maximum Γ. For sample A, we take $\Gamma = 2.5\ \mu\mathrm{eV}$, an inhomogeneous broadening. For samples B and C, we take $\Gamma = 0.8\ \mu\mathrm{eV}$ corresponding to homogeneous broadening, equivalently the radiative lifetime-limited linewidth, the so called "transform limit".

A.2 Monte Carlo simulation of the charge fluctuations: results

A.2.1 The defect array

We present initially simulation results obtained with $d_{\text{tun}} = 25\,\text{nm}$, $d_{\text{cap}} = 30\,\text{nm}$, corresponding to samples A and B, using a full 2D array of randomly placed defects with density N_{2D}. Fig. A.3 shows example simulation results, energy shift versus p, from a set of 500 runs using the Stark shift parameters for the QD in sample A and with $N_{2D} = 1 \times 10^{10}\,\text{cm}^{-2}$. We find that, first, a large percentage of the simulations show a monotonous Stark shift as a function of p without any steps (56.8 %; 284 occurrences in the 500 Monte Carlo simulations). Two typical examples are shown in Fig. A.3(a),(b). Some other simulations exhibit clearly-resolved steps of the Stark shift, Fig. A.3(c),(d). In this simulation set, only 1 of the 500 runs exhibits 5 steps, a probability of $\sim 0.2\,\%$. The probability of 4 steps is $\sim 0.4\,\%$; the probability of 3 steps $\sim 4.2\,\%$. The probability of steps occurring is even smaller for a lower value of N_{2D}. At higher values of N_{2D}, steps are more likely, but the transition from one step to the other becomes progressively more blurred such that above $6 \times 10^{10}\,\text{cm}^{-2}$, no well defined steps can be made out. Another significant point is that when steps are observed, for instance Fig. A.3(c),(d), the absorption energy within each "plateau" has a strong dependence on p, shifting monotonically to the blue.
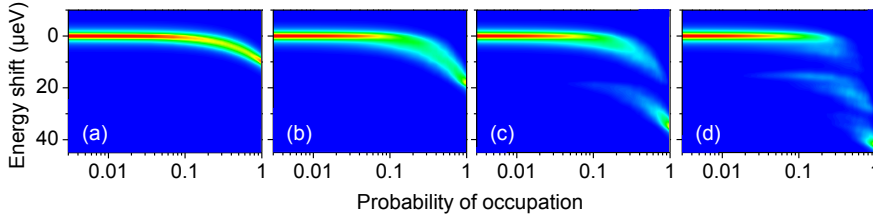
Fig. A.3. (a)-(d) Example simulations obtained with a 2D random distribution of defects with $N_{2D} = 10^{10}\,\text{cm}^{-2}$ over a surface of $1.0\,\mu\text{m}^2$. The parameters are the ones obtained for the QD in sample A in section A.1 with $N = 2,500$ and $\Gamma_L = 1.0\,\mu\text{m}$. The colour scale goes from 2 (blue) to 60 (red). More than 50% of the simulated contour plots are similar to (a) and (b); some show steps, (c) and (d).

These results are now compared with the experiments. All 8 quantum dots measured with $d_{\text{cap}} = 30\,\text{nm}$ exhibit steps of the absorption versus non-resonant laser power (P). Example data are shown in Fig. 2.2(a) (sample A), and Fig. A.4(a) (sample B). All dots have at least 3 steps. One dot shows 6 steps with a total Stark shift of $\sim 300\,\mu\text{eV}$, a situation we have not encountered even in several thousand simulations using a homogeneous N_{2D}. The conclusion is that there are localization centres located

directly above the quantum dot which are highly unlikely to arise by a process which is completely random as a function of (x, y). Instead, the quantum dot induces localization centres at the capping layer/SPS interface for $d_{cap} = 30\,\text{nm}$, typically two to four, the "above-dot-defects". Occupation of these defects leads to the pronounced steps in the Stark shift versus P experimental results, equivalently the Stark shift versus p simulations.

For the QD in sample A, the P-dependence of each Stark shift "plateau" is small, Fig. 2.3(a). As explained above, this signifies that N_{2D} is small. In fact, N_{2D} is too small for us to resolve and we take $N_{2D} = 0$ in the simulations, Fig. 2.3(b) and Fig. A.4(b). However, QDs in sample B behave differently, Fig. A.4(a). In this case, the plateau steps show a blue shift, particularly when the defects directly above the quantum dot (4 in this case), are occupied (by $3-4$ holes in this case). In addition, each absorption line in the experiment changes from run to run, the origin of the noise in Fig. A.4(a). Neither the blue shifts nor the noise can be reproduced in the simulations with $N_{2D} = 0$ as shown in Fig. A.4(b). Instead, $N_{2D} \neq 0$. For a given occupation of the defects directly above the dot, as p increases, the number of stored holes at the capping layer/SPS interface increases, inducing the blue shifts of the plateau. Also, for fixed p, changes in the charge distribution of the holes leads to small energy shifts even when the number of holes in the above-dot-defects remains constant, leading to the noise. For a quantum dot in sample B, we fix the positions of the above-dot-defects using the procedure outlined below, we define a random 2D array for $r \geq 80\,\text{nm}$, and then vary
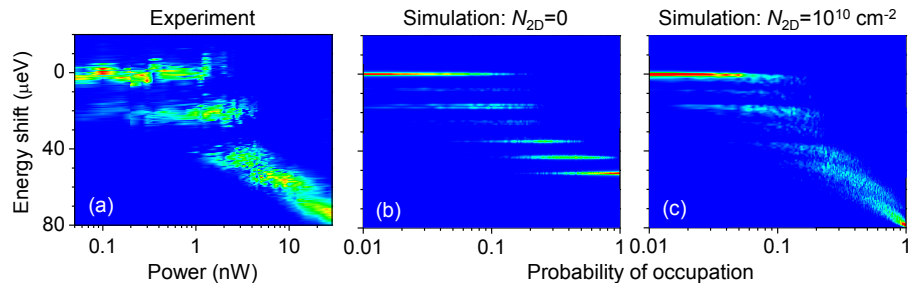
Fig. A.4. (a) Contour plot of the QD resonance fluorescence signal from sample B as a function of the non-resonant excitation power. The colour scale goes from 27 counts (blue) to 700 counts (red). (b),(c) Simulated signal as a function of the probability of occupation, plotted with the same scale dynamic as (a), i.e. 0.15 (blue) to 4 (red). (b) $N_{2D} = 0$; (c) $N_{2D} = 1.0 \times 10^{10}\,\text{cm}^{-2}$. An area of $3 \times 3\,\mu\text{m}^2$ is considered; $\Gamma_L = 10.0\,\mu\text{m}$, $N = 60$ and $\Gamma = 0.8\,\mu\text{eV}$. From the PL characterization, $V_g = -0.7\,\text{V}$, $V_0 = 0.62\,\text{V}$, $D = 322\,\text{nm}$, $p_z = 0.142\,\text{nm}$, $\beta_z = -0.104\,\mu\text{eV}/(\text{kV/cm})^2$, $\Delta F_{NR} = 13\,\text{kV/cm}$, $l_e = 5.02\,\text{nm}$ and $l_h = 2.88\,\text{nm}$. In addition to N_{2D}, 4 defects were placed by hand to reproduce the energy steps, with in-plane positions $r_i = (28, 45, 45, 26)\,\text{nm}$ and $\alpha = (4.0, 1.7, 1.0, 4.0)$.

N_{2D} to find the best fit to the experimental data: $N_{2D} = 1 \times 10^{10}\,\mathrm{cm}^{-2}$ gives good agreement with the experimental results, Fig. A.4(c).

A.2.2 Positions of above-dot-defects

We illustrate how the simulation allows us to deduce the position of the above-dot-defects, concentrating on the results from sample A, Fig. 2.2(a). (Fig. A.4 shows the result of the same procedure on a dot from sample B.) Fig. A.5 shows different contour plots obtained by changing the properties of the above-dot-defects, illustrating the procedure for reaching the best fit for the QD of sample A, Fig. 2.2(b). The number of steps, 4 in this case, determines the total number of holes which can be stored in the above-dot-defects. In Fig. A.5(a), 4 defects are placed at the same location, all with the same weight $\alpha = 1$, laterally displaced from the quantum dot in order to reproduce the total Stark shift in the experiment. Four steps and 5 transitions are simulated, as in the experiment. The "size" of the steps decreases slightly with increasing hole number – the in-plane Stark shift increases in magnitude and subtracts from the vertical Stark shift – but this does not match the experimental result, Fig. 2.2. In Fig. A.5(b), the defects are now placed one in each quadrant around the QD, keeping $r = \sqrt{x^2 + y^2}$ constant.
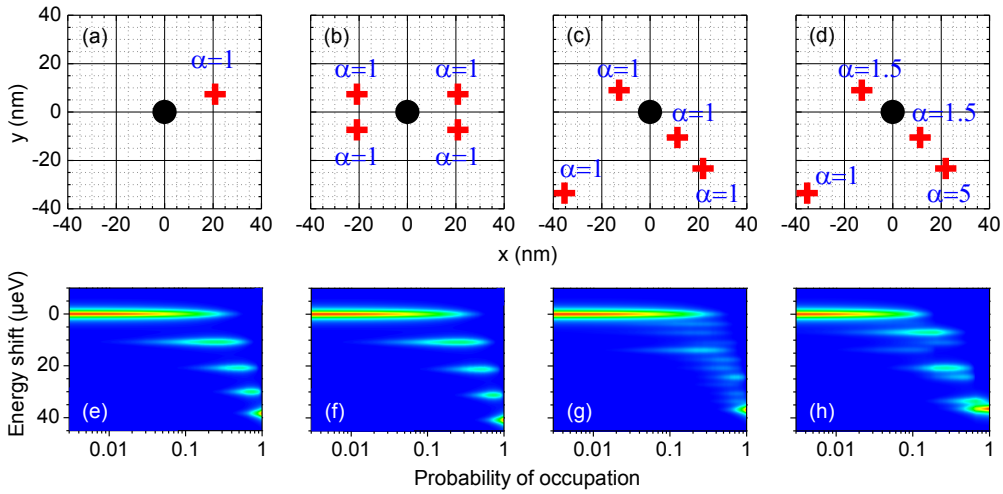
Fig. A.5. (a)-(d) 2D representation of the spatial distribution of defects used in the simulations (e)-(h). The QD is symbolized by the black point in the centre of each 2D map. In (a), all the 4 defects are located at the same place with $r = 22.1\,\mathrm{nm}$. In (b), r is kept constant, only θ is changed. In (c) and (d), the spatial distribution is the one used in chapter 2. The weight α associated to each defect is specified explicitly. The colour scale goes from 4 (blue) to 135 (red). $N_{2D} = 0$. The parameters used for the simulations are those for the QD in sample A, described in section I, with $N = 2,500$ and $\Gamma_L = 1.0\,\mu\mathrm{m}$.

Now, the step sizes are constant – the in-plane electric fields tend to cancel – in slightly better but still poor agreement with the experimental result. The significant different step sizes in the experiment can be reproduced in the simulation only by changing both the locations of the defects r_i and their relative weights α_i. In Fig. A.5(c), the 4 defects are located at 4 different values of r. The Stark shift versus p plot is now more complicated. For instance, while 2 stored holes in Fig. A.5(b) give the same Stark shift independent of the configuration, this is no longer the case in Fig. A.5(c): the 4-fold degeneracy is lifted. Line cuts show that Fig. A.5(c) has transitions at the correct energies but the relative transition strengths are not reproduced. This discrepancy is remedied by changing the α_i. The result of this procedure is shown in Fig. A.5(h). A defect with relatively large r has a particularly large α: this produces a small first step. Once this defect is always occupied, $p > 0.2$, occupation of the remaining 3 gives the remaining step structure in close agreement with the experiment.

A.2.3 Spatial resolution of the defect positions

A quantitative agreement with the peak positions and relative amplitudes in the experiment, Fig. 2.2, can only be achieved with a tolerance of $\pm 5\,\mathrm{nm}$ in each of the r_i values. This spatial resolution is illustrated in Fig. A.6, where we move, from the ideal distribution, the different defects within $5\,\mathrm{nm}$ and examine the peak positions in both the experiments and simulations, Fig. A.6, for a particular value of P, equivalently p. Fig. A.6(a),(g) represent the best fit to the data. Fig. A.6(b),(h) show results for a distribution where all the defects have been moved $5\,\mathrm{nm}$ towards the QD. The two main peaks in the simulations are now blue shifted with respect to the experiment at this particular p; also, the simulated Stark shift at $p = 1$ is also too large. Fig. A.6(c),(e) and (i),(k) show results when only one of the defects is moved by plus or minus $5\,\mathrm{nm}$. One can see that there is always at least one energy peak which is not reproduced, as indicated by the green arrows in Fig. A.6. Finally, Fig. A.6(f),(l) show results where 2 defects have been moved, one $5\,\mathrm{nm}$ towards the QD, the other $5\,\mathrm{nm}$ away, and in this case the "final" peak in the simulation has a slightly too large blue shift. It is therefore fair to claim that the random error in the r_i is around $\pm 5\,\mathrm{nm}$; the systematic error is obviously harder to judge, but the agreement in Fig. 2.2, also Fig. A.4, would suggest that it is small.
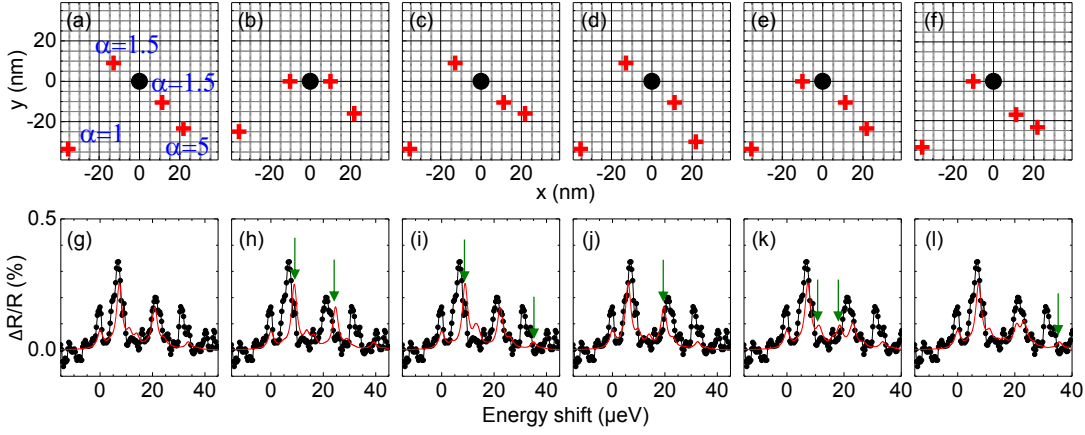
Fig. A.6. (a)-(f) 2D representation of the spatial distribution of the above-dot-defects used in the corresponding simulations, (g)-(l). The relative probability α_i for each defect i is stated in (a) and remains the same for all the other configurations. (g)-(l) Line cuts from experiment (black points/lines) at $P = 0.34$ nW and simulation (red lines) at $p = 0.16$. The parameters used in the simulations are those obtained in section I and we take $N = 2,500$ and $\Gamma_L = 1.0\,\mu$m. The distribution in (a) gives the best fit to the data and is used in chapter 2: all the simulated peaks lie within the linewidth of the corresponding peak in the experimental data. In (b), all the defects are moved 5 nm towards the QD. In (c), the defect with $\alpha = 5$ is moved 5 nm towards the QD. In (d), the defect with $\alpha = 5$ is moved 5 nm away from the QD. In (e), the defect with $x < 0$ and $\alpha = 1.5$ is moved 5 nm towards the QD. Finally, in (f), the defect with $x < 0$ and $\alpha = 1.5$ is moved 5 nm towards the QD while the defect with $x > 0$ and $\alpha = 1.5$ is moved 5 nm away from the QD. In each case, (h)-(l), at least one of the simulated peaks is shifted by at least a linewidth from the peak in the experiment. The particular peaks in question are shown by the green arrows.

References

1. Warburton, R. J., Schulhauser, C., Haft, D., Schäflein, C., Karrai, K., Garcia, J. M., Schoenfeld, W., and Petroff, P. M. *Phys. Rev. B* **65**, 113303 (2002).

2. Gerardot, B. D., Seidl, S., Dalgarno, P. A., Warburton, R. J., Granados, D., Garcia, J. M., Kowalik, K., Krebs, O., Karrai, K., Badolato, A., and Petroff, P. M. *Appl. Phys. Lett.* **90**, 041101 (2007).

3. Warburton, R. J., Miller, B. T., Dürr, C. S., Bödefeld, C., Karrai, K., Kotthaus, J. P., Medeiros-Ribeiro, G., Petroff, P. M., and Huant, S. *Phys. Rev. B* **58**, 16221–16231 (1998).

4. Dalgarno, P. A., Smith, J. M., McFarlane, J., Gerardot, B. D., Karrai, K., Badolato, A., Petroff, P. M., and Warburton, R. J. *Phys. Rev. B* **77**, 245311 (2008).

Appendix B

Supplementary information to chapter 3 "Charge noise and spin noise in a semiconductor"

In chapter 3 "Charge noise and spin noise in a semiconductor quantum device", the resonance fluorescence (RF) from a single quantum dot (QD) is used to investigate noise inherent to the semiconductor: charge noise and spin noise. We distinguish between charge noise and spin noise via a crucial difference in their optical signatures. We derive noise spectra for both electric and magnetic fields with Monte-Carlo simulations. The noise decreases with increasing frequency, such that, by operating the device at high enough frequencies, we demonstrate the transform-limit for the QD optical linewidth. Here, we explain the details of the experiments, the data processing and the modelling.

B.1 Resonance fluorescence on a single quantum dot

B.1.1 The semiconductor quantum device

The quantum device that is used to probe charge noise and spin noise in a semiconductor is a QD sample grown by molecular beam epitaxy. The data presented in chapter 3 were measured on two QDs from different samples: QD1 from sample A and QD2 from sample B. In addition, data are shown from QD3 from sample B and QD4 from sample C in this supplementary information.

The self-assembled QDs are embedded in a Schottky diode[1,2] as shown in Fig. B.1(a). The layer sequence is:

1. *back contact*
   50 nm n^+-GaAs, doping level $\sim 1.7 \times 10^{18}$ cm^{-3}

2. *tunnelling barrier*
   25 nm i-GaAs

3. *active layer*
   InGaAs QDs (diameter ~ 20 nm, height ~ 5 nm) with centre wavelength 950 nm.

4. *capping layer*
   samples A and B: 150 nm i-GaAs
   sample C: 434.3 nm i-GaAs

5. *blocking barrier*
   samples A and B: 68 periods AlAs/GaAs 3 nm/1 nm
   sample C: 64 periods AlAs/GaAs 3 nm/1 nm

6. *cap*
   10 nm i-GaAs

7. *Schottky gate*
   samples A and C: 3 nm/7 nm Ti/Au
   sample B: 5 nm/10 nm Ti/Au.

Samples A and B only differ in the gate thickness, they are from the same wafer. Sample C is from a different wafer grown under similar conditions with increased capping layer thickness. Our previous spectroscopic experiments[3] showing clear single charging events from holes trapped at the capping layer/blocking barrier interface were carried out on a sample from the same growth system but with 30 nm capping layer thickness.
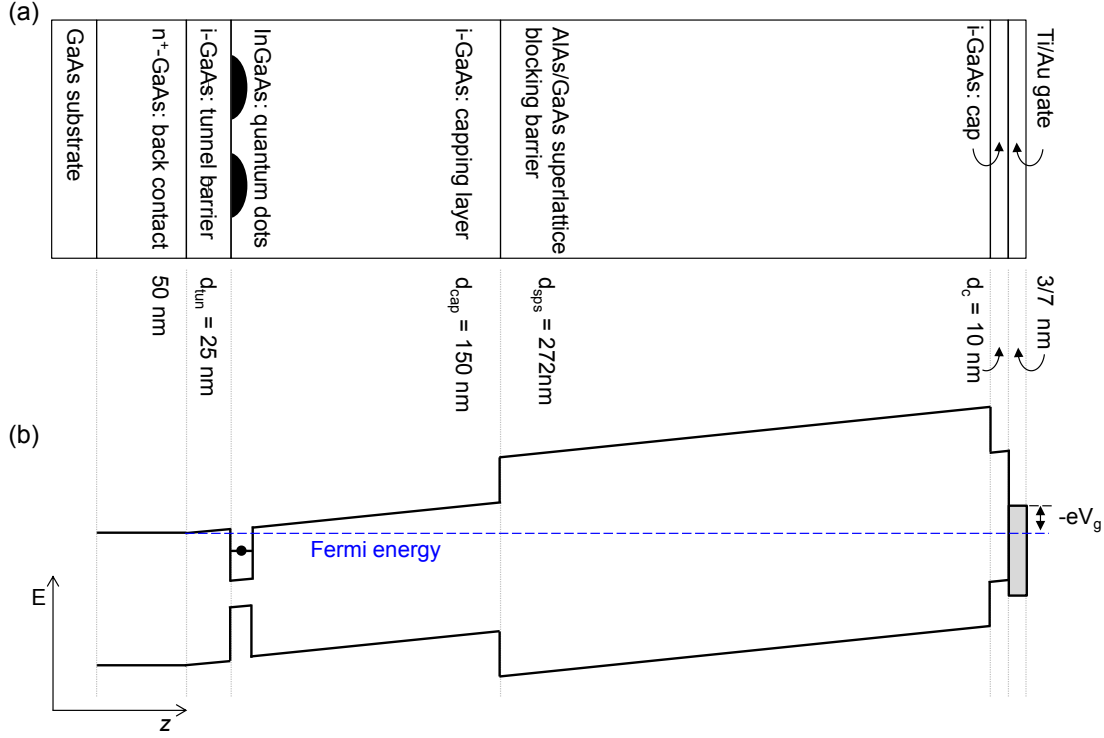
Fig. B.1. (a) Structure of sample A and the corresponding (b) Energy band diagram. The Fermi energy is pinned to the conduction band edge of the back contact. The figures are to scale with respect to length.

The background doping of as-grown GaAs is $p \sim 10^{13} \, \text{cm}^{-3}$; two-dimensional electron gases grown under similar conditions have mobilities $> 10^6 \, \text{cm}^2/\text{Vs}$.

The number of carriers confined to the QD can be precisely controlled by the gate voltage V_g as illustrated in Fig. B.1(b). A change of gate voltage yields a change of the QD's local potential ϕ by

$$\Delta\phi = \frac{\Delta V_g}{\lambda} \tag{B.1}$$

where λ denotes the sample's lever arm, defined as the ratio of back contact to gate distance d and tunnel barrier thickness. For samples A and B $\lambda = 18.3$, for sample C $\lambda = 29.0$, respectively. The exciton energy E is detuned with respect to the constant laser frequency by exploiting the dc Stark effect,

$$\Delta E = a\Delta F, \quad \Delta F = \frac{\Delta V_g}{d} \tag{B.2}$$

with Stark shift coefficient a and electric field F. The Stark shift is determined by recording the resonance position in V_g for many laser frequencies, the laser frequency

Stark shift a (μeVcm/V)	QD1	QD2	QD3	QD4
X^0	0.0324	0.0320	0.0306	0.0377
X^{1-}	0.0240	0.0266	0.0219	0.0296

Table B.1. Stark shift coefficient of neutral exciton and trion.

measured in each case with an ultra-precise wavemeter. The Stark shift is linear in ΔF for the small windows of V_g used here, Fig. B.5(b). The neutral exciton X^0 has a larger Stark shift than the trion X^{1-} and thus it is more sensitive to charge noise, Table B.1.

B.1.2 Resonance fluorescence

The quantum dot optical resonance is driven with a resonant continuous-wave laser (1 MHz linewidth) focused on to the sample surface. Reflected or scattered laser light is rejected with a dark field technique using crossed linear polarizations for excitation and detection (see chapter 1). The axes of linear polarization are aligned to the sample's crystal axes. The polarization of the neutral exciton is nearly parallel to the crystal axes for QD1, and rotated by $\sim \pi/4$ for QD2, QD3 and QD4. Consequently, at zero magnetic field only the higher energy X^0 transition (blue transition) of QD1 is observed in resonance fluorescence (RF), whereas both lower (red transition) and higher energy transitions are observed for the other QDs. The transitions to the trion states are circularly polarized.

The laser power is chosen to lie below the point at which power broadening can be observed, Table B.2. Resonance fluorescence is detected with a silicon avalanche photodiode in photon counting mode. The arrival time of each photon is recorded over the entire measurement time T.

The experiment is not shielded against the earth's magnetic field, thus $B_{\min} \sim 50\,\mu$T. All the experiments were performed with the sample at 4.2 K.

noise measurement	Fig. 2 (a)	Fig. 2 (b)	Fig. 4 (a)
exciton	X^{1-}	X^{1-}	X^0
Ω/Γ_0	0.73	0.84	0.74
Γ_0 (μeV)	0.75	0.74	0.93

Table B.2. Laser power. The Rabi frequency Ω is stated as a multiple of the transform-limit Γ_0 for all the noise measurements presented in the main article. Γ_0 is given with an error of $\pm 0.1\,\mu$eV.

B.2 Charge noise and spin noise: experiments

B.2.1 Determination of quantum dot noise spectrum

Post measurement, a binning time t_{bin} is selected, typically $1\,\mu\text{s}$. The number of counts in each time bin is $S(t)$, the average number of counts per bin $\langle S(t) \rangle$. The fast Fourier transform of the normalized RF signal $S(t)/\langle S(t) \rangle$ is calculated to yield a spectrum of the noise power $N_{\text{RF}}(f)$, specifically

$$N_{\text{RF}}(f) = |\text{FFT}\left[S(t)/\langle S(t)\rangle\right]|^2 \, (t_{\text{bin}})^2/T. \tag{B.3}$$

$N_{\text{RF}}(f)$ has the same spectrum independent of the choice of t_{bin} and T: smaller values of t_{bin} allow $N_{\text{RF}}(f)$ to be determined to higher values of frequency f; larger values of T allow $N_{\text{RF}}(f)$ to be determined with higher resolution. The high frequency limit of our experiment is only limited by the photon flux. The typical binning time of $1\,\mu\text{s}$ is not the smallest possible. Smaller values of t_{bin} will however increase the Fourier transform computation time.

All Fourier transforms are normalized[4] such that the integral of the noise power $N_x(f)$ over all positive frequencies equals the variance of the fluctuations δx,

$$\langle(\delta x)^2\rangle = \int_0^\infty df\, N_x(f). \tag{B.4}$$

To record a noise spectrum of the experiment alone, the QD is detuned by > 100 linewidths relative to the laser and one polarizer is rotated by a small angle to open slightly the detection channel for reflected laser light, choosing the rotation so that the detected laser light gives a count rate similar to the QD RF. A noise spectrum of the reflected laser light (Fig. B.2(a)) is recorded using exactly the routine used to analyse the RF, yielding $N_{\text{exp}}(f)$. $N_{\text{exp}}(f)$ has a $1/f^2$-behaviour at low frequencies arising from intensity fluctuations in the setup. For $f > 10$ Hz, $N_{\text{exp}}(f)$ has a completely f-independent spectrum, $N_{\text{exp}} \sim 10^{-5}\ \text{Hz}^{-1}$: this is the shot noise N_{shot}. The noise of the experiment is typically larger than the noise of the QD $N_{\text{QD}}(f)$. The shot noise is proportional to $\langle S(t)\rangle^{-1}$ (Fig. B.2(b)) and not to $\langle S(t)\rangle^{1/2}$ due to the normalization of $S(t)$ by $\langle S(t)\rangle$ in the calculation of the spectrum. N_{shot} is comparable to $N_{\text{QD}}(f)$ at low frequencies ($f \sim 10$ Hz), and exceeds $N_{\text{QD}}(f)$ at higher frequencies, Fig. B.2(c).

The noise spectrum of the QD alone is then determined using

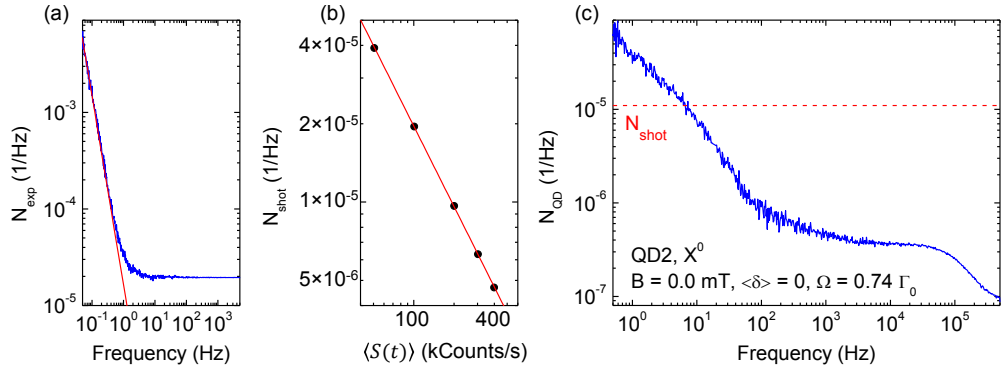$$N_{\text{QD}}(f) = N_{\text{RF}}(f) - N_{\text{exp}}(f). \tag{B.5}$$

Fig. B.2. (a) Noise spectrum of the experiment. Intensity fluctuations of the laser cause a $1/f^2$-behaviour of $N_{\mathrm{exp}}(f)$ at low frequencies (exponent of red fit -1.96). For $f > 10$ Hz the spectrum is dominated by shot noise, thus, the spectrum is flat. The average count rate of the detected laser light is 101 kCounts/s in this particular experiment. (b) Shot noise. Noise spectra of the experiment alone were recorded at different laser light count rates to extract the dependence of the shot noise on the count rate. A proportionality of the shot noise to $\langle S(t) \rangle^{-1}$ is verified (exponent of red fit -1.03). (c) Quantum dot noise spectrum. The noise of the experiment is typically larger than the noise of the QD. The shot noise (red dashed line) typically equals $N_{\mathrm{QD}}(f)$ at low frequencies ($f \sim 10$ Hz), and exceeds $N_{\mathrm{QD}}(f)$ at higher frequencies. The RF count rate is 176 kCounts/s in this particular experiment. The noise spectrum shown here is the one from Fig. 3.5(a) of chapter 3.

Correction of $N_{\mathrm{RF}}(f)$ with $N_{\mathrm{exp}}(f)$ where $N_{\mathrm{RF}}(f)$ and $N_{\mathrm{exp}}(f)$ are not measured simultaneously is successful on account of the high stability of the setup. Furthermore, no spectral resonances in $N_{\mathrm{QD}}(f)$ have been discovered. We present here $N_{\mathrm{QD}}(f)$ after averaging at each f over a frequency range Δf to yield equidistant data points on a logarithmic scale. This entire procedure enables us to discern $N_{\mathrm{QD}}(f)$ down to values of 10^{-8} Hz^{-1} for $T = 2$ hours.

B.2.2 Quantum dot noise

Quantum dot-to-Quantum dot dependence

Noise spectra of three different QDs from the same wafer with 150 nm capping layer – QD1, QD2 and QD3 – are shown in Fig. B.3(a) for the neutral exciton X^0 and Fig. B.3(b) for the trion X^{1-}, respectively. The X^0 noise spectrum of QD2 is presented in Fig. 3.5(a) of chapter 3, the X^{1-} noise spectrum of QD2 in Fig. 3.2 of chapter 3 and the X^{1-} noise spectrum of QD1 in Fig.s 3.6 and 3.7 (c) of chapter 3.

For all QDs we find that charge noise is concentrated at low frequencies and that spin noise lies at higher frequencies. For both charge noise and spin noise the quantum dot-to-quantum dot variation of the correlation times is small.
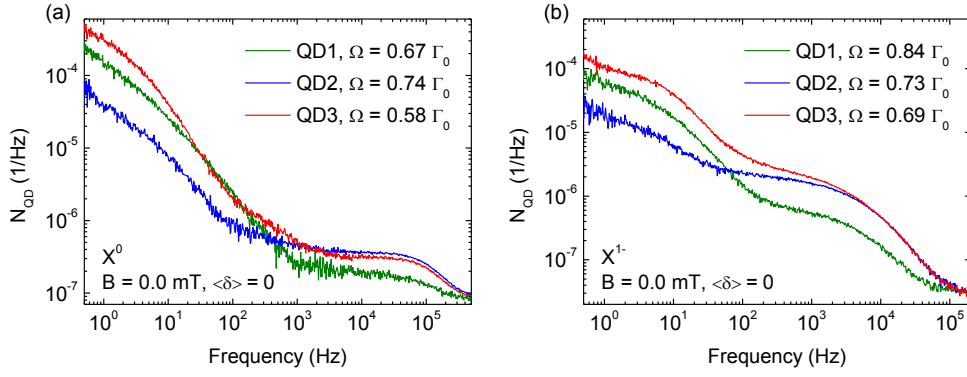
Fig. B.3. Noise spectra of different QDs: neutral exciton X^0 (a) and trion X^{1-} (b). Noise spectra of three different QDs were recorded for both the X^0 and X^{1-}. The laser power of each measurement is given by the ratio of Rabi energy Ω to radiative decay rate Γ_0.

The correlation time of the nuclear spin fluctuations for the neutral exciton X^0 is $5.5\,\mu s$ for all three QDs. Whereas for QD2 and QD3 the spin noise power is almost the same, QD1 is less sensitive to spin noise, pointing to a smaller electron g-factor.

The general behaviour of the charge noise is the same for all QDs, but the charge noise powers are quantum dot dependent. The neutral exciton X^0 is more sensitive to charge noise than the trion X^{1-}, reflecting the larger Stark shift. In general, the difference in the charge noise power is due either to the different local electrical environment the QD senses or to a difference in sensitivity, on account of the different Stark shifts. QD3 for instance has the smallest Stark shift of all three QDs, Table B.1, but the largest noise power, i.e. the local electrical environment of QD3 is the noisiest one.

Magnetic field dependence

In Fig. 3.2 of chapter 3 we present noise spectra of the X^{1-} taken with two detunings, one with average detuning $\langle\delta\rangle = 0$, the other with average detuning half a linewidth, $\langle\delta\rangle = \Gamma/2$. Switching from $\langle\delta\rangle = 0$ to $\langle\delta\rangle = \Gamma/2$ causes the low frequency noise to increase yet the high frequency noise to decrease. This crucial information allows us to distinguish charge noise and spin noise. Sensitivity to charge noise is weak for $\langle\delta\rangle = 0$ yet strong for $\langle\delta\rangle = \Gamma/2$. Spin noise results in a complementary behaviour in the absence of an external magnetic field, $B = 0$.

The identification of charge noise and spin noise can be backed up by experiments in small external magnetic fields. In the presence of an external magnetic field, $B \neq 0$, the trion resonance is split by the exciton Zeeman energy E_Z. The splitting at low magnetic fields of a few tens of mT is of the order of the linewidth. Resonance fluorescence spectra
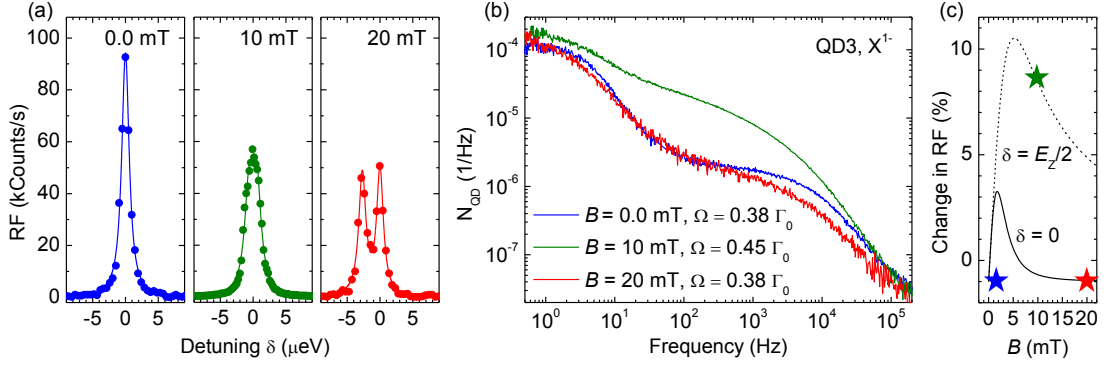
Fig. B.4. (a) RF spectra of the X^{1-} in the presence of a magnetic field. The trion resonance is split by the exciton Zeeman energy E_Z, the splitting is resolved for $B > 10\,\text{mT}$. (b) Charge noise and spin noise in the presence of a magnetic field. The corresponding noise measurements. (c) Simulation of the X^{1-} spin noise sensitivity. The change in RF for an Overhauser field shift $\Delta\delta = 0.13\,\Gamma_0$, the spin noise sensitivity, is shown for $\langle\delta\rangle = 0$ (solid line) and for $\langle\delta\rangle = E_Z/2$ (dashed line). First the trion's response increases, it then returns to the zero field value remaining constant at higher fields. The colours are used to indicate the same magnetic field, the stars mark the expected value of spin noise sensitivity for the particular measurement.

taken at zero magnetic field and at low fields are shown in Fig. B.4(a). The exciton Zeeman splitting is resolved for $B > 10\,\text{mT}$.

In a small magnetic field we expect charge noise to stay the same yet the trion's response to spin noise first to increase and then to decrease again. Noise spectra of the X^{1-} recorded in a small magnetic field are shown in Fig. B.4(b). Charge noise is unaffected yet spin noise is increased by an order of magnitude at $B = 10\,\text{mT}$ (measured with $\langle\delta\rangle = -E_Z/2$ with respect to the higher energy transition) and returns to the zero field value at $B = 20\,\text{mT}$ (measured with $\langle\delta\rangle = 0$ with respect to the higher energy transition), confirming the expectations on the trion's response to spin noise, Fig. B.4(c).

The external magnetic field affects the nuclear spin dynamics. The higher the field the slower the nuclear spins are. This is already observed for B as small as $20\,\text{mT}$, where the spin noise is shifted to lower frequencies, Fig. B.4(b).

B.2.3 Determination of quantum dot linewidth

In Fig. 3.4 of chapter 3 the linewidth of the blue transition of the neutral exciton X^0 of QD2 is discussed. In addition, we present in Fig. B.5 a discussion of the red X^0 and the X^{1-} transition of the same QD.

To determine the quantum dot optical linewidth Γ, we apply a triangle voltage signal to the gate with 100 mV amplitude, recording the RF signal as a function of time, Fig.
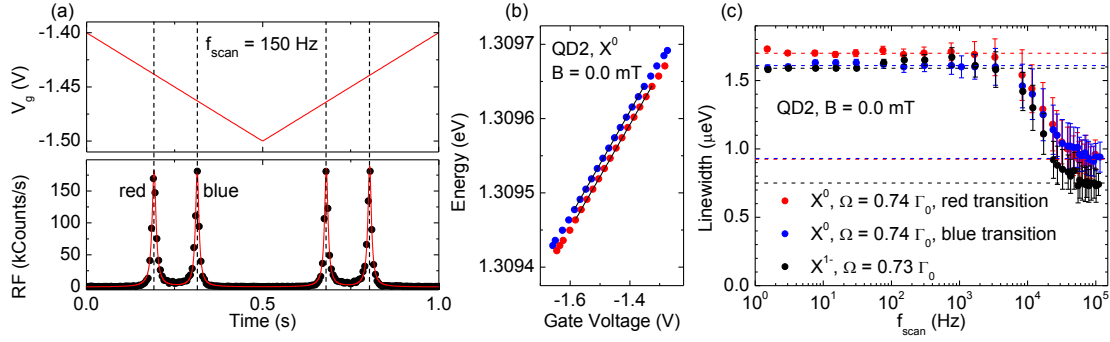
Fig. B.5. (a) Gate voltage and RF time trace. A triangle voltage signal with 100 mV amplitude and 1 Hz frequency, corresponding to 150 Hz scan frequency, is applied to the gate. The constant laser frequency is set in resonance with the neutral exciton X^0. Due to the fine structure splitting of the X^0, $\Delta = 17.3\,\mu$eV for QD2, two peaks per scan are observed in the RF even at zero magnetic field. Sweeping to more negative voltages first the lower energy resonance (red) is observed. (b) Stark shift. To determine the Stark shift the resonance position in gate voltage is recorded as the laser frequency is varied. The Stark shift for both red and blue X^0 transitions is $0.032 \pm 0.005\,\mu$eVcm/mV. Solid black lines are linear fits to the data. (c) Linewidth dependence on scan frequency. The linewidth for both red and blue transitions of the neutral exciton is recorded as the scan frequency is varied. The constant laser frequency corresponds to the centre of the gate voltage plateau shown in (b). As the scan frequency increases the linewidth decreases from 1.70 μeV for the red transition and 1.61 μeV for the blue transition (upper dashed lines) to 0.93 μeV (lower dashed line) and remains constant at higher frequencies. The radiative lifetime is 0.70 ± 0.05 ns ($\Gamma_0 = 0.94 \pm 0.07$ μeV), thus the transform-limit is achieved. The experiment is repeated with the constant laser frequency set in resonance with the X^{1-}. The linewidth decreases from 1.59 μeV to 0.75 μeV corresponding to the trion's transform-limit of $\Gamma_0 = 0.77 \pm 0.05$ μeV. The mean value of typically 100 Lorentzian fits is plotted as a function of scan frequency; error bars indicate the standard deviation.

B.5(a). Each time the quantum dot comes into resonance with the constant frequency laser, a peak in the RF is observed. The peak is fitted to a Lorentzian, and the linewidth in mV is converted to a linewidth in μeV using the known Stark shift.

The linewidth is recorded as the scan frequency is varied, Fig. B.5(c). The scan frequency is defined as the scanning rate divided by the transform-limited linewidth, $f_{\text{scan}} = d\delta/dt/\Gamma_0$ with $\Gamma_0 = \hbar/\tau_r$. For each scan frequency, multiple resonances are recorded and the mean linewidth with error given by standard deviation is plotted as a function of the scan frequency, Fig. B.5(c).

As the scan frequency is increased the linewidth decreases and remains constant at higher frequencies. This constant value corresponds to the transform-limit, determined separately by measuring the exciton lifetime. The radiative lifetime, τ_r, is measured either from an intensity correlation measurement, $g^{(2)}(t)$, or from a decay curve following

pulsed excitation.

B.3 Charge noise and spin noise: modelling

The experiment determines the spectrum of the noise in the RF and demonstrates that it is dominated by charge noise at low frequency, spin noise at high frequency. The noise sensor, the RF from a single quantum dot, has a trivial dependence on the fluctuating electric $F(t)$ and magnetic fields $B_N(t)$ only for small fluctuations in the detunings around particular values of detuning δ. Monte Carlo simulations allow us to determine both the electric field and magnetic field noise accurately by describing the response of the sensor for all δ, treating charge noise and spin noise on an equal footing.

The basic approach is to calculate $F(t)$ and $B_N(t)$, in each case from an ensemble of independent, but identical, 2-level fluctuators using a Monte Carlo method; to calculate the RF signal $S(t)$ from $F(t)$ and $B_N(t)$; and to compute the noise $N(f)$ from $S(t)$ using exactly the same routine as for the experiments (but without the correction for extrinsic noise of course).

For X^{1-},

$$S(t) = \frac{\frac{1}{2}\left(\frac{\Gamma_0}{2}\right)^2}{(aF(t) + \delta_1(t) + \delta)^2 + \left(\frac{\Gamma_0}{2}\right)^2} + \frac{\frac{1}{2}\left(\frac{\Gamma_0}{2}\right)^2}{(aF(t) - \delta_1(t) + \delta)^2 + \left(\frac{\Gamma_0}{2}\right)^2}, \quad \delta_1(t) = \frac{1}{2}g\mu_B B_N(t),$$

(B.6)

where a is the dc Stark coefficient and g the electron g-factor.

For X^0,

$$S(t) = \frac{\left(\frac{\Gamma_0}{2}\right)^2}{(aF(t) + \delta_0(t) + \delta)^2 + \left(\frac{\Gamma_0}{2}\right)^2}, \quad \delta_0(t) = \pm\frac{1}{2}\sqrt{\Delta^2 + \delta_1(t)^2},$$

(B.7)

with Δ the fine structure splitting. For the blue Zeeman branch $\delta_0(t)$ is positive, for the red one negative, respectively.

An ensemble of identical 2-level fluctuators fully describes spin noise; charge noise is more complex, Fig. B.6. The experiment reveals the existence of a dominant 2-level fluctuator that is modelled using a Monte Carlo approach. To fully describe charge noise, post simulation a weak $1/f$-like noise component is introduced.

B.3.1 Spectrum of a 2-level fluctuator

A 2-level fluctuator occupies either state 0 with lifetime τ_0 or state 1 with lifetime τ_1. The probability p of being, at any time, in state 1 is $\tau_1/(\tau_0 + \tau_1)$; the probability of
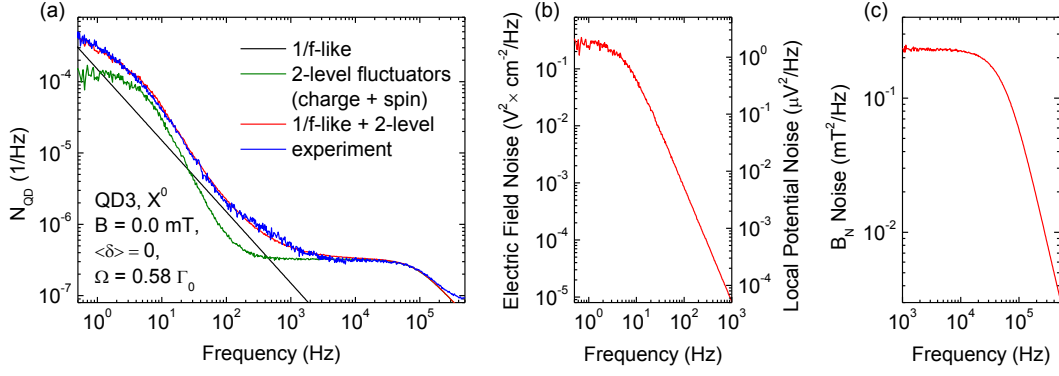
Fig. B.6. Charge noise and spin noise modelling. Charge noise and spin noise of the neutral exciton X^0 of QD3 are calculated from an ensemble of 2-level fluctuators. To fully describe charge noise a $1/f^\alpha$ noise component with $\alpha = 1.00$ is added to $N_{\text{QD}}(f)$. From the simulations both the electric (without the $1/f$-like noise) and magnetic field noise can be calculated. The rms value for the fluctuations in the local potential is $3.9\,\mu\text{V}$ corresponding to electric field fluctuations of $1.55\,\text{V/cm}$ with a correlation time of $0.03\,\text{s}$. The nuclear spins cause fluctuations of $B_{N,\text{rms}} = 145\,\text{mT}$ with a correlation time of $5.5\,\mu\text{s}$. The parameters used in the simulations are: $N_c = 1.0 \times 10^{10}\,\text{cm}^{-2}$, $d = 150\,\text{nm}$ and $p = 1.2\%$ for charge noise; $N_{\text{eff}} = 115$, $A = 90\,\mu\text{eV}$, $g = -0.5$ and $\Delta = 11.5\,\mu\text{eV}$ for spin noise.

being in state 0 is $\tau_0/(\tau_0 + \tau_1)$. The configuration $C(t)$ of a 2-level fluctuator, either 0 or 1, is determined by the probabilities of a $0 \to 1$ transition[5],

$$p_{0\to1}(\delta t) = 1 - \frac{1}{\tau_0 + \tau_1}\left[\tau_1 \exp\left(-\left(\frac{1}{\tau_0} + \frac{1}{\tau_1}\right)\delta t\right) + \tau_0\right] \tag{B.8}$$

and a $1 \to 0$ transition,

$$p_{1\to0}(\delta t) = 1 - \frac{1}{\tau_0 + \tau_1}\left[\tau_0 \exp\left(-\left(\frac{1}{\tau_0} + \frac{1}{\tau_1}\right)\delta t\right) + \tau_1\right] \tag{B.9}$$

where δt denotes the time over which the system evolves. The power spectrum of a 2-level fluctuator $S(\omega)$ is Lorentzian[5],

$$S(\omega) = \frac{1}{\pi}\frac{\tau_0\tau_1}{(\tau_0 + \tau_1)^2}\frac{1/T}{\omega^2 + (1/T)^2}, \quad 1/T = 1/\tau_0 + 1/\tau_1. \tag{B.10}$$

B.3.2 Charge noise

The experiment reveals the low frequency noise to be charge noise. There is a Lorentzian power spectrum superimposed on a weak $1/f$-like component in the power spectrum, Fig. B.6.

The simulation for the Lorentzian charge noise proceeds by assuming that the noise

arises from an ensemble of localization centres, each of which can be occupied by a single hole[3]. Performing the experiments in Fig. B.5, we very occasionally observe (probability $\sim 2\%$) that the QD resonance shifts by $2.45\,\mu\mathrm{eV}$ from its average position. This is a blue-shift consistent with the trapping of a single hole above the QD. The centres are located at distance d away from the QDs. The energy shift ΔE of the exciton resonance induced by the electric field $F_{\mathrm{h},z}$ created by a single hole is given by

$$\Delta E = -aF_{\mathrm{h},z}. \tag{B.11}$$

The approximate in-plane symmetry of the QDs allows only for a significant non zero dipole moment in growth direction z. Again, as in the z-direction the exciton polarizability can be neglected such that only $F_{\mathrm{h},z}$ contributes to the Stark shift. The electric field $F_{\mathrm{h},z}$ at the position of the QD created by a single positive charge at distance d from the QD, at lateral coordinate $\mathbf{r} = (x, y)$ is given by[3]

$$F_{\mathrm{h},z} = \frac{-e}{4\pi\epsilon_0\epsilon_r} \left[\frac{d}{(r^2 + d^2)^{3/2}} + \frac{d + 2d_{\mathrm{tun}}}{\left(r^2 + (d + 2d_{\mathrm{tun}})^2\right)^{3/2}} - \frac{d + 2\left(d_{\mathrm{sps}} + d_{\mathrm{c}}\right)}{\left(r^2 + (d + 2\left(d_{\mathrm{sps}} + d_{\mathrm{c}}\right))^2\right)^{3/2}} \right]. \tag{B.12}$$

Both the hole at distance d and its negative image charges in the metallic back contact and the Schottky gate contribute to the electric field. For example, a hole at distance $d_{\mathrm{cap}} = 150\,\mathrm{nm}$, centred above the QD, shifts the resonance by $+1.65\,\mu\mathrm{eV}$; increased by a negative image charge in the back contact to $+2.57\,\mu\mathrm{eV}$; reduced by a negative image charge in the top gate to $+2.50\,\mu\mathrm{eV}$. The numbers are derived with the neutral exciton's Stark shift of QD3, Table B.1, and the close agreement with the experimental optical shift of $+2.45\,\mu\mathrm{eV}$ enables us to conclude that $d = d_{\mathrm{cap}}$, i.e. the hole in the environment is located at the capping layer/blocking barrier interface.

To back up this conclusion we measured the noise on a sample with increased capping layer thickness, Fig. B.7. For sample C the capping layer thickness was increased from $150\,\mathrm{nm}$ to $434.3\,\mathrm{nm}$ moving the capping layer/blocking barrier interface far away from the QDs. The high frequency noise is unaffected by the increased capping layer thickness, supporting the identification of the high frequency noise to be spin noise. The low frequency noise by contrast changes: the Lorentzian charge noise vanishes and a weak $1/f$-like noise component remains. This strongly supports the assertion that the Lorentzian charge noise is caused by fluctuating holes the capping layer/blocking barrier interface.

We model a two-dimensional array of localization centres. The centres have a density
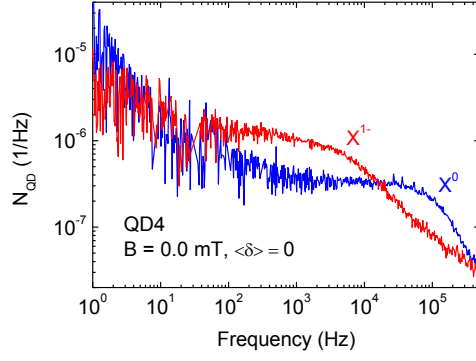
Fig. B.7. Noise dependence on capping layer thickness. Charge noise and spin noise of both the neutral exciton X^0 and the trion X^{1-} for QD4 from sample C with increased capping layer thickness compared to samples A and B.

of N_c and, at any particular time, are occupied/unoccupied (states 1/0) with probability p, $1-p$ such that the average hole density is $N_h = pN_c$. At $t = 0$, each centre is occupied by a random number generator giving a configuration of localized charges $C(0)$. At a later time, δt, $C(\delta t)$ is calculated from $C(0)$ again with a random number generator using the probabilities $p_{1\to0}(\delta t)$ and $p_{0\to1}(\delta t)$ from the theory of a two-level fluctuator. The localization centres are treated independently. The localization centres directly above the quantum dot give rise to substantial energy shifts $\Delta E \sim 2.5\,\mu\text{eV}$ which, as described above, we very rarely observe: we therefore neglect any localization centres in a circle of diameter $0.8\,\mu\text{m}$ about the quantum dot axis. In other words, above-QD localization centres exist, but are occupied with low probability. This is probably related to a strain field above the quantum dot. The procedure is repeated to give $C(0), C(\delta t), C(2\delta t)$, etc. The electric field $F(t)$ is calculated for each C.

For the Monte-Carlo simulations charge noise can be controlled by 4 independent parameters: occupation probability p, localization centre density N_c, distance d and lifetime τ_1 (for $\tau_1 < \tau_0$). Once p and τ_1 are defined, τ_0 cannot be chosen independently: τ_1 is determined by the Lorentzian's linewidth. In principle, a good fit to the experiment can be achieved in a window of N_c and d: a high density of far away defects leads to similar charge noise as a lower density of closer defects. In practice however, the occasional rigid shift of $+2.45\,\mu\text{eV}$ and the noise suppression with increased capping layer thickness point strongly to the fact that the localization centres are located at the capping layer/blocking barrier interface. We therefore simulate the Lorentzian charge noise using $d = d_{\text{cap}}$ and $N_c = 1.0 \times 10^{10}\,\text{cm}^{-2}$, a value of N_c we deduced from a sample with $d_{\text{cap}} = 30\,\text{nm}$ for which the spectral shifts on occupying the localization centres
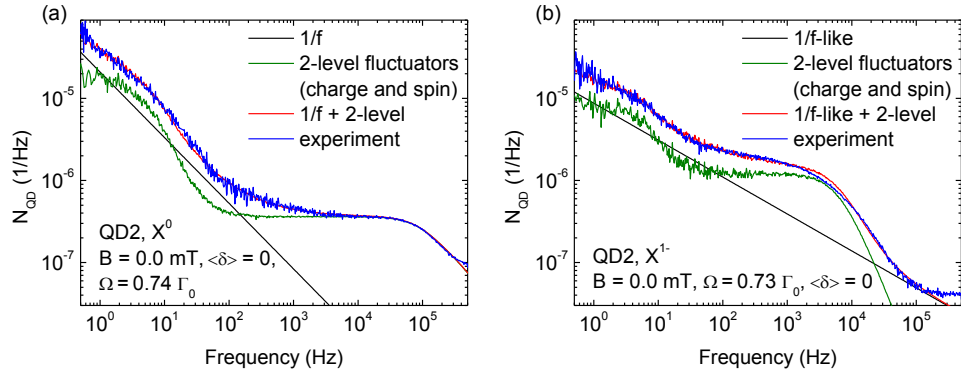
Fig. B.8. Charge noise and spin noise modelling. Charge noise and spin noise of both the neutral exciton X^0 and the trion X^{1-} of QD2 are simulated. Fig. B.7 (a) and Fig. 3.5(a) of the main article are the same.

are much larger[3].

Post simulation, in $N_{QD}(f)$ we superimpose the Lorentzian charge noise on a weak $1/f$-like noise component. The power and exponent of the $1/f$-like noise is exciton and also quantum dot dependent and its origin is not known exactly. It is however independent of the power of the resonant laser.

The results of the charge noise simulations for both the neutral exciton X^0 and the trion X^{1-} of QD2 are presented in Fig. B.8. Both excitons sense the same local electrical environment however with a different Stark shift: the neutral exciton is more sensitive to fluctuations of the electrical environment. A good fit to the experiment is achieved for both X^0 and X^{1-} by an ensemble of 2-level fluctuators with $\tau_1 = 0.03\,\mathrm{s}$, $N_c = 1.0 \times 10^{10}\,\mathrm{cm}^{-2}$ and $d = 150\,\mathrm{nm}$. The occupation probability p is $0.1\,\%$ ($\tau_0 = 30\,\mathrm{s}$) for X^0 and $0.46\,\%$ ($\tau_0 = 6.5\,\mathrm{s}$) for X^{1-}. The difference in p reflects the different charging state of the sample, discussed in section 3.6 of chapter 3. The exponent of the superimposed $1/f^\alpha$ noise in $N_{QD}(f)$ is determined by the slope of $N_{QD}(f)$ at low frequencies $f \sim 0.1\,\mathrm{Hz}$: $\alpha = 0.8$ for X^0, $\alpha = 0.5$ for X^{1-}. Note that also the charge noise of QD3 (Fig. B.6) can be described with the same local electrical environment as used for QD2.

B.3.3 Spin noise

The calculation of the time trace of the magnetic field $B_N(t)$ proceeds in a similar way, albeit simplified: each nucleus is treated as a two-level fluctuator, with equal $0 \to 1$, $1 \to 0$ transition rates, $1/\tau$. The nuclear magnetic field, the so-called Overhauser field

B_N, is given by[6]

$$B_N = \frac{v_0}{g\mu_B} \sum_{i=1}^{N} A_i \left|\psi(\mathbf{r}_i)\right|^2 I_i \tag{B.13}$$

where v_0 is the atomic volume, A_i the hyperfine interaction constant, $\mathbf{r}_i$ is the position of the nuclei i with spin I_i, and $\psi(\mathbf{r})$ is the normalized electron envelope function. By using an average hyperfine constant[7] $A = 90\,\mu\text{eV}$ and approximating the electron envelope function $\psi(\mathbf{r})$ by a top hat, Eq. (B.13) simplifies to

$$B_N = \frac{A}{g\mu_B N_{\text{eff}}} \sum_{i=1}^{N_{\text{eff}}} I_i. \tag{B.14}$$

N_{eff} denotes the number of nuclear spins inside the top hat envelope function.

Regarding the dimensionality of B_N, a 1D model for the nuclear spins is appropriate for both X^0 and X^{1-}. The isotropic part of the electron-hole exchange interaction "protects" the X^0 from the in-plane fluctuations of the nuclear magnetic field. Specifically, the z-component of the Overhauser field enters along the diagonals of the exchange/Zeeman Hamiltonian[8] in the $|\Uparrow\downarrow\rangle$, $|\Downarrow\uparrow\rangle$, $|\Uparrow\uparrow\rangle$, $|\Downarrow\downarrow\rangle$ basis and results in the dispersion of Eq. B.7. The in-plane components of the Overhauser field couple $|\Uparrow\downarrow\rangle \leftrightarrow |\Uparrow\uparrow\rangle$ and $|\Downarrow\uparrow\rangle \leftrightarrow |\Downarrow\downarrow\rangle$ but these states are split by the dark-bright splitting, 100s of μeV, determined by the isotropic part of the exchange interaction. As a result the dependence of the exciton energy on the in-plane fields is negligible. For X^{1-}, at zero external magnetic field, all three components of the Overhauser field are equally important. However, a simulation of the X^{1-} RF at $B = 0$ gives the same results for a B_N fluctuating in 1D and for a B_N fluctuating in 3D provided $B_{N,\text{rms}}^{\text{1D}} = \sqrt{3}B_{N,\text{rms}}^{\text{3D}}$. A small B suppresses the sensitivity of X^{1-} to in-plane B_N fluctuations.

We assume that each nuclear spin I can be represented by a spin-$\frac{1}{2}$, a 2-level fluctuator. To account for an underestimate of the hyperfine interaction (the real spins are larger than $\frac{1}{2}$) the Overhauser field is enhanced via a reduction in the total number of nuclei, $N \to N_{\text{eff}}$. Equivalently, we could work with a higher N_{eff} and larger A. The model represents a phenomenological way to create $B_N(t)$ which mimics the experiment. $B_N(t)$ is unique, the route to $B_N(t)$ is not.

There are two independent parameters that control spin noise in the simulation: the correlation time τ and the rms field $B_{N,\text{rms}}$. The experiment reveals a smaller nuclear spin correlation time for the X^0 exciton than the X^{1-} exciton. Also, the $B_{N,\text{rms}}$ for X^{1-} is lower than that for X^0. The origin of the difference is both surprising and not at all obvious. The results of the spin noise simulations for both X^0 and X^{1-} of QD2

are shown in Fig. B.7. For X^0 we extract $\tau = 5.5\,\mu$s and $B_{N,\mathrm{rms}} = 193\,$mT ($N_{\mathrm{eff}} = 65$, $A = 90\,\mu$eV, $g = -0.5$, $\Delta = 17.3\,\mu$eV in the simulation), for X^{1-} $\tau = 100\,\mu$s and $B_{N,\mathrm{rms}} = 9\,$mT ($N_{\mathrm{eff}} = 310$, $A = 9\,\mu$eV, $g = -0.5$ in the simulation).

The correlation time for the nuclear spin dipole-dipole interaction can be estimated by,

$$\tau = \hbar/E_{dd}, \quad E_{dd} = \mu_{I1}B_{I2} \sim \frac{\mu_0}{2\pi}\frac{\mu_{I1}\mu_{I2}}{d^3}, \quad \mu_i = \hbar\gamma_i I_i \qquad \text{(B.15)}$$

with energy E_{dd} of a nuclear dipole with moment μ_{I1} in the magnetic field B_{I2} of another dipole at distance d and gyromagnetic ratio γ. For example, taking the average of an In and Ga as one spin and an As spin as the other, separated by the atomic spacing in the GaAs lattice, $\tau = 47\,\mu$s. It gives order-of-magnitude agreement with the correlation time of the spin noise and this allows us to identify the process responsible for the spin noise: nuclear spin dipole-dipole processes.

References

1. Drexler, H., Leonard, D., Hansen, W., Kotthaus, J. P., and Petroff, P. M. *Phys. Rev. Lett.* **73**, 2252–2255 (1994).

2. Warburton, R. J., Schäflein, C., Haft, D., Bickel, F., Lorke, A., Karrai, K., Garcia, J., Schoenfeld, W., and Petroff, P. *Nature* **405**, 926 – 929 (2000).

3. Houel, J., Kuhlmann, A. V., Greuter, L., Xue, F., Poggio, M., Gerardot, B. D., Dalgarno, P. A., Badolato, A., Petroff, P. M., Ludwig, A., Reuter, D., Wieck, A. D., and Warburton, R. J. *Phys. Rev. Lett.* **108**, 107401 (2012).

4. Kogan, S. *Electronic noise and fluctuations in solids.* Cambridge University Press, (1996).

5. Machlup, S. *J. Appl. Phys.* **25**, 341–343 (1954).

6. Urbaszek, B., Marie, X., Amand, T., Krebs, O., Voisin, P., Maletinsky, P., Högele, A., and Imamoglu, A. *Rev. Mod. Phys.* **85**, 79–133 (2013).

7. Kloeffel, C., Dalgarno, P. A., Urbaszek, B., Gerardot, B. D., Brunner, D., Petroff, P. M., Loss, D., and Warburton, R. J. *Phys. Rev. Lett.* **106**, 046802 (2011).

8. Bayer, M., Ortner, G., Stern, O., Kuther, A., Gorbunov, A. A., Forchel, A., Hawrylak, P., Fafard, S., Hinzer, K., Reinecke, T. L., Walck, S. N., Reithmaier, J. P., Klopf, F., and Schäfer, F. *Phys. Rev. B* **65**, 195315 (2002).

Appendix C

Supplementary information to chapter 5 "Linewidth of single photons from a single quantum dot"

In chapter 5 "Linewidth of single photons from a single quantum dot: key role of nuclear spins", the linewidth of the optical transition of a single quantum dot is discussed. Nuclear spin noise is identified as the main dephasing mechanism and not charge noise. Here, we explain details of the experiments, the data processing and the modelling.

C.1 The semiconductor quantum dot sample

A quantum dot (QD) sample grown by molecular beam epitaxy is used to probe the linewidth of single photons from a single QD. All the data presented in chapter 5 were measured on the same QD.

The self-assembled QDs are embedded in a Schottky diode[1,2] as shown in Fig. C.1 (a). The layer sequence is:

1. *back contact*
   50 nm n^+-GaAs, doping level $\sim 1.7 \times 10^{18}$ cm^{-3}

2. *tunnelling barrier*
   25 nm i-GaAs

3. *active layer*
   InGaAs QDs (diameter ~ 20 nm, height ~ 5 nm) with centre wavelength 950 nm

4. *capping layer*
   150 nm i-GaAs

5. *blocking barrier*
   68 periods AlAs/GaAs 3 nm/1 nm

6. *cap*
   10 nm i-GaAs

7. *Schottky gate*
   5 nm/10 nm Ti/Au.

The background doping of as-grown GaAs is p $\sim 10^{13}$ cm^{-3}; two-dimensional electron gases grown under similar conditions have mobilities $> 10^6$ cm^2/Vs.

The number of electrons confined to the QD can be precisely controlled by the gate voltage V_g as illustrated in Fig. C.1 (b). A change of gate voltage yields a change of the QD's local potential ϕ by

$$\Delta\phi = \frac{\Delta V_g}{\lambda} \tag{C.1}$$

where $\lambda = 18.3$ denotes the sample's lever arm, defined as the ratio of back contact to gate distance d and tunnel barrier thickness. The exciton energy E is detuned with respect to the constant laser frequency by exploiting the dc Stark effect,

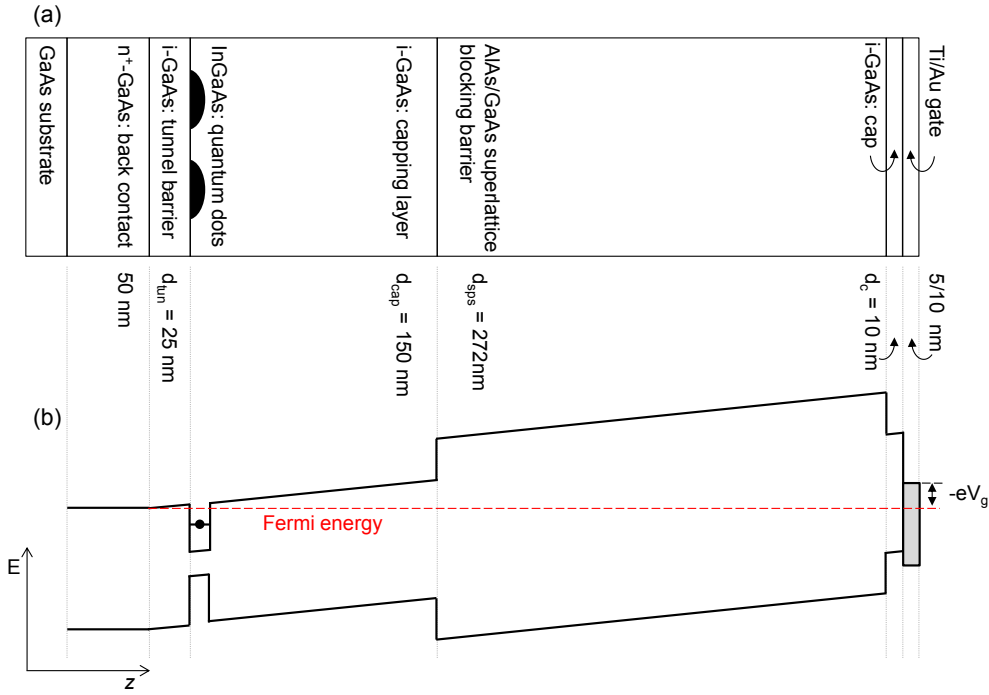$$\Delta E = a\Delta F, \quad \Delta F = \frac{\Delta V_g}{d} \tag{C.2}$$

Fig. C.1. (a) Sample layer structure and the corresponding (b) energy band diagram. The Fermi energy is pinned to the conduction band edge of the back contact. The figures are to scale with respect to length.

with Stark shift coefficient a and electric field F.

C.2 The dc Stark effect

The Stark shift is determined by recording the resonance position in V_g for many laser frequencies, the laser frequency measured in each case with an ultra-precise wavemeter. The Stark shift is linear in ΔF for the small windows of V_g used here, Fig. C.2 (a). The neutral exciton X^0 has a larger Stark shift ($a = 0.0306\,\mu\text{eVcm/V}$) than the trion X^{1-} ($a = 0.0219\,\mu\text{eVcm/V}$) and thus it is more sensitive to charge noise. Red and blue X^0 transitions have identical Stark shifts, inset of Fig. C.2 (a). The larger linewidth of X^{1-} compared to X^0 despite the smaller Stark shift, and the difference in linewidth of the red and blue X^0 transitions despite the identical response to charge noise, both point to spin noise as the major dephasing mechanism. The identification can be backed up by experiments on several QDs which reveal no dependence of the linewidth on the Stark shift coefficient, Fig. C.2 (b). From quantum dot to quantum dot the Stark shift varies by up to 50% without a correlated change in linewidth.
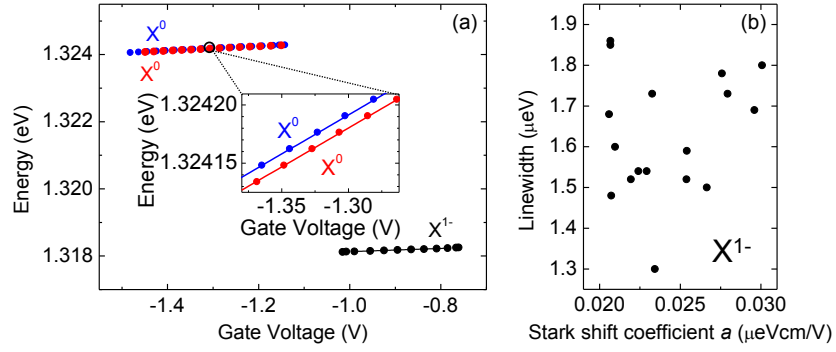
Fig. C.2. (a) Exciton energy voltage plateaus to determine the Stark shift coefficients of the neutral exciton X^0 and the trion X^{1-}. Inset shows a zoom in of X^0 revealing the fine structure splitting $\Delta = 11.5\,\mu\text{eV}$. (b) Linewidth versus Stark shift. Statistics on X^{1-} of 17 QDs from the same wafer with a spread in Stark shift of up to 50% demonstrate no significant correlation between linewidth and Stark shift.

C.3 Power broadening

The linewidth of the optical resonance increases with increasing resonant excitation power, Fig. C.3. The additional contribution to the linewidth is known as *power broadening*, described for an ideal 2-level system by[3]

$$\Gamma(\Omega) = \sqrt{\Gamma_0^2 + \gamma^2 + 2\Omega^2}, \quad \Gamma_0 = \hbar/\tau_R \tag{C.3}$$

with Rabi energy Ω and radiative lifetime τ_R. An inhomogeneous broadening is included by γ.

For X^{1-}, the 2-level model with constant γ describes the data very well, Fig. C.3 (a). The inhomogeneous broadening γ is constant at low power, decreasing at high power but only when power broadening dominates, such that a constant γ allows the experimental data to be described very well (see chapter 5). By fitting the 2-level model to the data a resonant excitation power measured by a photo diode beneath the sample can be converted to a Rabi energy, Fig. C.3 (a).

Conversely for X^0, the inhomogeneous broadening is strongly power dependent: γ increases significantly with increasing resonant excitation power (see chapter 5). The 2-level model with constant γ does not describe the data well. Furthermore, we observe a different behaviour of the red and blue transition of the neutral exciton, Fig. C.3 (b). At low power the linewidths of the red and blue transitions are the same, at high power the red transition is broader. The reason for this is unknown. It is however a robust
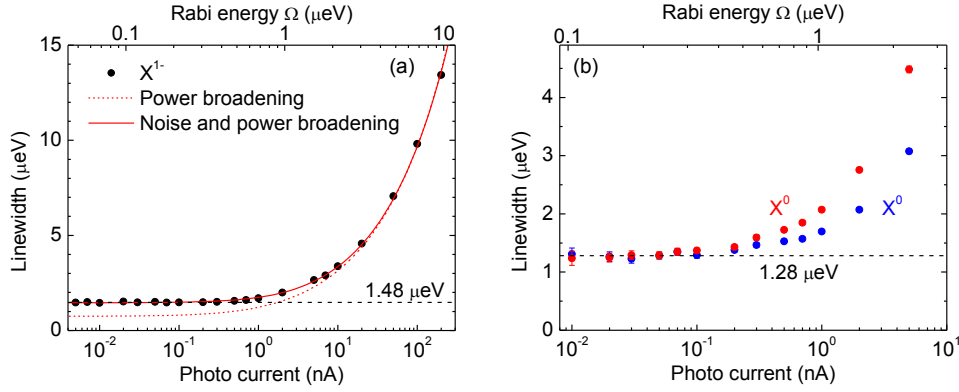
Fig. C.3. Power broadening. Linewidth power dependence for X^{1-} (a) and X^0. The 2-level model with (solid red lines) and without (dashed red lines) an inhomogeneous broadening ($\gamma = 1.25\,\mu$eV) is fitted to the X^{1-} data. The transform-limit Γ_0 is $0.75\,\mu$eV for X^{1-} and $0.92\,\mu$eV for X^0.

phenomenon observed at all the QDs studied so far and points to the dominant role of nuclear spins in determining the optical linewidth.

A phonon-induced dephasing process as observed at very high Rabi couplings[4] and in pulsed experiments[5] is negligible at these Rabi couplings.

C.4 Resonance fluorescence

The quantum dot optical resonance is driven with a resonant continuous-wave laser (1 MHz linewidth) focused on to the sample surface. Reflected or scattered laser light is rejected with a dark-field technique using crossed linear polarizations for excitation and detection[6]. The axes of linear polarization are aligned to the sample's crystal axes. The polarization of the neutral exciton is rotated by $\sim \pi/4$ with respect to the polarization axes for this particular QD. Consequently, at zero magnetic field both red and blue transitions are observed with equal RF intensity. The two X^{1-} transitions are circularly polarized, one σ^+ the other σ^-.

Resonance fluorescence is detected with a silicon avalanche photodiode in photon counting mode. The experiment is not shielded against the earth's magnetic field, thus $B_{\min} \sim 50\,\mu$T. All the experiments were performed with the sample at $4.2\,$K.

C.5 Quantum dot noise spectrum

To determine the QD noise spectrum the arrival time of each photon is recorded over the entire measurement time T. Post measurement, a binning time t_{bin} is selected, typically
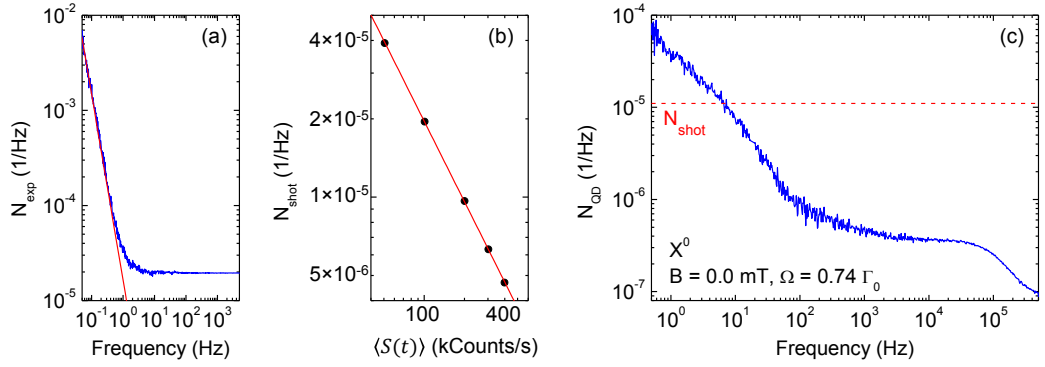
Fig. C.4. (a) Noise spectrum of the experiment. Intensity fluctuations of the laser light in the setup cause a $1/f^2$-behaviour of $N_{exp}(f)$ at low frequencies (exponent of red fit -1.96). For $f > 10$ Hz the spectrum is dominated by shot noise, thus, the spectrum is flat. The average count rate of the detected laser light is 101 kCounts/s in this particular experiment. (b) Shot noise. Noise spectra of the experiment alone were recorded at different laser light count rates to extract the dependence of the shot noise on the count rate. A proportionality of the shot noise to $\langle S(t) \rangle^{-1}$ is verified (exponent of red fit -1.03). (c) Quantum dot noise spectrum. The noise of the experiment is typically larger than the noise of the QD. The shot noise (red dashed line) typically equals $N_{QD}(f)$ at low frequencies ($f \sim 10$ Hz), and exceeds $N_{QD}(f)$ at higher frequencies. The RF count rate is 176 kCounts/s in this particular experiment. The noise spectrum shown here is not from the QD discussed in chapter 5 but it is from a QD in the same sample.

$1 \, \mu$s. The number of counts in each time bin is $S(t)$, the average number of counts per bin $\langle S(t) \rangle$. The fast Fourier transform of the normalized RF signal $S(t)/\langle S(t) \rangle$ is calculated to yield a spectrum of the noise power $N_{RF}(f)$, specifically

$$N_{RF}(f) = |\text{FFT}\,[S(t)/\langle S(t) \rangle]|^2 \,(t_{bin})^2/T. \qquad (C.4)$$

$N_{RF}(f)$ has the same spectrum independent of the choice of t_{bin} and T: smaller values of t_{bin} allow $N_{RF}(f)$ to be determined to higher values of frequency f; larger values of T allow $N_{RF}(f)$ to be determined with higher resolution. The high frequency limit of our experiment is only limited by the photon flux.

All Fourier transforms are normalized[7] such that the integral of the noise power $N_x(f)$ over all positive frequencies equals the variance of the fluctuations δx,

$$\langle (\delta x)^2 \rangle = \int_0^\infty df\, N_x(f). \qquad (C.5)$$

To record a noise spectrum of the experiment alone, the QD is detuned by > 100 linewidths relative to the laser and one polarizer is rotated by a small angle to open

slightly the detection channel for reflected laser light, choosing the rotation so that the detected laser light gives a count rate similar to the QD RF. A noise spectrum of the reflected laser light (Fig. C.4 (a)) is recorded using exactly the routine used to analyse the RF, yielding $N_{\mathrm{exp}}(f)$. $N_{\mathrm{exp}}(f)$ has a $1/f^2$-behaviour at low frequencies arising from intensity fluctuations in the setup. For $f > 10$ Hz, $N_{\mathrm{exp}}(f)$ has a completely f-independent spectrum, $N_{\mathrm{exp}} \sim 10^{-5}$ Hz^{-1}: this is the shot noise N_{shot}. The noise of the experiment is typically larger than the noise of the QD $N_{\mathrm{QD}}(f)$. The shot noise is proportional to $\langle S(t) \rangle^{-1}$ (Fig. C.4 (b)) and not to $\langle S(t) \rangle^{1/2}$ due to the normalization of $S(t)$ by $\langle S(t) \rangle$ in the calculation of the spectrum. N_{shot} is comparable to $N_{\mathrm{QD}}(f)$ at low frequencies ($f \sim 10$ Hz), and exceeds $N_{\mathrm{QD}}(f)$ at higher frequencies, Fig. C.4 (c).

The noise spectrum of the QD alone is then determined using

$$N_{\mathrm{QD}}(f) = N_{\mathrm{RF}}(f) - N_{\mathrm{exp}}(f). \tag{C.6}$$

Correction of $N_{\mathrm{RF}}(f)$ with $N_{\mathrm{exp}}(f)$ where $N_{\mathrm{RF}}(f)$ and $N_{\mathrm{exp}}(f)$ are not measured simultaneously is successful on account of the high stability of the setup. Furthermore, no spectral resonances in $N_{\mathrm{QD}}(f)$ have been discovered. We present here $N_{\mathrm{QD}}(f)$ after averaging at each f over a frequency range Δf to yield equidistant data points on a logarithmic scale. This entire procedure enables us to discern $N_{\mathrm{QD}}(f)$ down to values of 10^{-7} Hz^{-1} for $T = 2$ hours.

C.6 Effect of charge noise on the linewidth

The quantum dot noise spectrum $N_{\mathrm{QD}}(f)$ allows us to set an upper limit of the linewidth broadening γ_{c} due to charge noise. The energy jitter due to charge fluctuations is less than the linewidth such that the change in RF is related quadratically to the detuning for fluctuations around $\delta = 0$. This quadratic approximation overestimates the effect of charge fluctuations on the linewidth. The variance of the quantum dot RF noise, $\sigma_{\mathrm{QD,c}}^2$, is related to an integral of the noise curve. Integrating over the bandwidth of charge noise after subtracting spin noise,

$$\gamma_{\mathrm{c}} = \frac{\Gamma}{2} \left(\sigma_{\mathrm{QD,c}}^2 / 3 \right)^{1/4}. \tag{C.7}$$

The charge noise has a $1/f$-like component and a Lorentzian component. We integrate both from 0.1 Hz to 1 GHz. Applying this concept to the X^{1-} noise spectrum of Fig. 5.2, with $\Gamma = 1.48 \, \mu$eV this predicts $\gamma_{\mathrm{c}} < 0.05 \, \mu$eV.

C.7 Noise spectra modelling

Our previous experiments[8] demonstrate that the spectrum of the noise in the RF is dominated by charge noise at low frequency, spin noise at high frequency. The noise sensor, the RF from a single quantum dot, has a trivial dependence on the fluctuating electric $F(t)$ and magnetic fields $B_N(t)$ only for small fluctuations in the detunings around particular values of detuning δ. Monte Carlo simulations allow us to determine both the electric field and magnetic field noise accurately by describing the response of the sensor for all δ, treating charge noise and spin noise on an equal footing.

The basic approach is to calculate $F(t)$ and $B_N(t)$, in each case from an ensemble of independent, but identical, 2-level fluctuators using a Monte Carlo method; to calculate the RF signal $S(t)$ from $F(t)$ and $B_N(t)$; and to compute the noise $N(f)$ from $S(t)$ using exactly the same routine as for the experiments (but without the correction for extrinsic noise of course). Here, we discuss the spin noise modelling of the neutral exciton X^0 used to extract the root-mean-square (rms) values of the magnetic field $B_{N,\mathrm{rms}}$ in Fig. 5.3 (b). The modelling of charge noise is explained in detail elsewhere[8].

For X^0, the RF depends on the electric and magnetic fields according to

$$S(t) = \frac{\left(\frac{\Gamma_0}{2}\right)^2}{(aF(t) + \delta_0(t) + \delta)^2 + \left(\frac{\Gamma_0}{2}\right)^2}, \quad \delta_0(t) = \pm\frac{1}{2}\sqrt{\Delta^2 + \delta_1(t)^2}, \quad \delta_1(t) = \frac{1}{2}g\mu_B B_N(t),$$

(C.8)

where a is the dc Stark coefficient, g the electron g-factor and Δ the fine structure splitting. For the blue Zeeman branch $\delta_0(t)$ is positive, for the red one negative, respectively.

An ensemble of identical 2-level fluctuators fully describes spin noise, Fig. 5.3 (a).

C.7.1 Spectrum of a 2-level fluctuator

A 2-level fluctuator occupies either state 0 with lifetime τ_0 or state 1 with lifetime τ_1. The probability p of being, at any time, in state 1 is $\tau_1/(\tau_0 + \tau_1)$; the probability of being in state 0 is $\tau_0/(\tau_0 + \tau_1)$. The configuration $C(t)$ of a 2-level fluctuator, either 0 or 1, is determined by the probabilities of a $0 \rightarrow 1$ transition[9],

$$p_{0\rightarrow 1}(\delta t) = 1 - \frac{1}{\tau_0 + \tau_1}\left[\tau_1 \exp\left(-\left(\frac{1}{\tau_0} + \frac{1}{\tau_1}\right)\delta t\right) + \tau_0\right] \qquad \text{(C.9)}$$

and a $1 \to 0$ transition,

$$p_{1\to0}(\delta t) = 1 - \frac{1}{\tau_0 + \tau_1} \left[\tau_0 \exp\left(-\left(\frac{1}{\tau_0} + \frac{1}{\tau_1} \right) \delta t \right) + \tau_1 \right] \qquad (C.10)$$

where δt denotes the time over which the system evolves. The power spectrum of a 2-level fluctuator $S(\omega)$ is Lorentzian[9],

$$S(\omega) = \frac{1}{\pi} \frac{\tau_0 \tau_1}{(\tau_0 + \tau_1)^2} \frac{1/T}{\omega^2 + (1/T)^2}, \quad 1/T = 1/\tau_0 + 1/\tau_1. \qquad (C.11)$$

C.7.2 Spin noise

The calculation of the time trace of the magnetic field $B_N(t)$ is simplified, such that each nucleus is treated as a two-level fluctuator, with equal $0 \to 1$, $1 \to 0$ transition rates, $1/\tau$. At $t = 0$, each nucleus is initialized by a random number generator giving a configuration of nuclear spins $C(0)$. At a later time, δt, $C(\delta t)$ is calculated from $C(0)$ again with a random number generator using the probabilities $p_{1\to0}(\delta t)$ and $p_{0\to1}(\delta t)$ from the theory of a two-level fluctuator. The nuclei are treated independently.

The nuclear magnetic field, the so-called Overhauser field B_N, is given by[10]

$$B_N = \frac{v_0}{g\mu_B} \sum_{i=1}^{N} A_i \left| \psi(\mathbf{r}_i) \right|^2 I_i \qquad (C.12)$$

where v_0 is the atomic volume, A_i the hyperfine interaction constant, $\mathbf{r}_i$ is the position of the nuclei i with spin I_i, and $\psi(\mathbf{r})$ is the normalized electron envelope function. By using an average hyperfine constant[11] $A = 90\,\mu\text{eV}$ and approximating the electron envelope function $\psi(\mathbf{r})$ by a top hat, Eq. (C.12) simplifies to

$$B_N = \frac{A}{g\mu_B N_{\text{eff}}} \sum_{i=1}^{N_{\text{eff}}} I_i. \qquad (C.13)$$

N_{eff} denotes the number of nuclear spins inside the top hat envelope function.

Regarding the dimensionality of B_N, a 1D model for the nuclear spins is appropriate for X^0. The isotropic part of the electron-hole exchange interaction "protects" the X^0 from the in-plane fluctuations of the nuclear magnetic field. Specifically, the z-component of the Overhauser field enters along the diagonals of the exchange/Zeeman Hamiltonian[12] in the $|\Uparrow\downarrow\rangle$, $|\Downarrow\uparrow\rangle$, $|\Uparrow\uparrow\rangle$, $|\Downarrow\downarrow\rangle$ basis and results in the dispersion of Eq. C.8. The in-plane components of the Overhauser field couple $|\Uparrow\downarrow\rangle \leftrightarrow |\Uparrow\uparrow\rangle$ and $|\Downarrow\uparrow\rangle \leftrightarrow |\Downarrow\downarrow\rangle$ but these states are split by the dark-bright splitting, 100s of μeV, determined by the

isotropic part of the exchange interaction. As a result the dependence of the exciton energy on the in-plane fields is negligible.

We assume that each nuclear spin I can be represented by a spin-$\frac{1}{2}$, a 2-level fluctuator. To account for an underestimate of the hyperfine interaction (the real spins are larger than $\frac{1}{2}$) the Overhauser field is enhanced via a reduction in the total number of nuclei, $N \rightarrow N_{\text{eff}}$. Equivalently, we could work with a higher N_{eff} and larger A. The model represents a phenomenological way to create $B_N(t)$ which mimics the experiment. $B_N(t)$ is unique, the route to $B_N(t)$ is not.

There are two independent parameters that control spin noise in the simulation: the correlation time τ and the rms field $B_{N,\text{rms}}$. For the simulation shown in Fig. 5.3 (a) $A = 90\,\mu\text{eV}$, $N_{\text{eff}} = 178$, corresponding to $B_{N,\text{rms}} = 116\,\text{mT}$, and $\tau = 6.0\,\mu\text{s}$ were used. The noise spectra at higher Rabi energies were fitted by decreasing N_{eff} (increasing $B_{N,\text{rms}}$) and the same τ.

References

1. Drexler, H., Leonard, D., Hansen, W., Kotthaus, J. P., and Petroff, P. M. *Phys. Rev. Lett.* **73**, 2252–2255 (1994).

2. Warburton, R. J., Schäflein, C., Haft, D., Bickel, F., Lorke, A., Karrai, K., Garcia, J., Schoenfeld, W., and Petroff, P. *Nature* **405**, 926 – 929 (2000).

3. Loudon, R. *The Quantum Theory of light.* Oxford Science Publications, (2009).

4. Ulrich, S. M., Ates, S., Reitzenstein, S., Löffler, A., Forchel, A., and Michler, P. *Phys. Rev. Lett.* **106**, 247402 (2011).

5. Ramsay, A. J., Godden, T. M., Boyle, S. J., Gauger, E. M., Nazir, A., Lovett, B. W., Fox, A. M., and Skolnick, M. S. *Phys. Rev. Lett.* **105**, 177402 (2010).

6. Kuhlmann, A. V., Houel, J., Brunner, D., Ludwig, A., Reuter, D., Wieck, A. D., and Warburton, R. J. *Rev. Sci. Instrum.* **84**, 073905 (2013).

7. Kogan, S. *Electronic noise and fluctuations in solids.* Cambridge University Press, (1996).

8. Kuhlmann, A. V., Houel, J., Ludwig, A., Greuter, L., Reuter, D., Wieck, A. D., Poggio, M., and Warburton, R. J. *Nature Phys.* **9**, 570–575 (2013).

9. Machlup, S. *J. Appl. Phys.* **25**, 341–343 (1954).

10. Urbaszek, B., Marie, X., Amand, T., Krebs, O., Voisin, P., Maletinsky, P., Högele, A., and Imamoglu, A. *Rev. Mod. Phys.* **85**, 79–133 (2013).

11. Kloeffel, C., Dalgarno, P. A., Urbaszek, B., Gerardot, B. D., Brunner, D., Petroff, P. M., Loss, D., and Warburton, R. J. *Phys. Rev. Lett.* **106**, 046802 (2011).

12. Bayer, M., Ortner, G., Stern, O., Kuther, A., Gorbunov, A. A., Forchel, A., Hawrylak, P., Fafard, S., Hinzer, K., Reinecke, T. L., Walck, S. N., Reithmaier, J. P., Klopf, F., and Schäfer, F. *Phys. Rev. B* **65**, 195315 (2002).

Curriculum Vitae

Andreas Volker Kuhlmann

Department of Physics
University of Basel
Klingelbergstrasse 82
4056 Basel
Switzerland

Background

Birth:	15th April 1985, Ansbach, Germany
Citizenship:	German
Languages:	German (mother tongue), English (fluent)

Education

2013	PhD in Experimental Physics
	University of Basel, Switzerland
	Advisor: Prof. Richard J. Warburton
	Thesis: *Charge noise and spin noise in a semiconductor quantum device*
2011	Diploma in Physics
	Julius-Maximilians University Würzburg, Germany
	Advisor: Prof. Bert Hecht
	Thesis: *Resonance fluorescence from single semiconductor quantum dots*
2009	MPhys in Physical Science
	Heriot-Watt University, Edinburgh, UK
2004	Abitur at the Theresien-Gymnasium, Ansbach, Germany

List of Publications

(∗) Publication covered in this thesis.

1. (∗) J. Houel, <u>A. V. Kuhlmann</u>, L. Greuter, F. Xue, M. Poggio, B. D. Gerardot, P. A. Dalgarno, A. Badolato, P. M. Petroff, A. Ludwig, D. Reuter, A. D. Wieck, and R. J. Warburton,
   Probing single-charge fluctuations at a GaAs/AlAs interface using laser spectroscopy on a nearby InGaAs quantum dot,
   Phys. Rev. Lett. **108**, 107401 (2012).

2. M. Heiss, Y. Fontana, A. Gustafsson, G. Wüst, C. Magen, D. D. O'Regan, J. W. Luo, B. Ketterer, S. Conesa-Boj, <u>A. V. Kuhlmann</u>, J. Houel, E. Russo-Averchi, J. R. Morante, M. Cantoni, N. Marzari, J. Arbiol, A. Zunger, R. J. Warburton, and A. Fontcuberta i Morral,
   Self-assembled quantum dots in a nanowire system for quantum photonics,
   Nature Mater. **12**, 439 (2013).

3. (∗) <u>A. V. Kuhlmann</u>, J. Houel, D. Brunner, A. Ludwig, D. Reuter, A. D. Wieck, and R. J. Warburton,
   A dark-field microscope for background-free detection of resonance fluorescence from single semiconductor quantum dots operating in a set-and-forget mode,
   Rev. Sci. Instrum. **84**, 073905 (2013).

4. (∗) <u>A. V. Kuhlmann</u>, J. Houel, A. Ludwig, L. Greuter, D. Reuter, A. D. Wieck, M. Poggio, and R. J. Warburton,
   Charge noise and spin noise in a semiconductor quantum device,
   Nature Phys. **9**, 570 (2013).

5. (∗) J. H. Prechtel, <u>A. V. Kuhlmann</u>, J. Houel, L. Greuter, A. Ludwig, D. Reuter, A. D. Wieck, and R. J. Warburton,
   A frequency-stabilized source of single photons from a solid-state qubit,
   Phys. Rev. X **3**, 041006 (2013).

6. J. Houel, J. H. Prechtel, D. Brunner, <u>A. V. Kuhlmann</u>, C. E. Kuklewicz, B. D. Gerardot, N. G. Stoltz, P. M. Petroff, and R. J. Warburton,
   High resolution coherent population trapping on a single hole spin in a semiconductor,
   arXiv:1307.2000.

7. ($*$) <u>A. V. Kuhlmann</u>, J. H. Prechtel, J. Houel, A. Ludwig, D. Reuter, A. D. Wieck, and R. J. Warburton,
   Linewidth of single photons from a single quantum dot: key role of nuclear spins,
   arXiv:1307.7109.

8. M. Munsch, G. Wüst, <u>A. V. Kuhlmann</u>, F. Xue, A. Ludwig, D. Reuter, A. D. Wieck, M. Poggio, R. J. Warburton,
   Manipulation of the nuclear spin ensemble in a quantum dot with chirped magnetic resonance pulses,
   submitted (2013)